

ORGAN DOSE MEASUREMENTS FROM MULTIPLE-DETECTOR COMPUTED
TOMOGRAPHY USING A COMMERCIAL DOSIMETRY SYSTEM AND TOMOGRAPHIC,
PHYSICAL PHANTOMS

By

LINDSEY K LAVOIE

A DISSERTATION PRESENTED TO THE GRADUATE SCHOOL
OF THE UNIVERSITY OF FLORIDA IN PARTIAL FULFILLMENT
OF THE REQUIREMENTS FOR THE DEGREE OF
DOCTOR OF PHILOSOPHY

UNIVERSITY OF FLORIDA

2009

© 2009 Lindsey K Lavoie

To my Grandma, from whom I got all of my brains

ACKNOWLEDGEMENTS

I would like to express my gratitude first and foremost to my advisor, Dr. Manuel Arreola. The opportunities he has given me in my five years of graduate education at the University of Florida and of clinical experience working at Shands at UF are truly invaluable and ones that I will take with me after graduation. His encouragement and positive reinforcement throughout this entire process will always be appreciated.

To my other two advisors, I am grateful for all they have taught me during my time at UF. Dr. Libby Brateman pushed me to always do my best and constantly challenged me with her essential questions and insightful critiques. Her demand for only high-level work is one that I hope to demand of myself in years to come. Dr. Lynn Rill was a source of constant encouragement; she provided a sounding board when I needed a second set of ears. Her door was always open to me for research and clinical questions, as well as those that were a part of life outside Shands, and for that I am thankful.

There are several others that I would like to acknowledge as helping me along this journey. Dr. David Hintenlang and Dr. Scott Banks provided me guidance and counseling throughout this research project. I am grateful to all of the radiologists involved in the RPC. Because of them I have gained a clinical knowledge, especially in CT, that complements everything I have learned during these five years of research. The CT technologists at Shands answered my countless clinical questions which helped give me a true understanding of CT protocols and how they are used clinically, and they were always gracious when answering my redundant question, "Is CT4 available?" For this, I am grateful.

I would also like to thank everyone in the QC/GA office for the small things they do on a daily basis. Jen Sirera has helped me to understand aspects of a radiology department that go beyond medical physics. Her constantly positive demeanor, despite the everyday stresses of her

job, is one I hope to emulate in the professional world. Carly Williams taught me most of what I have learned about testing x-ray equipment. Bo Hartmann's attention to detail is one that I admire and to which I strive to be better. Tom Griglock has assumed most of the responsibility of the GAs, an experience I only hope he can appreciate when he begins applying for jobs. For all of these people, I am thankful. And finally, I would like to express my sincere thanks to Monica Ghita, without whom I could not have completed this project. She worked late nights with me, struggling to place dots into the phantom and meticulously aligning the phantom in the scanner. The conversations I had with her are ones that helped shaped this research into a final product; I could not have done it without her.

On a more personal note, I would like to thank my Gator friends for their support over the past five years. I would especially like to thank Duane Ammons for his love and encouragement, particularly in these last few months; he pushed me to keep going and was there to pick me up when I was down. To my colleagues that started at UF with me in 2004, especially Ryan Fisher, Bob Ambrose, and Keelan Seabolt, I would not have survived my first year down here without them. These people, among many others, became my family away from home, and for that I will be forever grateful.

To my small family at home, Ed Podesky, Kathy Podesky, and Steve and Connor DeCosta, their support in my lengthy education made the transition to UF as seamless as it could have possibly been and for this I am grateful.

Over these past five years, Dr. Rich Mauceri has provided me support in as many ways as he possibly could, and for this I am extremely thankful. His excitement for me joining the field of radiology has been contagious and I look forward to scholarly discussions with him in "the Lounge."

And finally, I want to extend my deepest gratitude to my mom, Dona Lavoie. Without her, I would not be the person I am today. The sacrifices she has made for me over the years have allowed me the successes I have had in my life. She truly is the wind beneath my wings.

TABLE OF CONTENTS

	<u>page</u>
ACKNOWLEDGEMENTS.....	4
TABLE OF CONTENTS.....	7
LIST OF TABLES.....	12
LIST OF FIGURES.....	14
ABSTRACT.....	17
CHAPTER	
1 INTRODUCTION.....	19
1.1 Increased Use of Computed Tomography.....	19
1.2 Effects on Pediatric Patients.....	20
1.3 Specific Aims.....	22
2 CLINICAL CT PROTOCOLS.....	24
2.1 Radiology Practice Committee.....	24
2.2 Protocol Standardization and Revision.....	25
2.3 Clinical Indications in Protocols.....	26
2.4 Picture Archiving and Communications System.....	26
2.5 Protocol Development Process.....	28
2.5.1 Database Development.....	28
2.5.2 Protocol Template.....	28
2.5.2.1 Title and illustration.....	29
2.5.2.2 Acquisition parameter description table.....	29
2.5.2.3 Reconstruction parameter tables.....	29
2.5.2.4 Reformation parameter table.....	30
2.5.2.5 Additional protocol information.....	30
2.5.2.6 Indications.....	31
2.5.2.7 Using the templates and updating the protocols.....	31
2.6 Protocol Website.....	32
3 MULTIPLE-DETECTOR COMPUTED TOMOGRAPHY.....	36
3.1 Detector Array Systems.....	36
3.2 Modes of Acquisition.....	37
3.2.1 Axial Data Acquisition.....	37
3.2.2 Helical Data Acquisition.....	37
3.2.3 Volumetric Data Acquisition.....	38

3.3	Clinical CT Considerations	39
3.3.1	Slice Thickness	39
3.3.2	Image Reconstruction	39
3.4	Dose-Reduction Techniques	40
3.4.1	Tube Current (mA) Adjustment	40
3.4.2	Tube Current (mA) Modulation	41
3.4.2.1	Angular (X-Y) tube current (mA) modulation	42
3.4.2.2	Z-axis tube current (mA) modulation	42
3.4.3	Tube Voltage	42
4	COMPUTED TOMOGRAPHY DOSE DESCRIPTORS	45
4.1	Definitions	45
4.1.1	Kerma	45
4.1.2	Absorbed Dose (D)	45
4.1.3	Equivalent Dose (H_T)	46
4.1.4	Effective Dose (E)	46
4.2	Effective Dose as a Dose Descriptor	46
4.2.1	Applications of Effective Dose	47
4.2.2	Limitations of Effective Dose as a Patient Dose Descriptor in CT	47
4.2.2.1	Population-based risk	47
4.2.2.2	Tissue-weighting factors	48
4.3	Recommendations	48
5	COMPUTED TOMOGRAPHY DOSE INDEX	51
5.1	CTDI Definitions	51
5.1.1	MSAD	51
5.1.2	CTDI	52
5.1.3	$CTDI_{FDA}$	52
5.1.4	$CTDI_{100}$	53
5.1.5	$CTDI_w$	54
5.1.6	$CTDI_{vol}$	54
5.2	Dose-Length Product	55
5.3	Analysis of the Applicability of the Measurement of CTDI and DLP	56
5.3.1	Underestimation of Dose using CTDI in MDCT	56
5.3.2	Proposed Solutions	57
5.3.2.1	Extended phantoms	57
5.3.2.2	Small-volume ionization chamber	58
6	INSTRUMENTATION AND PHANTOMS	61
6.1	Ionization Chambers	61
6.1.1	A 6-cc Chamber	61
6.1.2	A 3-cc Pencil Chamber	62
6.1.3	A 0.6-cc Chamber	62
6.2	Solid-State Detector	63

6.3	Tube Voltage Meter	63
6.4	Dosimetry Phantoms	63
6.4.1	Stylized Phantoms	63
6.4.2	Tomographic Phantoms	64
6.5	Phantom for Image Quality Evaluations	65
7	CHARACTERIZATION OF X-RAY BEAMS OF THE VOLUMETRIC CT SYSTEM	72
7.1	Exposure Reproducibility	72
7.1.1	Service Mode	72
7.1.2	Clinical Mode	73
7.2	Beam Quality	73
7.2.1	Accuracy in kV	74
7.2.2	Beam Filtration in CT	74
7.2.3	Half-Value Layer	76
7.3	Beam Width	77
7.4	Dose Profile	77
7.4.1	X-Axis	77
7.4.2	Z-Axis	77
8	OPTICALLY-STIMULATED LUMINESCENT DOSIMETERS	82
8.1	Optically-Stimulated Luminescence	82
8.1.1	Disadvantages of TL Dosimeters	83
8.1.2	Advantages of OSL Dosimeters	83
8.2	Characterization of OSL Dosimetry System	84
8.2.1	Other Radiation-Measuring Devices	84
8.2.2	Tracking of System Standards	85
8.2.3	Dosimeter Response	86
8.2.4	Room-Light Erasure	87
8.2.5	Energy Response	88
8.2.6	Scatter Response	88
8.2.7	Dosimeter Calibration	90
8.2.8	Linearity Response	91
8.2.9	Angular Response	92
8.2.9.1	In-air response	92
8.2.9.2	In-phantom response	92
8.2.10	Comparison of OSL Dosimeter in and out of its Light-Tight Case	93
9	ORGAN DOSE MEASUREMENTS	98
9.1	Pediatric Head Study	99
9.1.1	Volumetric Protocol	99
9.1.2	Helical Protocol	100
9.1.3	Image Quality Analysis	101
9.2	Adult Brain Perfusion	101
9.2.1	Volumetric Protocol	102

9.2.2	Helical Protocol.....	104
9.2.3	Image Quality Evaluation	104
9.3	Adult Cardiac CT Angiography.....	105
9.3.1	Volumetric Protocol.....	107
9.3.2	Helical Protocol.....	108
10	RESULTS.....	119
10.1	Characterization of X-Ray Beams of Volumetric CT Scanner.....	119
10.1.1	Exposure Reproducibility	119
10.1.1.1	Service mode	119
10.1.1.2	Clinical mode.....	119
10.1.2	Beam Quality	120
10.1.2.1	Tube voltage	120
10.1.2.2	Total filtration.....	121
10.1.2.3	Half-value layer	122
10.1.3	Beam Width	122
10.1.4	Dose Profile.....	123
10.1.4.1	X-axis.....	123
10.1.4.2	Z-axis.....	123
10.2	Characterization of OSL Dosimetry System.....	124
10.2.1	Tracking of System Standards	124
10.2.2	Dosimeter Response.....	125
10.2.3	Room-Light Erasure.....	125
10.2.4	Energy Response.....	126
10.2.5	Scatter Response	127
10.2.6	Dosimeter Calibration	128
10.2.7	Linearity Response.....	128
10.2.8	Angular Response	129
10.2.8.1	In-air response	129
10.2.8.2	In-phantom response.....	130
10.2.9	Comparison of OSL Dosimeter In and Out of Its Light-Tight Case.....	130
10.3	Organ Dose Measurements	130
10.3.1	Pediatric Head Study.....	131
10.3.1.1	Organ doses	131
10.3.1.2	Image quality	135
10.3.2	Adult Brain Perfusion	136
10.3.2.1	Organ doses	136
10.3.2.2	Image quality	139
10.3.4	Adult Cardiac CTA	141
10.3.4.1	Organ doses	141
10.3.4.2	Image quality	144
10.3.5	Comparisons to Monte Carlo Organ Dose Simulations.....	145
11	SUMMARY AND CONCLUSIONS.....	177
11.1	Summary of This Research Project.....	177

11.2 Future Work	179
11.3 Final Words	182

APPENDIX

A EXAMPLES OF IMPLEMENTED CT PROTOCOLS	183
B DOSIMETRIC PHANTOMS	192
LIST OF REFERENCES	195
BIOGRAPHICAL SKETCH	201

LIST OF TABLES

<u>Table</u>	<u>page</u>
4-1 Tissue-weighting factors.....	50
8-1 HVL as a function of effective energy.....	96
9-1 Scan parameters for volumetric pediatric head protocol	109
9-2 Locations and number of dosimeters used in and on pediatric phantom.....	109
9-3 Scan parameters for helical pediatric head protocol.....	110
9-4 Details of volumetric brain perfusion protocols.	110
9-5 Locations and number of dosimeters used in and on adult phantom for brain perfusion protocol.	114
9-6 Scan parameters for helical adult brain perfusion protocol.	114
9-7 Scan parameters for adult cardiac CTA protocol.....	115
9-8 Location and number of dosimeters used in and on adult phantom for cardiac CTA protocol.	115
10-1 Reproducibility of x-ray tube operated in service mode.....	149
10-2 Reproducibility of volumetric clinical protocol.....	149
10-3 Reproducibility of helical clinical protocol.	149
10-4 Measured beam energies of scanners used for organ dose measurements.	150
10-5 Measured HVLs for each nominal x-ray tube voltage for the Aquilion One	152
10-6 Measured HVLs for each nominal x-ray tube voltage for the Aquilion 64.....	153
10-7 Measurement standards for microStar reader.	156
10-8 Dose response of standard and screened dots.	159
10-9 Energy response of the OSL dosimeters.....	160
10-10 Measurements used in flat-field scatter response.	160
10-11 Response of the dosimeters to scatter and a flat x-ray field.	161
10-12 Response of energy and scatter to the CT x-ray beams used for clinical protocols.	162

10-13	The calculated f-factors.....	162
10-14	Mean doses with a 95% confidence interval measured by the dosimeters in and out of their plastic cases in two different positions within the CTDI phantom.	168
10-15	Mean organ doses for pediatric craniosynostosis protocol.	168
10-16	Organ doses measured using the pediatric phantom and craniosynostosis protocol	169
10-17	Number of low-contrast objects viewed using pediatric craniosynostosis protocol parameters.	170
10-18.	Mean organ doses resulting from brain perfusion protocol.....	171
10-19	Mean and maximum organ doses in mGy measured with adult brain perfusion protocol.	172
10-20	Mean organ doses in mGy resulting from adult cardiac protocol.....	173
10-21	Mean and maximum organ doses in mGy resulting from adult cardiac protocol.....	174
10-22	Organ dose comparison for the 320-slice CT pediatric craniosynostosis protocol between measured doses (mGy) and Monte Carlo (MC) simulated doses (mGy).	175
10-23	Organ dose comparison for the 320-slice CT adult brain protocols between measured doses (mGy) and Monte Carlo (MC) simulated doses (mGy).....	176
10-24	Organ dose comparison for the 320-slice CT adult cardiac CTA protocols between measured doses (mGy) and Monte Carlo (MC) simulated doses (mGy).....	176

LIST OF FIGURES

<u>Figure</u>	<u>page</u>
2-1 Illustration used for the body protocols	34
2-2 Example of the acquisition table from a body protocol.....	34
2-3 Two image reconstruction tables are depicted for a body protocol.....	34
2-4 Reformation section of a neuroradiology protocol.....	35
2-5 Portion of CT ENT protocol	35
3-1 Illustration of angular tube current modulation	44
5-1 Standard CTDI phantoms	60
6-1 Pediatric tomographic phantom	69
6-2 Adult male tomographic phantom.....	70
6-3 Diagram of the low-contrast module of the image quality phantom.....	71
7-1 Representation of x-ray tube positions used for measurements.....	79
7-2 Dosimeters suspended perpendicular to the anode-cathode axis.....	80
7-3 Setup to measure beam profile parallel to anode-cathode axis.....	81
8-1 nanoDot dosimeters	95
8-2 Energy response, dose rate response and scatter response surface setup	95
8-3 Setup of scatter response.....	97
8-4 Diagram of cross-sectional view of ion chamber and dosimeters	96
8-5 Setup of in-phantom angular response.....	97
9-1 Pediatric phantom with surface dosimeters to measure skin, eye and breast doses	109
9-2 Placement of skin and lens dosimeters on the forehead and lens of the eyes on the adult phantom for the brain perfusion protocol.....	111
9-3 Dosimeter placement in the esophagus, measured in three slices of the adult phantom from the brain perfusion protocol.....	112
9-4 Locations of dosimeters within the thyroid.....	112

9-5	Locations of the dosimeters within the brain.....	113
9-6	Locations of dosimeters within the breast to capture scattered radiation.	113
9-7	Cardiac R-R cycles are shown with exposure conditions	114
9-8	Placement of dosimeters in the lungs.....	116
9-9	Placement of dosimeters within the stomach.....	117
9-10	Placement of the dosimeters to measure skin dose across the breasts.....	117
9-11	Locations of dosimeters for breast dose measurements using the cardiac CTA protocols.....	118
10-1	Total filtration of x-ray beam using the large filter and depicted for three beam qualities.....	150
10-2	Total filtration of x-ray beam for small and large filters using a 120 kV x-ray tube voltage.....	151
10-3	Effect of bowtie filter on total filtration measurements.....	152
10-4	Radiographic image of the 16-cm nominal beam width.....	153
10-5	Beam profile of the 16-cm nominal CT x-ray beame.....	154
10-6	Normalized dose in air across the CT scanner gantry perpendicular to the anode-cathode direction.....	155
10-7	Normalized dose in air across the CT scanner gantry in the anode-cathode direction. ...	156
10-8	Measurement of DRK counts.....	157
10-9	Measurement of CAL counts.....	158
10-10	Measurement of LED counts	159
10-11	Percent decrease from initial dose	160
10-12	Response of the OSL dosimeters to increasing dose rates.....	163
10-13	Linearity of the energy-corrected dosimeter doses.....	164
10-14	Linearity response of the OSL dosimeters to increasing tube currents, representative of the range of doses measured.....	165
10-15	Linearity response of the OSL dosimeters and ion chamber to increasing tube currents, representative of the range of doses measured.....	166

10-16	Dose absorbed by the nanoDot dosimeters, in air, as a function of x-ray tube angle.....	167
10-17	Dose absorbed by the nanoDots in the head phantom, displayed as a function of x-ray tube angle.....	168
10-18	Image quality phantom images for pediatric protocol.....	169
10-19	Image quality phantom images for cardiac protocol.....	175
A-1	Example of a body protocol.....	185
A-2	Example of a cardiac protocol.....	186
A-3	An example of an ENT protocol.....	188
A-4	Example of a neuroradiology protocol.....	189
A-5	Example of an MSK protocol.....	191

Abstract of Dissertation Presented to the Graduate School
of the University of Florida in Partial Fulfillment of the
Requirements for the Degree of Doctor of Philosophy

ORGAN DOSE MEASUREMENTS FROM MULTIPLE-DETECTOR COMPUTED
TOMOGRAPHY USING A COMMERCIAL DOSIMETRY SYSTEM AND TOMOGRAPHIC,
PHYSICAL PHANTOMS

By

Lindsey K Lavoie

August 2009

Chair: Manuel Arreola
Major: Medical Physics

The technology of computed tomography (CT) imaging has soared over the last decade with the use of multi-detector CT (MDCT) scanners that are capable of performing studies in a matter of seconds. While the diagnostic information obtained from MDCT imaging is extremely valuable, it is important to ensure that the radiation doses resulting from these studies are at acceptably safe levels. This research project focused on the measurement of organ doses resulting from modern MDCT scanners.

A commercially-available dosimetry system was used to measure organ doses. Small dosimeters made of optically-stimulated luminescent (OSL) material were analyzed with a portable OSL reader. Detailed verification of this system was performed. Characteristics studied include energy, scatter, and angular responses; dose linearity, ability to erase the exposed dose and ability to reuse dosimeters multiple times. The results of this verification process were positive. While small correction factors needed to be applied to the dose reported by the OSL reader, these factors were small and expected.

Physical, tomographic pediatric and adult phantoms were used to measure organ doses. These phantoms were developed from CT images and are composed of tissue-equivalent materials. Because the adult phantom is comprised of numerous segments, dosimeters were placed in the phantom at several organ locations, and doses to select organs were measured using three clinical protocols: pediatric craniosynostosis, adult brain perfusion and adult cardiac CT angiography (CTA). A wide-beam, 320-slice, volumetric CT scanner and a 64-slice, MDCT scanner were used for organ dose measurements. Doses ranged from 1 to 26 mGy for the pediatric protocol, 1 to 1241 mGy for the brain perfusion protocol, and 2-100 mGy for the cardiac protocol. In most cases, the doses measured on the 64-slice scanner were higher than those on the 320-slice scanner.

A methodology to measure organ doses with OSL dosimeters received from CT imaging has been presented. These measurements are especially important in keeping with the ALARA (as low as reasonably achievable) principle. While diagnostic information from CT imaging is valuable and necessary, the dose to patients is always a consideration. This methodology aids in this important task.

CHAPTER 1 INTRODUCTION

The issue of the apparent increased risk of cancer incidence and mortality from radiation doses resulting from computed tomography (CT) scanning has been widely addressed in the radiology community recently. Among these concerns are the documented increase in the number of scans done in the past few years as compared to those a decade ago and especially those from pediatric CT exams.¹ Similarly, as the dose from CT exams has become such a widely-discussed and publically debated topic, a brief description of relevant studies is appropriate.

1.1 Increased Use of Computed Tomography

A reliable source of data which can be used to determine the number of medical procedures done in a time period is the reimbursement payment data. Mettler conducted an institutional study that analyzed medical billing data for CT studies from 1990 through 1999.¹ Within this nine-year span, there was a 58% increase in the total number of diagnostic procedures. In 1990, CT scans made up 6.1% of all radiology procedures. Almost a decade later, 11.1% of exams were CT studies, which contributed to 70% of the total dose to patients from all radiology exams. Furthermore, the study also found that most patients had more than one CT study on the same day. While the ordering of extraneous exams should not be condoned, it must be realized that many CT exams require more than one series for proper diagnosis (i.e., a three-phase liver exam for the diagnosis of a liver mass or a pre-transplant evaluation). In the realm of pediatric radiology, Brenner reported a 92% increase from 1996 to 1999 in the number of abdominal and pelvic exams performed on patients under 15 years old.²

In 2009, the National Council on Radiation Protection and Measurements (NCRP) published a report detailing different sources of radiation to which the United States population

was exposed.³ Of all sources of exposure included in the study, they reported CT for medical purposes contributes 24% of the total collective effective dose due to exposure to ionizing radiation. Within the medical modalities, CT comprises 49% of the total collective dose; according to the same report, this figure was only 3% in the 1980s.

In 2000-2001, the Conference of Radiation Control Program Directors, Inc. (CRCPD) conducted a Nationwide Evaluation of X-Ray Trends (NEXT)⁴ study and looked at the number and details of CT exams performed at medical institutions in the United States. In the year the data were gathered, 45.1 million CT procedures were done nationwide. Head CT exams were the most frequent, making up 33% of the total number of CT exams, while abdomen and pelvis CT exams made up 22% of the total number of exams and second to head exams in frequency.

While the statistics illustrated in these studies seem extreme, it is important to note that the increase in the number of CT studies is driven by advancing technology. As CT scanners have become faster and total scan time has been reduced, there is no longer the need for sedation in many cases, making a CT scan more feasible and efficient. Wide-beam CT has increased the total beam width, allowing entire organs to be imaged in one rotation of the x-ray tube in less than one second. The utility of CT as a diagnostic tool and the valuable, detailed information provided to physicians has significantly contributed to an increase in the total number of CT scans performed in the United States.

1.2 Effects on Pediatric Patients

The focus of a study by Brenner *et al.* was a pediatric population, and his conclusion was that the lifetime risk of radiation-induced mortality is larger when the patient undergoes the CT study at an earlier age; and that this risk then increases as age at exposure increases.² Younger patients have, in principle, a longer period of time in which to express the effect (in this case, cancer), and second, because the organs of pediatric patients are still developing; these rapidly-

dividing, growing cells are more sensitive to radiation than the same cells of the fully-developed organs of an adult patient.

In a more qualitative analysis, Brenner stated that for the same scan parameters, pediatric organ doses were typically higher than those in adults.⁵ Along with increased sensitivity to radiation and longer lifetime for expressing radiation-induced cancers, pediatric patients, compared to adults, have a smaller body size. Due to the geometry of CT and its full rotation around isocenter during exposure, a given organ of interest will be found in a position distal to the x-ray tube at some point during the scan. At such a time, there is partial shielding of the organ by the anatomical structures lying in between the x-ray tube and the organ of interest. In a pediatric patient, this shielding is considerably less than in an adult, strictly due to the smaller size of a child, with less shielding between the x-ray tube and the aforementioned organ. When organs are in a closer position to the x-ray tube after a half-rotation, they are exposed in a similar manner for adult and pediatric patients, and thus, the total dose to the organ is higher in a smaller pediatric patient than in a larger adult.

Brenner was careful to point out the “caveats” of the group’s dose calculations. As with most radiation-effect risk estimates, the data were derived from documentation from atomic bomb survivors who received significantly higher doses than those observed in CT. Thus, extrapolation is necessary, and while the accepted linear-no-threshold model applies, there were very little data in the dose range relevant to a CT exam and its possible effects. Finally, Brenner’s calculations were overestimates because adult protocols were used in the dose calculation which in general implies a higher tube current value. Brenner cited several studies that have offered suggestions on clinical ways to reduce pediatric doses and admitted that none of these techniques were accounted for in his study.

One of Brenner's conclusions concentrates on the fact that, while the reported organ doses seem large, there is a very small percentage increase in the risk of radiation-induced cancer when compared to the natural background. While this translates to a small increase in the risk to an individual, Brenner claims these doses are not a matter of concern for personal health, but instead are of concern for public health. Although the risk per person is small, the number of people in the population who are undergoing CT exams has steadily increased, which has brought up the issue of appropriateness and usage, topics of immense interest to the radiological and medical communities. One way to address this issue is through education of physicians on a more careful ordering of CT exams.

1.3 Specific Aims

Because of the current relevance of the increased number of CT studies in the United States and the apparent higher radiation doses resulting from CT studies, it was the goal of this research project to develop a methodology for measuring organ doses resulting from clinical CT protocols. To this end, the following specific objectives were proposed:

- a) Develop clinical CT protocols. With involvement of experienced radiologists and CT technologists, protocols were to be developed based on clinical indications and by asserting scan parameters necessary to achieve adequate clinical image quality required for each protocol as defined by radiologists. Dose considerations were to be an essential part of the protocol development process.
- b) Verify commercial dosimetry system. A commercially-available optically-stimulated luminescence (OSL) dosimetry system, which can be used in a clinical setting, was to be verified for accuracy and reliability. Among the characteristics of the system to be investigated were energy, angular and scatter responses, accuracy, reproducibility, ability to erase trapped energy and reusability.

- c) Characterize the beams of a 320-slice CT scanner. As these wide-beam scanners were the latest in CT technology, methods were to be developed to characterize these wide x-ray beams. The characteristics to be evaluated were reproducibility, tube voltage, half-value layer, beam width, and beam profiles.
- d) Measure organ doses. Three clinical CT protocols were to be used to measure organ doses resulting from wide-beam CT scanning using a 320-slice CT system. Patients were to be simulated using physical, tomographic phantoms developed by the Nuclear and Radiological Engineering group at the University of Florida (UF). Small, OSL dosimeters were to be used to measure the doses to selected organs on and in these phantoms.
- e) Compare organ doses. Organ doses were to also be measured on a 64-slice multiple-detector computed tomography (MDCT) system. Protocols similar to those of the 320-slice scanner were to be used for organ dose measurements using the same physical phantoms.
- f) Evaluate image quality. A simple, low-contrast detectability test was to be assessed as a feasible image quality indicator for the clinical protocols selected for d) and e) above. It was to be investigated if possible changes in acquisition parameters could be suggested that could result in a dose reduction while maintaining adequate levels of image quality.

CHAPTER 2 CLINICAL CT PROTOCOLS

As described in Chapter 1, the objectives of this research project were to utilize actual clinical protocols for organ dose measurements, rather than measuring doses for arbitrary combinations of scanning parameters, which may be unrepresentative of actual clinical doses. Two adult protocols were chosen: one utilized to assess brain perfusion and a second that yields images of the heart using CT angiography (CTA). To address some of the concerns raised by Brenner regarding doses in pediatric CT, a pediatric head protocol was also selected. Throughout the course of this research project, these protocols, initially developed for the numerous MDCT scanners at Shands Hospital at UF, were redesigned to take full advantage of the newer technology of a 320-slice volumetric CT scanner purchased by the hospital in 2008. The adjustments made to the protocols were a collaborative effort of many members of the radiology department under the leadership of medical physicists, the process of which is detailed in this chapter.

2.1 Radiology Practice Committee

In response to the imperative needs of protocol standardization and workflow improvement, and to begin the process of implementing study appropriateness criteria, the Radiology Practice Committee (RPC) was formed at Shands Hospital at UF in October of 2005 with the main task of modifying existing CT and magnetic resonance imaging (MRI) protocols, and creating new ones when necessary. The committee was comprised of radiologists, the picture archiving and communications system (PACS) administrator, medical physicists, CT and MRI technologists, and radiology administrators. While both CT and MRI protocols were developed and edited, the scope of this document is only the CT protocol development process followed by the RPC.

The RPC set various goals in its charter, including the standardization of protocols in form and description and the improvement of workflow. The process was iterative in nature, with protocols being evaluated in small groups by the different radiology subspecialty sections under the leadership and guidance of the medical physicists. The following sections describe this complex and lengthy process.

2.2 Protocol Standardization and Revision

A standardized set of protocols improves workflow. As all involved steps are established clinically, the protocols can be used as a teaching tool for residents. In addition, they can further provide clinicians with the information needed to make an appropriate exam order based on clinical indication. When protocols are not standardized, they are frequently altered for each specific patient. While sometimes this modification is unavoidable, workflow is slowed down when a technologist needs to make changes to an existing protocol to suit the specific needs of a single exam. To further complicate the matter, clarification about the physician's orders is sometimes needed for the technologist to modify and accommodate the proper scan. As this process takes time to understand and finalize, patient throughput is compromised, with all of the negative ramifications on cost and patient care.

The process of standardization was accomplished in a variety of ways. First, radiologists on the committee were responsible for revising and setting anatomical and spatial scan parameters necessary for diagnosis, including slice thickness and spacing. Radiologists were also responsible for creating the list of clinical indications pertinent to each protocol. The role of the medical physicists was to make sure dose considerations were kept in mind. Finally, CT technologists were tasked with revising and establishing the technical and practical aspects of a scan, including the anatomical start and end points of the scan, the application of a breath-hold or

a specific breathing technique, oral and/or intravenous (IV) contrast agent administration and the appropriate timing of delayed scans, among others.

2.3 Clinical Indications in Protocols

One of the most important aspects of an imaging protocol is the clinical indications associated with that protocol, that is, the clinical reason for the study. While this list of indications may always be a “work-in-progress” due to the vast number of clinical indications, it serves as a starting point for the appropriateness of ordering a given CT exam. As all academic hospitals, Shands at UF has a large number of residency programs in many specialties. Thus, a properly-designed list of indications may be used by the least-experienced residents, who may be unsure of which CT exam is needed for a given patient indication. Allowing access to such a useful list of indications may also aid in reducing the number of inappropriate CT exams that are ordered every day. In fact, a secondary benefit of standardized protocols is the realization that CT may not be the most appropriate modality for a given diagnosis.

In order to facilitate and take full advantage of the efforts involved in the assignment of clinical indications to each CT protocol, a tool was developed to allow a search through the entire database of protocols for a given indication. Presented as a simple input text field, the user simply enters the indication, and any associated protocols within the database are returned. The softcopy version of the selected protocol is displayed, along with its full list of clinical indications. The importance and usefulness of such a tool is extraordinary and without precedent in the field of radiology.

2.4 Picture Archiving and Communications System

As digital imaging has become the standard in radiology departments across the country, a PACS provides essential storage and access to digital images. Network bandwidth, transmission times, and storage capacities are the main concerns of a PACS administrator and thus, his/her

involvement is indispensable, as the protocols must contemplate and take into account the number and size of the images generated in a given timeframe.

The number of images in a study is generally dictated by the modality and the specific exam. The size of each image depends on the number of pixels used during image acquisition.⁶ The number and size of these pixels are directly related to the resolution of an image; a larger number of smaller pixels results in an image with higher resolution than that with fewer and larger pixels, for the same displayed field-of-view (FOV). As an example, a typical chest exam involves two radiographs: one in the anteroposterior (AP) orientation and a second in the lateral position. The typical pixel matrix size of a digital radiograph is 2,000 x 2,000. The bit-depth, or number of bits per pixel, is 2 bytes. For CR images, there are 4096 (12-bit) gray scale values available for the image. Thus, roughly sixteen megabytes (MB) of storage is required for a 2-view chest exam. A CT exam, on the other hand, could involve anywhere between tens of images up to thousands of images. Despite having a smaller pixel matrix (512 x 512) than a CR radiograph, a standard chest CT study requires roughly 130 MB of space, assuming an average of 250 images. In summary, the larger number of images generated in a given CT study results in larger storage needs than for most other imaging modalities.

The RPC ensured that estimated study size be considered in the development of each protocol. Determination of slice thickness and spacing are two important parameters in protocols, and both directly affect the size of a CT study. When thinner slices are reconstructed, a larger number of images is necessary to cover the entire scan length; conversely, thicker slices generate fewer images for the same scan length. Important considerations include the level of detail needed for diagnosis, as well as the length of the scan. Radiation protection guidelines dictate that only the area of interest be scanned in CT study, thus limiting the number of images

that are generated as well as dose to the patient. As was the case in the entire development process, for each protocol, these tradeoffs were debated among RPC members, and the most appropriate and efficient values for such parameters were chosen by the committee.

2.5 Protocol Development Process

The following is a detailed description of the protocol development process. While all RPC members involved performed specific duties, it was the general leadership of the medical physicists that kept the committee focused on the task of updating and creating CT protocols. Specifically, RPC meetings were run by one of the medical physicists (i.e., the author, LKL). Weekly assignments were given to members by this physicist, who was responsible for updating protocol documents throughout the process. When necessary, this medical physicist coordinated among members so that each protocol was approved by the committee.

2.5.1 Database Development

To facilitate the redesign and organization of CT protocols while beginning implementation of a paperless process, a database was developed to store protocol-related information. In the database, each protocol has its own set of unique descriptors, the most relevant for clinical use being the Indications field to allow the search for a specific protocol, based on a known clinical indication. It was necessary that this field be dynamic, as the number of indications for a given protocol may be vast and may need to be updated frequently.

2.5.2 Protocol Template

Once the protocol database was established, the committee proceeded to develop a softcopy document for use by the CT technologists to use as a reference for each protocol. Templates were created for each anatomical body section, which efficiently condensed information in the database and displayed the protocol in a format most useful for the

technologists. Once completed, these templates were implemented online as the softcopy of each protocol and were made available for physicians to view.

2.5.2.1 Title and illustration

Each template is headed by the standardized protocol title, followed by a pictorial anatomical diagram of the body section of interest. These diagrams can be presented in axial, coronal or sagittal views, as necessary. For example, the body protocols depict an anterior anatomical view from the top of the neck through the femoral heads. The head and neck templates use only a lateral view of the entire skull and the neck through the cervical vertebrae. The protocol then illustrates the start and end points of the scan series by means of lines on the diagram, also indicating a cranio-caudal or caudo-cranial direction, with an anatomical reference. An arrow describes the direction of the table feed (in the case of helical protocols) with respect to the patient. Figure 2-1 depicts an example of the diagram used for CT body exams.

2.5.2.2 Acquisition parameter description table

Adjacent to the anatomical diagram is the acquisition table. An image acquisition refers to the actual process of scanning the anatomy of interest to generate raw data. Fields within the acquisition table include the following: patient position, respiration, contrast requirements, contrast medium requirements and timing, volume acquisition specifications, and the start and end point of the scan, as depicted in Figure 2-2. Multiple image acquisitions are labeled with different letters. In this example, there is only one acquisition, thereby denoted with the letter A in Figure 2-2.

2.5.2.3 Reconstruction parameter tables

The next set of tables in the protocol template contains the necessary reconstruction parameters. A reconstruction is defined as an image generated from the raw data of the CT acquisition. These tables include the type of algorithm used in processing the raw data (e.g.,

bone, lung, soft tissue), the thickness and spacing of the reconstructed images, and finally the FOV. Each reconstruction refers to the corresponding letter-labeled acquisition from which the raw data is processed. In the examples shown in Figure 2-3, the first table, labeled A1, is the first reconstruction (1) from the data obtained in acquisition A (shown in Figure 2.2), and it uses a soft-tissue algorithm. The second reconstruction, denoted A2, utilizes the lung algorithm but produces thinner images than the first reconstruction (3 mm thickness and spacing, as compared in 5 mm in A1). In both tables depicted in Figure 2-3, the FOVs denoted refer to the largest section of the patient within the anatomy to be imaged, and the FOV is increased by an additional 2 cm on each side of the patient; this increase in FOV is described as “patient largest +4 cm” in the table.

2.5.2.4 Reformation parameter table

The next section of the template is the reformation table. A reformation is an image set that is constructed from processed data of reconstructed images. The fields within the table are the same as those for the reconstructions, with the addition of the plane in which the images are reformatted (i.e., sagittal, coronal, axial, oblique). Both the reconstruction and reformation sections include a space for a diagram to illustrate the specified plane of the reformatted image. Some protocols have an anatomical diagram in the reformation section that depicts the FOV, or boundaries, for the reformation. In Figure 2-4, the coronal reformation begins at the tip of the nose but does not continue through the entire head, stopping around the condyle of the mandible.

2.5.2.5 Additional protocol information

Following the reformation table and diagram is a section for additional information related to the protocol labeled “Other”, intended to include information that may not have a specific place in the template. Special instructions or notes are placed here, as shown in Figure 2-5. Further examples of clinical CT protocols developed are found in Appendix A.

2.5.2.6 Indications

The final section of the protocol template is perhaps the most important and compiles a list of clinical indications associated with each CT protocol. Changes or updates to the indications are also updated in the protocol database. This section was closely and promptly maintained by the medical physicist, as the information on the protocol templates must be the same as that stored in the database.

2.5.2.7 Using the templates and updating the protocols

The next step in the protocol development and implementation process involved transferring the information from existing CT protocols into the database, as well as into the template of the corresponding body section. Initially, after the basic information was transferred, members of the committee reviewed the protocols for completeness, appropriateness and accuracy. One of the major changes made to the sets of previously existing protocols was the title. One goal of the committee was to consolidate protocols by separating the protocol name from its indication(s). For example, the protocol formerly titled “Liver Mass” was changed to “Three-Phase Liver” to allow the protocol to be used for indications other than the specific imaging of a liver mass.

A secondary caveat to the specific naming of the protocols is an initiative currently being pursued by the Radiological Society of North America (RSNA),⁷ in conjunction with the American College of Radiology (ACR),⁸ with the final objective of standardizing words and accepted standardized names used in diagnostic radiology. Termed RadLex, the goal of this RSNA initiative is to implement this standard list as a national standard so that all institutions use the same terminology. The protocol titles adopted by the RPC follow the RadLex nomenclature whenever available, as the RadLex project is a work-in-progress and not yet complete.

Efforts were also made to keep all of the protocol parameter tables independent of the CT manufacturer and model. For example, the major CT manufacturers do not always use the same terminology to describe functions or parameters of the scanner. The localizing tomograph acquired at the start point of each CT scan have manufacturer-specific names, such as topogram, scanogram, scout view and pilot scan.⁹ Similarly, different scanners may follow different scan sequences for a given protocol. One scanner may perform a torso acquisition protocol in one scan, while another scanner will break the acquisition into separate sections. The images are still sorted, displayed and viewed in the same order, but the acquisition sequence is different between the two different scanners.

2.6 Protocol Website

A website was developed to allow physician access to the CT and MRI protocols online.¹⁰ A list of all protocols is available, as well as a fully-functional indication search tool. In using the tool, the user types a clinical indication into the search text box. The results of the search are displayed in prioritized order for those that best match the term(s) in the text field. A result list may display a statement in red underneath the protocol title for some protocols. This statement is meant to further direct the user to the appropriate protocol or to alert him/her of the possible inappropriate selection of a protocol. The user is able to view each protocol within the search results by selecting the protocol title. Many revisions to this search tool have been necessary as the process of creating a complete list of indications by clinical specialty occurs in a cumulative manner, and the addition of clinical indications will be continual.

Although the RPC is still continuing work to further develop this website, the ground work is complete. The power of this tool is tremendous; it provides physicians with two resources to aid in the process of appropriately ordering a diagnostic imaging exam. First, the search by indication tool may be used to aid the physician in choosing the best exam based on the

particular indication of a given patient. Second, the physician is able to view all details of the indicated protocol. This standardization of protocols based on clinical indication improves the quality of patient care, while optimizing workflow and proper use of resources.

The implementation of the CT protocols at UF is complete and has been a success. Although small edits are still necessary, these are minor compared to the scope of the project. Furthermore, these are dynamic protocols, deliberately designed to allow for the continued development in technology which will ultimately drive major revisions and updates of existing protocols. The RPC committee has put into place a structured process to allow for these advancements.

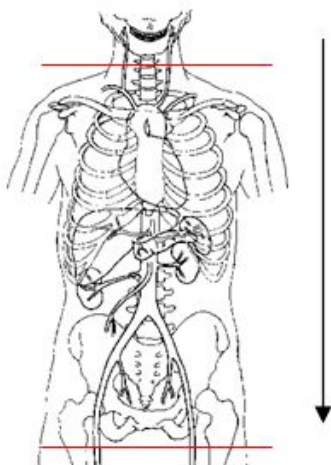


Figure 2-1. Illustration used for the body protocols, with lines showing the start and end points of the scan as the thoracic inlet and pubic symphysis, respectively; the scan direction is cranio-caudal.

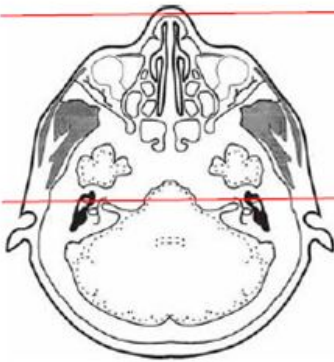
	Patient Position	Supine
	Contrast	Oral: dilute, 4 cups IV: up to 100 ml
	Injection Rate	2 ml/sec
	Respiration	Breath hold
	Volume	Appropriate to achieve images as specified in following reconstruction tables.
	Acquisition Specs	
A	general venous	Begin Thoracic inlet
	50-60 sec delay	End Pubic symphysis

Figure 2-2. Example of the acquisition table from a body protocol. The letter A in the Begin line notes the first acquisition for the protocol.

A1	Algorithm	Soft tissue	A2	Algorithm	Lung
	Thickness	5 mm		Thickness	3 mm
	Spacing	5 mm		Spacing	3 mm
	FOV	Patient largest + 4 cm		FOV	Patient largest + 4 cm

Figure 2-3. Two image reconstruction tables are depicted for a body protocol. A1 and A2 use different algorithms, slice thickness and slice spacing. Patient largest + 4 cm denotes an increase in the FOV of 2 cm on each side of the patient.

REFORMATION



A2R1	Algorithm	Bone
	Thickness	1 mm
	Spacing	1 mm
	F.O.V.	To be specified by tech
	Plane	Coronal

Figure 2-4. Reformation section of a neuroradiology protocol, depicting a diagram for reformation boundaries on the left, and the associated reformation table on the right.

OTHER

For retinoblastoma **initial work up only** add through eyeballs recon FOV as in A1 above.

Ret	Algorithm	Soft
	Thickness	1.0 mm
	Spacing	1.0 mm
	<u>F.O.V.</u>	160 – 180 mm

Figure 2-5. Portion of CT ENT protocol, depicting the use of the “Other” section for specific protocol notes.

CHAPTER 3 MULTIPLE-DETECTOR COMPUTED TOMOGRAPHY

Invented in 1972 by Godfrey Hounsfield and Allan Cormack independently, CT was designed to solve the problem of the superimposition of anatomical projections in clinical laminar tomography. This problem is a result of the process of projection radiography, which generates two-dimensional images of three-dimensional objects. In addition, poor tissue contrast results from this superimposition of anatomy.

The goal of CT is the improvement of tissue contrast by generating images of two-dimensional nature which do not contain images of over- or underlying structures. A true cross-sectional view of the scanned anatomy gives the radiologist improved tissue contrast, as well as depth information never before seen on a two-dimensional radiograph.

CT has greatly improved since 1972. With complete rotation times of less than a half-second and single-scan coverage up to 16 cm, it is easy to see how CT has become such a useful clinical tool. A history detailing the progression of scanners can be found elsewhere.^{6,9} Below is a discussion of the relevant CT scanning parameters pertaining to this research project, including their definitions and clinical impact. Many of the aspects of CT that are outlined in this chapter were considered by the RPC during protocol development. While some dose reduction techniques, such as tube current modulation, were already in place as part of the implemented protocols, other techniques, specifically tube voltage reduction, were investigated during this research project.

3.1 Detector Array Systems

In MDCT, small, multiple detectors make up the detector array. The minimum slice thickness is determined by the width of the individual detector elements.¹¹ However, the individual slice thickness may be greater than the individual detector widths because multiple

channels can be selected for data acquisition. The detector configuration is generally described as the product of the number of data channels and the width of the detector rows within the channel. For example, a detector configuration of 4 x 1.5 mm represents four slices that are 1.5 mm thick. The total scanned volume coverage per rotation is determined by the physical collimation of the x-ray beam.

3.2 Modes of Acquisition

There are two modes of acquisition in CT: axial and helical. While scanners of today are capable of both, it was only in the 1990s that technology allowed for the inception of helical scanning. These modes of acquisition are described briefly below.

3.2.1 Axial Data Acquisition

Early generation scanners were limited by electrical cables that supplied the x-ray tube with the required electrical power and cables that transferred data from the detector array to the data processing unit. This combination allowed one full rotation of the x-ray tube and detector at a time. One slice in the axial plane was acquired and the cables wound up, the table was incremented (i.e. advanced) to the next position, and the next slice was acquired as the cables unwound.⁹ However, in the 1990s, slip-ring technology was developed that allowed the x-ray tube and detector to rotate continuously in the gantry, overcoming the limitation of needing to stop acquisition for a table increment before the next rotation. This development reduced the time needed in between acquisitions, but data acquisition was still limited by the time required for the table to advance through the gantry.

3.2.2 Helical Data Acquisition

During helical CT acquisition, the table advances continually through the gantry during the x-ray exposure. Thus, in the patient's frame of reference, the x-ray tube follows a helical path around the patient. Slip-ring technology also resulted in faster rotation times, all of this helping

to reduce the total scan time as compared to axial acquisitions, for which time is needed between exposures for the table to move.

3.2.3 Volumetric Data Acquisition

The constant advancement of MDCT scanners, with the objective of faster scanning and wider coverage has led to the advent of wide-beam scanners, like the 256-slice Philips Brilliance (Philips Medical Systems, Aurora, IL) and the 320-slice Toshiba Aquilion ONE (Toshiba American Medical Systems, Tustin, CA), to address the clinical implications of complete organ coverage in a single scan. As indicated in previous chapters, an Aquilion ONE scanner was installed at Shands Hospital at UF in 2008 and thus, it was one of the focuses of this research project. The detector elements in the Aquilion ONE are 0.5 mm x 0.5 mm,¹² and the total cone angle of the x-ray beam is 15.2°. A nominal x-ray beam width of 16 cm enables complete coverage of entire organs,¹³ such as the brain and heart, in one axial rotation of the x-ray tube and detector array. To appreciate the clinical usefulness of this design, consider the case of brain perfusion studies. A contrast agent is administered to the patient, and, at the appropriate time, a scan of the entire brain is captured at once, generating “temporally-uniform,”¹⁴ volumetric data, from which a variety of images can be reconstructed. A dynamic volume study is performed by scanning the brain at specific time intervals to monitor the progress of the contrast agent through the arterial and venous phases. Anatomic information is generated by differences in tissue attenuation, while functional information is calculated using the time characteristics of the flow of the administered contrast agent. Perfusion capabilities have been available on 64-slice systems for a few years; however, only a 3.2 cm section of the brain is scanned at a time to capture perfusion data. The ability to acquire uniform volumetric information of the entire brain is a breakthrough for improving the information available in a clinical setting. However, comparison of doses from such wide beams with those from scans covering the same volume

with narrower beam widths is necessary. This research project assessed organ doses resulting from clinical scans using both a wide-beam volumetric CT scanner and a 64-slice MDCT scanner to determine if there was significant discrepancy in doses resulting from these scans of different total beam widths.

3.3 Clinical CT Considerations

3.3.1 Slice Thickness

Slice thickness is one of the most important parameters of a CT scan, and has significant image quality and file size implications such as transfer times and storage. There are many factors to consider in determining the most appropriate scanned and reconstructed slice thickness of a given protocol. Thin slices yield improved spatial resolution along the Z-axis (assuming all other scan parameters remain constant). Conversely, thin slices suffer from a decrease in the signal-to-noise ratio (SNR), due to the smaller number of photons collected per detector element. For a given volume, thin acquisition slices also result in an increased number of images, putting a potential strain on the network and minor impacts on the image storage system, namely the PACS archive. Due to the numerous tradeoffs between thin and thick slices, it should be the clinical need of the CT scan that dictates the scan parameters.

3.3.2 Image Reconstruction

Once the raw data are acquired with MDCT, images can be reconstructed in different combinations, depending on the clinical needs of the study. For example, the data from a 4 x 1.5 mm acquisition may be reconstructed to one 6.0 mm slice, 2 slices that are 3.0 mm thick, or the original acquisition of 4 slices that are 1.5 mm thick. While this allows for flexibility, it is not recommended to reconstruct to a slice thickness that is thinner than the acquisition thickness: data interpolation is necessary to achieve this goal, and the results are not of full integrity.

3.4 Dose-Reduction Techniques

As CT technology continues to produce newer and better systems, it is important to keep in mind that the basic principles of x-ray imaging remain true and that dose considerations follow the ALARA (as low as reasonably achievable) principle. While there are numerous techniques to reduce CT dose, the main three are lowering the tube current (mA), dynamic tube current modulation and reduction of tube voltage. At a given kV, the tube current, along with the total time of exposure, determines the total number of x-ray photons produced by the x-ray tube, sometimes referred to as the mAs. Since the dose delivered to the patient is proportional to the number of photons incident to the anatomy, any adjustment in mA (assuming all other parameters remain constant) directly affects the delivered dose.

The total number of photons and therefore the tube current also directly impact the level of noise in an image, visually described as the mottle in an image. Mathematically, random noise in a digital image is expressed as the square root of the mean number of x-ray photons reaching the imaging detector.⁶ Because mAs determines the number of x-ray photons in the CT x-ray beam, it directly affects the amount of noise in the image. The acceptable noise content in a clinical image is dictated by the observing radiologist, as noisy images can negatively affect diagnosis, thus resulting in the well-known tradeoff between dose to the patient and image noise.

3.4.1 Tube Current (mA) Adjustment

CT protocols are pre-programmed into the scanner by applications personnel of the manufacturer and lead CT technologists. This process is necessary to streamline the performance of CT studies, since the manufacturer-loaded study parameters are generic to apply to the average patient. X-ray photon attenuation is affected by the size of the patient; larger patients attenuate a larger number of photons than a smaller patient, when the same exposure parameters are applied. In many cases, the mA may be lowered for a smaller patient and because

of this reduction in size (and therefore attenuating material), an adequate number of photons will still reach the detector. A study on pediatric chest CT reported that adequate image quality was achieved with a low-dose protocol using 25 mAs and resulted in a dose reduction of 90% compared to the standard protocol that used 250 mAs.¹⁵ Manual reduction of mA, depending on patient size, is one method of dose reduction in CT.

3.4.2 Tube Current (mA) Modulation

A second option for dose reduction involves using different mAs values at a constant kV throughout a single CT scan series. X rays are continuously emitted from the x-ray tube as it rotates around the patient. Attenuation profiles are collected at the detector at different angles and reconstructed to produce a cross-sectional image. Tube current modulation refers to adjustments made to the mA during one CT exposure to decrease the dose to the patient while maintaining acceptable noise levels, and therefore, image quality.

As the CT x-ray beam rotates around the patient, the amount of x-ray transmission through the patient changes. When the tube is in a lateral position, x-rays are absorbed to a greater degree than when the tube is in the AP/PA position because, in general, a patient is thickest in the lateral direction, as depicted in Figure 3-1. Automatic tube current modulation increases the tube current to increase the photon transmission through the thicker part of the patient and decreases it to transmit through thinner sections. Because the noise of an image is dictated by the region of greater attenuation and decreased photon fluence at the individual detector, the tube current is lowered when the x-ray tube is at the AP position to maintain patient dose at lower levels with little degradation in image quality. The two techniques of mA modulation are angular, or X-Y modulation and Z-axis modulation.

3.4.2.1 Angular (X-Y) tube current (mA) modulation

Angular mA modulation refers to adjustments to the tube current made by the CT scanner to account for differences in attenuation in the x-y imaging plane of the patient,¹⁶ i.e., the scan plane. While different manufacturers have different names and methods for angular mA modulation techniques, the general approach is the same. One approach involves an “on-the-fly” adjustment in which the scanner utilizes fluence information from projections with a 5-degree range to decide if an adjustment to the current is required for the next 5 degrees. Other simple approaches utilize information from the two perpendicular localizing tomographs performed before each CT image acquisition. Based on this attenuation data, the mA is modulated as a function of x-ray tube position with respect to the patient during the scan.

3.4.2.2 Z-axis tube current (mA) modulation

Tube current may also be modulated in the Z-axis,¹⁶ or along the superior-inferior axis of the patient. Using this technique, the operator selects a nominal noise level acceptable for the CT study in question. Information is again obtained from a localizing tomograph from which the scanner automatically computes the necessary approximate variations in mA values needed throughout the scan to obtain that desired noise level. The Toshiba Real E.C. software uses the AP/PA tomograph to calculate a thickness of water that attenuates an equivalent amount of photons as the patient at different positions along the Z-axis. As the patient and table translate through the CT scanner during image acquisition, the mA is modulated to produce the same level of noise in all images, regardless of the size and shape of the anatomy being scanned.

3.4.3 Tube Voltage

One technique for dose reduction, used extensively in the case of pediatric patients, is a decrease in the x-ray tube voltage.¹⁷ It has been shown that diagnostic-quality images can be produced using lower tube voltages for pediatric patients.¹⁸ Because pediatric patients are

smaller in size than adults, there is less tissue attenuating the x-ray beam as compared to an adult when the same scan parameters are used, thus dose decreases as the tube voltage decreases. Furthermore, a lower tube voltage shifts the x-ray energy spectrum downwards in such a way that photoelectric absorptions are more prominent and away from Compton scattering, enhancing the tissue contrast of the image.¹⁷ One must be careful in this task, however, as more significant beam hardening artifacts may occur in the CT image as a result of a lower tube voltage.¹⁸ Beam hardening occurs when lower energy photons are preferentially absorbed by an attenuating material, thus increasing the effective energy of the x-ray beam compared to the initial beam entering the material. This process results in an artificial brightness at the edges of the material in a CT image and a darkening at the center.⁶ As described by Cody *et al.*, the 80 kV tube voltage setting was eliminated from their institution because significant beam hardening artifacts were prevalent and affected the diagnostic quality of the images. They were, however, able to use 100 kV in place of 120 kV in patients up to 12 years of age for both chest and abdominal studies. In the case of an abdominal study, this reduction in tube voltage from 120 kV to 100 kV resulted in a 40% reduction in dose. This example highlights the importance of recognizing the balance between dose and image quality. Dose reduction techniques fail if a scan needs to be repeated because of poor image quality. While patients should be exposed to the lowest doses as possible, images must be of diagnostic quality.

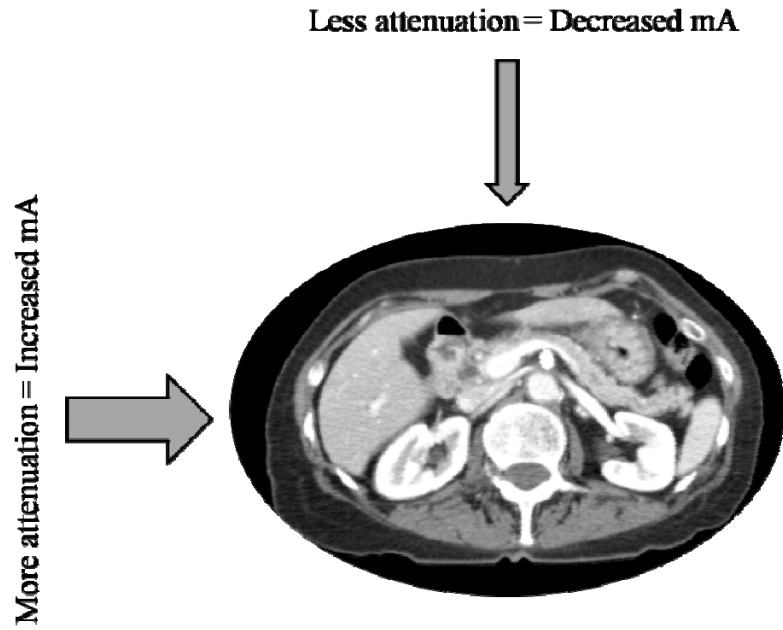


Figure 3-1. Illustration of angular tube current modulation, depicting an increase in photon transmission in the AP direction and decrease in the lateral direction. Adapted from M.K. Kalra, M.M. Maher, T.L. Toth, B. Schmidt, B.L. Westerman, H.T. Morgan, and S. Saini, "Techniques and applications of automatic tube current modulation for CT," *Radiology*. **233**, 649-657.

CHAPTER 4 COMPUTED TOMOGRAPHY DOSE DESCRIPTORS

Because one aim of this research project was the measurement of organ doses, definitions of appropriate dose quantities are appropriate. Discussed in this chapter are the standard definitions of terms relevant to this project, as accepted by the appropriate bodies, mainly the National Council on Radiation Protection and Measurements (NCRP)¹⁹ and the International Commission on Radiological Protection (ICRP).²⁰

4.1 Definitions

4.1.1 Kerma

Kerma is an acronym for “kinetic energy released in matter” and describes the events that occur when ionizing radiation passes through matter.⁶ In the case of x rays, the two-step process begins with indirectly-ionizing photons transferring energy to kinetic energy of charged particles via Compton scattering and the photoelectric absorptions. These charged particles, in turn, deposit energy in matter through ionization and excitation. Kerma is the amount of kinetic energy transferred from the photons to direct ionization. The Standard International (SI) unit of kerma is J kg^{-1} , termed gray (Gy). From this definition, it is clear that kerma does not present information on the amount of energy transferred to the irradiated matter.

4.1.2 Absorbed Dose (D)

Absorbed dose is the mean energy imparted by ionizing radiation ($d\varepsilon$) to a given mass (dm).²⁰ Absorbed dose is the most fundamental unit of radiation dose. The mathematical expression of absorbed dose is shown in Equation 4-1. The SI unit of absorbed dose is also the Gy.

$$D = \frac{d\varepsilon}{dm} \tag{4-1}$$

4.1.3 Equivalent Dose (H_T)

Equivalent dose was developed by the ICRP as a radiation protection quantity used for the purpose of defining limits of radiation exposure.²⁰ The product of the average absorbed dose (i.e., the absorbed dose averaged over a volume) and a radiation weighting factor (w_R) yields the equivalent dose, as shown in Equation 4-2.

$$H_T = \sum_R w_R D_{T,R} \quad (4-2)$$

The radiation weighting factor describes the degree of biological damage produced by different types of directly and indirectly-ionizing radiation, and it is based on the relative biological effectiveness (RBE),²⁰ which is defined as the ratio of the absorbed dose from a reference radiation to that of a given radiation, both producing the same biological effect.²¹ Photons have a radiation weighting factor of unity.

4.1.4 Effective Dose (E)

Effective dose expresses the risk to an individual member of a population exposed to a uniform whole-body irradiation that is equivalent to that of a partial-body or organ exposure. Numerically, it is the summation of the individual products of the equivalent organ doses and the individual tissue- and organ-weighting factors. The ICRP²⁰ defines the tissue-weighting factor as the quantity expressing the contribution of a tissue or organ to the total body detriment from stochastic effects. Values of tissue weighting factors are listed in Table 4-1. The expression of effective dose is given by Equation 4-3.

$$E = \sum_T w_T \sum_R w_R D_{T,R} \quad (4-3)$$

4.2 Effective Dose as a Dose Descriptor

The effective dose has been historically used to describe the dose associated with a radiation exposure. Thus, a brief discussion of the quantity, its usefulness, its limitations, and possible alternatives for medical applications is pertinent.

4.2.1 Applications of Effective Dose

As previously stated, the effective dose is the sum of the average absorbed dose to tissues and organs, weighted to reflect the degree of biological detriment to a given tissue or organ. Generally speaking, effective dose is used when comparing the relative biological radiation detriment among different radiological procedures. Thus, effective dose may be a useful measure in the process of improvement of radiological procedures that involve partial or non-homogenous irradiations.

4.2.2 Limitations of Effective Dose as a Patient Dose Descriptor in CT

While effective dose is clearly a useful quantity in many circumstances, especially when comparing the risk of biological detriment from different diagnostic x-ray procedures, one is tempted to apply its theory to doses for particular patients. Below are several arguments against this idea.

4.2.2.1 Population-based risk

Because of its risk-based definition, effective dose is relevant when assessing risk to populations, while assessing the risk to individuals is limited by its scope. Such is the case in a diagnostic x-ray exam.²² Similarly, it is relevant only when the exposure conditions are the same as those under which the risk factors have been derived.²² For example, the ICRP formulation of effective dose was derived from considerations of both the working population and the general population which is not intentionally exposed. According to the definitions of these populations, a patient does not fall into either of these categories since a patient is intentionally exposed. In addition, not all population groups, including patients, can fit into broader definitions. For example, elderly patients receiving diagnostic radiology exams are at a lower risk of radiation-induced effects than the average population simply because their age allows less time for any effects to develop.²³ On the other hand, pediatric patients have a much higher risk than the

general population for the opposite reason; their still-growing organs are more radiosensitive, and the probability of development of biological detrimental effects is greater because of their potentially longer life span than that of an average member of the public.

4.2.2.2 Tissue-weighting factors

The ICRP defined the tissue weighting factors so that the factor associated with a given tissue or organ would represent the fraction that such organ or tissue contributes to the total biological effect to the body. These values are displayed in Table 4-1. Thus, the summation of the weighting factors is equal to unity to account for the entire body. In the case of non-uniform, or partial-body irradiation, the definition of the effective dose is such that organs which are not irradiated do not contribute at all to the total body detriment estimate.

4.3 Recommendations

The ICRP states in its 2007 recommendations²⁰ regarding medical exposure of patients that either the equivalent dose or the absorbed dose to irradiated tissues or organs can be used as good estimates of radiation exposure to patients. Even in the case where effective dose is the most commonly used descriptor, the ICRP states that it is more appropriate to determine organ doses separately, rather than simplify the situation by assuming a whole-body irradiation.

Similarly, McCollough and Schueler²² suggest that the best approach to a patient dose estimate is to estimate separately and as accurately as possible all pertinent organ doses and apply the most appropriate risk factor for such organs. When necessary information is unavailable to conduct such a calculation, they suggest that a Monte Carlo (MC) simulation be used. This approach is suggested because, if the definition is followed strictly, calculation of the effective dose requires direct measurement, or at least an estimate, of the dose to each individual organ and tissue. In practice, it is difficult to accomplish this task. Direct measurement of organ and tissue doses is a practical impossibility since dose measurements in that case would have to

be calculated or estimated, rendering the effective dose an estimate, rather than an assessment. Physical phantoms, as the one used in this research project, typically are not full-body phantoms, or they do not facilitate placement of dosimeters in all organs. Thus, they limit the assessment of all organ and tissue doses. MC simulations, as suggested above, can be utilized in place of actual measurements, but such an approach is outside the scope of this research project.

Thus, for the purposes of this work and under the conditions described, the assessment of effective dose is not only impractical, but it would lead to a large number of assumptions and approximations which would render the number meaningless. Instead, reliable organ dose measurements were made in accordance with the aims of this research project.

Table 4-1. Tissue-weighting factors.²⁰

Tissue	w_T	$\sum w_T$
Bone-marrow (red), colon, lung, stomach, breast, remainder tissue*	0.12	0.72
Gonads	0.08	0.08
Bladder, esophagus, liver, thyroid	0.04	0.16
Bone surface, brain, salivary glands, skin	0.01	0.04
	Total	1.00

* Remainder tissues: adrenals, extrathoracic (ET) region, gall bladder, heart, kidneys, lymphatic nodes, muscle, oral mucosa, pancreas, prostate, small intestine, spleen, thymus, uterus/cervix.

CHAPTER 5 COMPUTED TOMOGRAPHY DOSE INDEX

Historically, doses in CT have been expressed by and referenced to a quantity known as the computed tomography dose index (CTDI). Therefore, a description of the CTDI and its various definitions, uses and limitations are presented in this chapter.

5.1 CTDI Definitions

The CTDI was originally proposed by Shope *et al.*²⁴ in 1981 as a method to standardize CT dose estimates. At the time, there were many measurements and techniques available; Shope's goal was to set a benchmark. There are also many factors that contribute to the complex dose distributions in CT. Scan motions, filtration, varying detector collimations and scan parameters all differ among manufacturers. As a standard method was necessary, the CTDI (without its numerous subscripts) was proposed as a "quick and convenient" estimate of dose from a CT scan, so that the dose from different scanners could be compared in a consistent manner.

5.1.1 MSAD

The first quantity specifically designed to represent the radiation dose resulting from exposure of the patient to the rotating x-ray beam in the geometrical conditions of CT was the multiple scan average dose (MSAD). The MSAD describes the limiting value of a dose profile obtained when multiple single-slice axial CT scans are acquired over a given length. As the number of scans increases, the subsequent scatter tails add to the dose on the central axis; the MSAD is approached when the distance between the first and last scans of the series is large enough so that these two scans do not contribute to the dose at the central axis. The MSAD was developed to describe the complex dose distributions of clinical scans; measurement of the MSAD along the length of a scan consisting of multiple rotations of the x-ray tube describes the

dose distribution along the length of the scan. Numerically, Shope²⁴ defines the MSAD in Equation 5-1 as,

$$MSAD = \frac{1}{I} \int_{-I/2}^{I/2} D_{N,I}(z) dz \quad (5-1)$$

where I is the distance between the central axis of each scan N is the number of scans.

5.1.2 CTDI

The CTDI is defined as the “dose as a function of position along the Z-axis co-ordinate for a single scan dose profile at a given point.”²⁴ The numeric integral is inversely proportional to the slice thickness, integrated over infinity and expressed in Equation 5-2, as

$$CTDI = \frac{1}{NT} \int_{-\infty}^{\infty} D(z) dz \quad (5-2)$$

where N is equal to the number of tomography slices in the acquisition, and T is equal to the width of the scanning beam in the Z-direction. The product NT is equivalent to the nominal slice thickness. The CTDI is then “equal to the average dose along the Z-axis at a point over the central scan of a series of scans,”²⁴ as long as the distance between each scan is held constant. This definition ensures that if enough scans are acquired in such a way that the contributions from scatter from adjacent slices is included, the dose profile levels out and remains consistent throughout the scanned length, regardless of the number of scans further added.²⁴ CTDI measurements are much more convenient than the numerous point dose measurements required for an actual calculation of the MSAD.

5.1.3 CTDI_{FDA}

Since the time Shope initially introduced the concept of the CTDI, further modifications to the CTDI have been defined, each with a different motivation and purpose. The first modification was made by the Food and Drug Administration (FDA), as it formally adopted

CTDI as the parameter to describe doses in CT, realizing that the integral over infinity in the definition of the CTDI was not practical, and also that the dose was dependent on the scan thickness and the scattering medium.²⁵ In establishing regulatory definitions on how to measure the CTDI, two cylindrical phantoms were introduced: one with diameter of 16 cm to represent an average adult head, and the other 32 cm in diameter to simulate attenuation and scatter from an average adult torso. Both phantoms are made of polymethyl methacrylate, better known as PMMA, and 15 cm in length. These phantoms are depicted in Figure 5-1, along with rods used to fill cylindrical sockets in the phantom, created for placement of a dosimeter. At the time, the length of these phantoms guaranteed that all scattered radiation within the phantom (resulting from a thin axial slice) would be included in the measurement. A standard pencil chamber with a 100-mm active length was used in conjunction with these phantoms to measure $CTDI_{FDA}$, defined in Equation 5-3 below.

$$CTDI_{FDA} = \frac{1}{NT} \int_{-7T}^{7T} D(z) dz \quad (5-3)$$

The limits of integration were assigned as $\pm 7T$ because the maximum beam width used in CT at the time was 10 mm, thus ensuring that all of the scatter produced within the phantom from a single 10 mm axial slice was collected by the pencil chamber. However, as CT evolved into helical first, and late MDCT and systems with greater beam widths, these integration limits became obsolete.

5.1.4 $CTDI_{100}$

With the objective to extend the applicability of the CTDI concept to varied slice thicknesses and scanners, the $CTDI_{100}$ was defined. Because the pencil chamber specified by the FDA has an active length of 100 mm, the $CTDI_{100}$ is defined with limits of integration that reflect this length, as shown in Equation 5-4.

$$CTDI_{100} = \frac{1}{NT} \int_{-50mm}^{50mm} D(z) dz \quad (5-4)$$

While this equation was meant to estimate the MSAD (section 5.5.1), $CTDI_{100}$ underestimates the MSAD when beam widths wider than 10 mm are used because not all of the scatter tails of the scan are collected and measured by the pencil chamber.

5.1.5 $CTDI_w$

Due to the geometry of a CT acquisition, the dose distribution is not uniform across a single slice. Except at the center of the cylindrical CTDI phantoms, the attenuation characteristics at any other points on the phantom are different, because of the additional attenuation resulting from the patient table and other factors. Clearly, such is also the case with a patient. To account for these variations, a weighted CTDI value was defined²⁶ as indicated in Equation 5-5.

$$CTDI_w = \frac{1}{3} CTDI_{100,center} + \frac{2}{3} CTDI_{100,edge} \quad (5-5)$$

The first term in the equation refers to the $CTDI_{100}$ value measured in the center of the PMMA phantom and the latter to the average of the measurements made at the four peripheral positions. The weighted CTDI is often used as an indicator of dose across the scanned field-of-view, because the CTDI measured at different positions within the phantom can vary.¹¹

5.1.6 $CTDI_{vol}$

The advent of helical scanning made it clear that none of the CTDI descriptors would adequately describe the dose resulting from a CT helical acquisition that may use a pitch value other than 1.0. Pitch is defined as the ratio of table travel during one rotation of the x-ray tube (I) to the total beam width ($N \times T$).¹¹ In this way, application of any of the CTDI definitions would yield the same numeric result regardless of whether an acquisition resulted in over-scanning

(pitch less than 1) or under-scanning (pitch greater than 1). Consequently, a modified definition called $CTDI_{vol}$ was introduced as stated in Equation 5-6.

$$CTDI_{vol} = \frac{NT}{I} \times CTDI_w \quad (5-6)$$

With the definition of pitch as the table increment per axial scan, a further simplification to Equation 5-7 is made.

$$CTDI_{vol} = \frac{1}{pitch} \times CTDI_w \quad (5-7)$$

5.2 Dose-Length Product

By definition, all but the original CTDI definitions are based on measurements on a standard phantom. Thus, the values so obtained are not representative of the actual dose deposited in a volume of a different size, shape, or scattering material than the PMMA head and body phantoms, nor can the CTDI values be considered accurate when not all of the scatter tails are accounted for or measured. As a dose estimate for a 100 mm scan (by virtue of the length of the pencil chamber), such CTDI values are typically applied for a clinical scan, whether its scanned length may be at of 10 mm or 1000 mm. In other words, the length of a clinical scan is not taken into account when using the CTDI as the dose descriptor. To rectify this situation, the dose-length product (DLP) was developed. The DLP, in units of mGy-cm, is described in Equation 5-8, where L is the scan length, in cm and the $CTDI_{100}$ is measured in mGy.

$$DLP = CTDI_{100} \times L \quad (5-8)$$

The evolution of the CTDI, and all of its associated derivations, has spanned over the past three decades. As CT technology has continued to advance, it has been necessary for the imaging community to adapt the definition of CTDI to best describe the actual dose that results from a CT scan. Because of its simple measurement process, CTDI remains an acceptable and

efficient tool in comparing the output of different CT scanners and to track the performance of a scanner over time. However, it presents certain limitations, as described in the next section.

5.3 Analysis of the Applicability of the Measurement of CTDI and DLP

In recent years, there has been much discussion within the radiology community regarding the measurement of the computed tomography dose index (CTDI) with a standard “pencil” ionization chamber. The pencil chamber was originally proposed by Suzuki and Suzuki²⁷ in 1978 as a convenient way to measure the radiation output of a CT scanner in such a way that geometry and scatter would be included in the measurements. Such measurements would also allow for a relative comparison among scanners, as the measurement is representative of an average dose along the length of the chamber. The chamber was designed to be used with the PMMA CTDI phantoms. While the original concept behind the pencil chamber was adequate at the time it was proposed, the advancements in CT technology have brought up many limitations to the pencil chamber and the definition of CTDI.

5.3.1 Underestimation of Dose using CTDI in MDCT

In the early days of CT technology, the maximum 10 mm x-ray beam width was narrow enough that all scatter tails were indeed captured by the pencil chamber in a CTDI measurement. When the FDA²⁵ adopted the CTDI concept, the limits of integration were modified to $\pm 7T$ (section 5.1.3), which still encompassed the scatter tails of such narrow beams. However, CT technology has rapidly advanced: the number of slices per acquisition has increased, as have the maximum beam widths, a situation not contemplated in the various CTDI definitions.

As MDCT scanners allow wide beams, Dixon has shown that for a given 20-mm total beam width, a single axial measurement using a pencil chamber underestimates the dose in the central region of the body and head CTDI phantoms by 20% and 10%, respectively.²⁸ He further suggests that these discrepancies will only increase as the total beam width increases.

Boone²⁹ addressed the issue of increasing beam widths in a 2007 study that focused on the efficiency of the 100 mm length pencil chamber in capturing and accurately measuring the total dose deposited in a single axial CT scan of beam widths of 10, 20 and 40 mm. He defined the efficiency of the CTDI₁₀₀ value as the ratio of the dose deposited in a rod 100 mm in length (representing a pencil chamber) to the total dose deposited in a rod of infinite length. Using a Monte Carlo code to simulate energy deposition in the PMMA CTDI head and body phantoms, the CTDI₁₀₀ efficiencies in the center and peripheral holes of the head phantom were 82% and 90%, respectively, for a 120 kVp x-ray spectrum simulated. The corresponding efficiency values for the body phantom were 63% (center) and 88% (periphery). While these numbers highlight the vast ineffectiveness of CTDI₁₀₀ as a true dose descriptor, there was only a 1% decrease in the efficiency values when a 40 mm beam width was simulated. This result indicates that the dose measured by a pencil chambers for wide-beam MDCT systems is not representative of the actual dose.

5.3.2 Proposed Solutions

To address some of the inadequacies of the current measurement of CTDI, several groups have suggested different methodologies. The two main concepts considered include the design of phantoms of a length greater than 150 mm to provide sufficient scattering material to better represent a patient more closely and a small ionization chamber to measure dose.

5.3.2.1 Extended phantoms

The 2003 Dixon²⁸ study suggests that increased phantom lengths appear to be necessary in order to produce equilibrium scatter; however, an actual length is not suggested in that work. To this end, Mori *et al.*³⁰ manufactured phantoms of 900 mm length using the same PMMA material as suggested by the FDA.²⁵ By definition, the integration length of CTDI₁₀₀ is a total of 100 mm (50 mm on each side of the central Z=0 axis). Instead, this study used a 300 mm length pencil

chamber to investigate whether a longer integration range would accurately capture all of the dose profile (including scatter tails) of CT x-ray beams of increasing widths. The authors concluded that for nominal beam widths of 15 mm or greater, a standard length (150 mm) body phantom estimates the dose profile integral to be 84% of the true value when compared to that measured using a 900 mm length phantom. Because a 300 mm length pencil chamber was used in this study, the authors further suggest an integration range of 300 mm for the beam width investigated (20 mm) to estimate better an average dose profile integral.

5.3.2.2 Small-volume ionization chamber

In order to address this underestimation of dose, Dixon and Ballard³¹ make a recommendation to replace the pencil chamber with a small volume (0.6 cm³) Farmer chamber. The measurement is then performed on the central axis of either the body or head phantom, which are placed on the table of the CT scanner and allowed to translate through the scanner during the exposure. In this way, the chamber is directly measuring the dose accumulated at the center of the phantom as a result of a CT scan of a given length. Furthermore, the small ion chamber guarantees that the scan length is equal to the integration length.

Chapters 4 and 5 have clearly established the limitations of the various CTDI incarnations to describe, properly and faithfully, the doses resulting from the wide-beam MDCT scanners, as well as the practical limitations of measuring effective doses, which justifies one of the main aims of this research project to measure individual organ doses in physical phantoms as the best alternative to dose characterization in MDCT. However, not all of the concepts associated with the CTDI and effective dose are to be discarded, especially those which focus on scatter and beam width considerations. For example, the concept of the small-volume ion chamber as the most adequate way to perform measurements because it takes into account these issues was applied in this project by approximating the small-volume ion chamber with a commercially-

available, small-volume OSL dosimeter to estimate organ doses. The dosimeters approximate a small-volume ion chamber and are capable of measuring the dose accumulated in the organ of interest.



Figure 5-1. Standard CTDI phantoms. From left to right: body phantom, cylindrical rods and head phantom.

CHAPTER 6 INSTRUMENTATION AND PHANTOMS

This final chapter of background material is dedicated to the description of the dose-measuring devices and phantoms used throughout the course of this research project. Specifically included are the details of the various ionization chambers and a solid-state detector used for both the characterization of the CT x-ray beams and the verification of the OSL dosimetry system, as specified in aims (b) and (c) in Section 1.3. Also, a brief discussion of the different types of dosimetry phantoms, including the tomographic phantoms used in this research project, is given in this chapter.

6.1 Ionization Chambers

Ionization chambers are the standard instrumentation used by medical physicists in performing all types of measurements with ionizing radiation. The basic details of the principle operation of an ionization chamber are outside the aims of this project and are found elsewhere.³² Listed in this section are the ionization chambers, along with manufacturer-stated specifications and other information pertinent to their use in this research project.³³

6.1.1 A 6-cc Chamber

A 10X6-6 (Radcal, Monrovia, CA) ionization chamber with an active volume of 6 cm³ was used to measure air kerma. The usable range for the chamber is 0.01 μ Gy to 600 Gy, well within the limits of air kerma ranges measured throughout this research project. The chamber is calibrated by the manufacturer at 60 kVp, 2.8 mm of aluminum (Al) half-value later (HVL) and has an accuracy of $\pm 4\%$. The nearly-flat energy response of the chamber yields correction factors of approximately 0.98-1.00 from 20 keV to 150 keV. While this chamber is most commonly used to measure kerma in the diagnostic energy range, the design and size of the

chamber, when compared with those of the OSL dosimeters, limited its use in this research project.

6.1.2 A 3-cc Pencil Chamber

For measurements involving the PMMA CTDI phantoms, a 3 cm³ pencil chamber was used (10X6-3CT, Radcal, Monrovia, CA). This chamber was calibrated at 150 kVp and 10.2 mm Al HVL and has a manufacturer-specified accuracy of $\pm 4\%$. Similar to the 6-cc chamber described in section 6.1.1, the energy dependence is $\pm 5\%$ with a range of correction factors ranging from 0.98 to 1.02, for HVLs of 2 to 20 mm Al. The active length of this chamber is 10 cm and the reported dose is the integral dose over the active length. As discussed in Section 5.3, this 10-cm length does not capture all of the scatter tails that result from CT beam widths that are common today. Furthermore, a disadvantage of this chamber is the inability to assess CTDI on modern scanners that do not allow the user to utilize narrow beam widths necessary (i.e., ≤ 10 mm) to ensure that all scatter tails are captured by the pencil chamber.

6.1.3 A 0.6-cc Chamber

Because of the small size of the OSL dosimeters, a 0.6 cm³ chamber (10X6-0.6, Radcal, Monrovia, CA) was purchased for the purpose of comparing and benchmarking measurements made with such dosimeters under similar geometry conditions. This Farmer-type chamber was specifically calibrated by the manufacturer to the National Institute of Standards and Technology (NIST) beam code M100, which is defined as follows: moderately-filtered 100 kV beam with a 5.25 mm Al HVL.³⁴ This beam code was chosen because it best matched the characteristics of the CT beams used in this research project. The manufacturer-stated energy dependence of this chamber is $\pm 5\%$ from 40 keV to 1.33 MeV, resulting in correction factors ranging from 0.97 to 1.03 for the 20 keV to 500 keV subrange.

6.2 Solid-State Detector

A Barracuda X-ray Multimeter (RTI Electronics, Inc., Fairfield, NJ) was used to measure the total filtration of the CT x-ray beam (described in section 7.2.2). This measurement device, in addition to the Ortigo software (RTI Electronics, Inc., Fairfield, NJ) used with it, gives a direct read-out of the total filtration of the x-ray beam, in mm of Al, making such measurements quick and easy. The accuracy of this measurement is $\pm 10\%$, or 0.3 mm, whichever is larger, in the range of 60-120 kV.³⁵

6.3 Tube Voltage Meter

A 40X12-W Accu-kV sensor (Radcal, Monrovia, CA) was used to directly measure the accuracy of the nominal kV of the CT x-ray beams. This sensor has a manufacturer-stated accuracy of ± 1 kV, or $\pm 1\%$, whichever is larger. The range of this meter is 40 kV to 160 kV, adequate to cover the range of tube voltages used in this research project.

6.4 Dosimetry Phantoms

Over the years, a large variety of phantoms has been used for dosimetric purposes. There are two main types of phantoms used for estimating doses from radiological procedures. Both have advantages and disadvantages. The following sections describe these phantoms and justify the decision for using the anthropomorphic phantoms for this research project.

6.4.1 Stylized Phantoms

Stylized phantoms are designed based on simple mathematical shapes. They use three-dimensional surface equations to describe the main organs that make up the human body by using simple, general shapes. The organs are represented in generic, often realistic positions and orientations. For example, a leg is represented with a cylinder of a given length, while a sphere is used to represent the head. Because of the lack of detail and generic nature of these shapes, one advantage of these phantoms is that they can be used to sufficiently represent an average

adult. While this type of phantom may be adequate in some equivalent dose estimates, this lack of detail and the inadequate locations and orientations of the organ can be a source of error when estimating organ doses.³⁶

6.4.2 Tomographic Phantoms

Anthropomorphic tomographic phantoms can be developed using image sets from actual scans of patients from tomographic modalities such as CT and MRI. In this way, the actual shapes of organs and structures, and their relative positions and orientations, are captured by the image sets. Segmentation methods are generally used to define the contours of the organs from the image set. Throughout the past decade, a multi-disciplinary group at UF as developed a series of tomographic, computational and physics phantoms spanning various age ranges and including both genders.^{37,38} These unique tissue-equivalent phantom sets were generated from actual patient CT data and were physically constructed with tissue-equivalent materials.³⁹ Because of these attributes, the phantoms are tomographic in nature, and they are clearly well-suited for the measurement of organ and tissue doses in CT. The resolution of all organs defined in the phantom are limited only by the resolution of the CT or MR image sets from which the organ data were derived.³⁶ Conversely, the smaller voxels that provide good resolution negatively affect the signal-to-noise ratio (SNR) of the image. When a smaller number of x-ray photons (or hydrogen nuclei in the case of MR) is captured within a volume element (voxel), there is an increase in the noise of the image. The result is a “grainy” image which leads to less accuracy during the segmentation process. Furthermore, because tomographic phantoms use patient image sets, the phantoms created are more specific to the few patients from which the CT or MR data were acquired. While one may choose an image set that closely represents an average patient, the organs may not be as “average” in size and location as those defined in a

stylized model. However, the detail of the organs and their relative positions among each other in tomographic phantoms makes them the phantom of choice for organ dose estimates.

Two tomographic physical phantoms were used for organ dose measurements in this research project: a pediatric phantom, depicted in Figure 6-1 and an adult male phantom, shown in Figure 6-2. Details regarding the construction process of these phantoms, as well as the tissue-equivalent materials used for construction are given in Appendix B.

6.5 Phantom for Image Quality Evaluations

There are a number of methods used by medical physicists to assess image quality in a clinical setting. Certain quantitative measurements, such as signal-to-noise (SNR), can be made using data analysis software available on some image display and viewing stations. On the other hand, more qualitative measurements can be made using phantoms specifically designed for image quality assessment. Since both of these approaches are used, a brief discussion of their advantages and disadvantages is given, as well as justification for the method chosen for this research project to assess low-contrast detectability.

A quantitative approach to image quality is described by Rill *et al.*,⁴⁰ in which acrylic and aluminum phantoms were developed to approximate the attenuation characteristics of an adult chest. SNR measurements were made in three different locations in these phantoms, corresponding to landmarks of patient anatomy, and using a soft-copy display workstation to assess image quality in the clinical environment. A circular region of interest (ROI) was drawn at five locations and the mean pixel value was recorded for each of them. Noise was defined as the standard deviation of the pixel values of all five ROIs. Imaging parameters were assessed by calculating the differences in SNR from images acquired with different techniques. Such a method allows for image quality to be assessed without exposing patients to excess radiation

because phantoms are used instead. However, in order to implement dose-reduction techniques suggested by the authors, a follow-up evaluation of clinical images would likely be necessary.

In a more qualitative approach, Prasad *et al.*⁴¹ acquired CT chest images which were analyzed by experienced radiologists. A 5-point scale was used to assess the images for noise, contrast, sharpness and overall quality. A score of 0 was given to images considered to be of the worst quality, while a score of 5 was assigned to images of excellent quality. This method yields results that may be put into practice immediately because clinical patient images are used for analysis. However, this type of study requires approval by the Institutional Review Board (IRB) and, in this specific case, required that patients receive an additional amount of radiation because additional scans were acquired in order to compare standard CT imaging techniques with the low-dose techniques proposed by the authors.

The method chosen to assess image quality for two of the protocols in this study was similar to that described by McCollough and Zink.⁴² A phantom designed and manufactured specifically for image quality analysis in CT was used in their evaluation of the performance of a multi-slice CT system. The phantom was centered and aligned with the CT scanner gantry, images were acquired using various combinations of scan parameters and resulting images from different modules of the phantom were assessed.

While the tomographic phantoms used in this research project include many organs and tissues, they are limited from an image quality perspective because the phantoms are made of three tissue-equivalent materials. While this level of detail is adequate for the purpose of dose measurements, it was not adequate to evaluate image quality because of the lack of contrast among different tissues.

To assess image quality of two of the clinical protocols evaluated in this research project, as described in Chapter 9, the low-contrast detectability (LCD) module of an image quality phantom (Catphan 500, The Phantom Laboratory, Salem, NY) was utilized.⁴³ The phantom contains various sections to assess parameters such as slice thickness and spatial resolution, among others. In particular, the LCD section is 15 cm in diameter and 4 cm thick. Cylindrical rods are embedded in two circular patterns into 6 groups. Each of the outer three groups contains 10 rods of varying diameter: 2, 3, 4, 5, 6, 7, 8, 9, 10 and 15 mm, respectively. Each group has a different contrast level: 1%, 0.5% and 0.3%, and labeled A, B and C, respectively. All rods are 40 mm in length and, thus, these groups are called supra-slice groups because this length is wider than most beam widths in MDCT, excluding, of course, the wide-beam scanners such as the Aquilion ONE 320-slice scanner. The inner three groups, known as the sub-slice groups, each have 4 rods of varying diameter: 3, 5, 7 and 9 mm. These all have an identical 1% contrast level. Unlike the outer groups, the sub-slice groups contain rods of varying length: 3, 5 and 7 mm, and are labeled D, E and F, respectively. MDCT scanners with 16-slice capabilities and up clearly have beam widths larger than these sub-slice groups. As example of a CT image of the LCD section of the Catphan is presented in Figure 6-3.

Typical LCD assessments are done in a subjective observation manner. Images of the LCD sector are obtained using kV and mAs values, as predetermined by the observer, using the thinnest acquisition slice possible and reconstructed using a soft-tissue algorithm and a reconstruction thickness also predetermined by the observer. Scoring of the phantom is done under dimmed-light conditions and optimal window and level settings, as determined by the user. The number of objects resolved completely (i.e., those for which the circular margins are

evident) are identified and counted. The results can be presented in various ways, as described in Chapter 10.

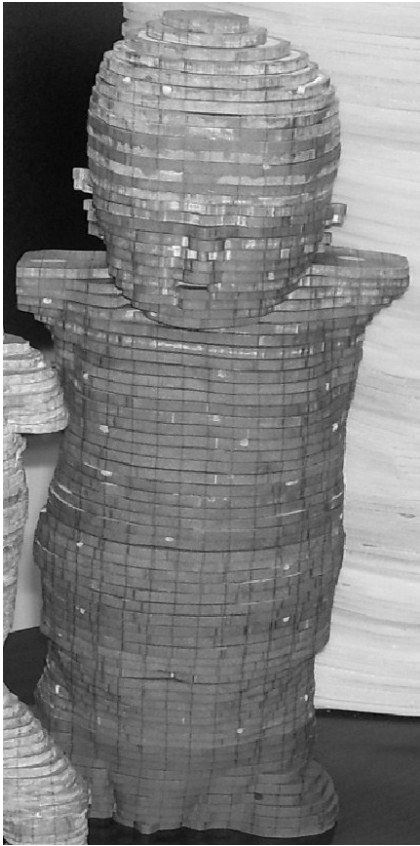


Figure 6-1. Pediatric tomographic phantom, developed from CT data of a 9 month-old patient.



Figure 6-2. Adult male tomographic phantom.

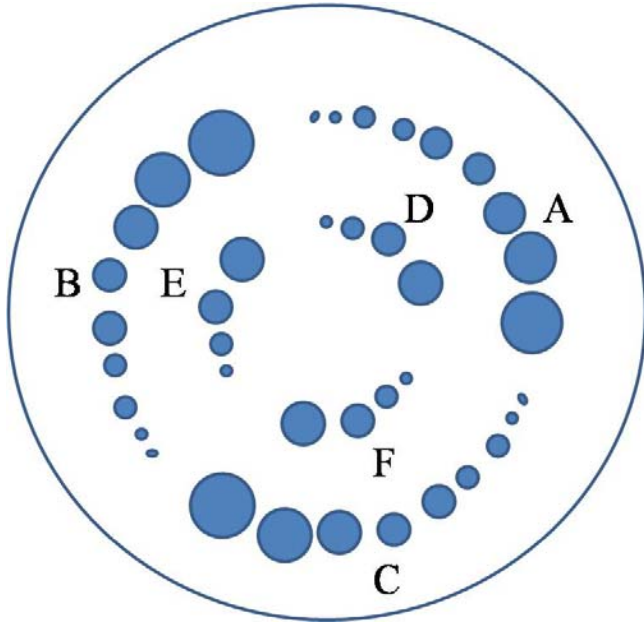


Figure 6-3. Diagram of the low-contrast module of the image quality phantom. Sections A-C are the supra-slice groups and D-F are the sub-slice groups. Adapted from “Catphan 500 & 600” brochure, The Phantom Laboratory. Available at <http://www.phantomlab.com/catphan.html>.

CHAPTER 7 CHARACTERIZATION OF X-RAY BEAMS OF THE VOLUMETRIC CT SYSTEM

Only a handful of 320-slice scanners are currently in use for both clinical and research purposes worldwide. No publications describing the complete characteristics of the x-ray beams for these scanners exist to date. Thus, a characterization of the MDCT systems (Aquilion ONE and Aquilion 64, Toshiba America Medical Systems, Tustin, CA) used for this research project was necessary. Though the evaluation of the Aquilion 64 was rather limited in scope (HVL and kV accuracy), that for the Aquilion ONE included exposure reproducibility, kV accuracy, total filtration, HVL, beam width, and dose profile measurements. For some of these measurements, specifically the beam width and dose profile determinations, well-known established methods for scanners of narrower beam widths were modified to accommodate the 160 mm full beam width of this scanner. The results of this characterization are presented in Section 10.1.

7.1 Exposure Reproducibility

7.1.1 Service Mode

In addition to the measurement of organ doses for selected clinical protocols using the 320-slice scanner, as described in Chapter 9, the scanner was also used to verify the dosimetry system (Section 8.2). During the dosimetry system verification, the scanner was mostly operated in service mode, which allows the user greater flexibility in the selection of exposure parameters, and most importantly, the capability of making exposures with the x-ray tube in a stationary (i.e., non-rotating) mode, a feature unavailable in clinical mode.

To investigate exposure reproducibility in this service mode, 0.6 cc ionization chamber, described in Section 6.1.3, was placed on 5.1 cm of acrylic slabs at the center of the CT x-ray beam. Ten exposures were made using identical scanning parameters, and the air kerma was measured. The mean and standard deviation of the ten measurements were calculated.

7.1.2 Clinical Mode

While most of the scan parameters of a clinical protocol are either selectable or visible to the user, one that remains unknown in present-day scanners is the actual position of the x-ray tube (i.e., the angle in the gantry) when the exposure actually begins. The three clinical protocols studied as part of this research project, described in Chapter 9, include either a single axial rotation of the x-ray tube to acquire one volume of data, or multiple axial rotations without any table motion to acquire several volumes. Some protocols also include helical scans, and so this type of acquisition was also reviewed.

Reproducibility in the clinical mode was assessed using two types of clinical protocols: volumetric (Craniosynostosis, Section 9.1.1) and helical (Head without Contrast). For both protocols, the CTDI head phantom was placed in the center of the gantry. The 3-cc pencil chamber described in Section 6.1.2 was used to measure the dose at all positions within the phantom. Ten replicate measurements were made at each phantom position for the volumetric protocol, while three were made for the helical protocol. The mean and coefficient of variation (CV) were calculated for each set of measurements.

7.2 Beam Quality

The quality of an x-ray beam affects both the patient dose and image quality, the two main aspects of interest in a diagnostic imaging protocol. Beam quality is characterized by tube voltage, total filtration and HVL. X-ray tube voltage was measured at the four tube voltage settings available on the scanner: 80, 100, 120 and 135 kV. Total filtration measurements were made to assess the effects of the different types of bowtie filters used in the CT system. HVLs were measured at all beam energies and using three different bowtie filters.

7.2.1 Accuracy in kV

Because photoelectric absorption and Compton scatter are energy-dependent processes, the attenuation characteristics of a tissue are quantitatively represented by the attenuation coefficient of the tissue. This quantity is dependent on the energy of the x-ray beam that passes through the tissue. In general, when a lower tube voltage is selected for a given exposure, the overall lower energies present in the x-ray spectrum result in more tissue contrast in the image because the relative differences among attenuation coefficients are larger than in the case of higher energy spectra due to the larger number of photoelectric absorptions which take place at lower energies.⁶ On the other hand, when lower tube voltages are used, images suffer from decreased transmission of x-ray photons through the irradiated material as compared to higher tube voltages, thus, resulting in lower photon transmission and a smaller amount of photons reaching the detector elements. Because of these reasons, the importance of the accuracy of the voltage selected cannot be overstated.

The accuracy of the nominal tube voltages was measured using the kV sensor described in section 6.3 with associated radiation measurement system (9095, Radcal Corporation, Monrovia, CA). The sensor was placed at the scanner isocenter, and the x-ray tube was positioned stationary at the top of the gantry (12 o'clock position), as depicted in Figure 7-1. For each voltage available, an exposure was made, and the measured kV was recorded.

7.2.2 Beam Filtration in CT

Due to the circular geometry of a CT scanner, the overall beam attenuation is non-uniform as the x-ray beam passes through the anatomy of interest during a scan. Thus, the x-ray beam is non-uniformly attenuated and hardened as it rotates around the patient.⁹ The central rays of the fan beam pass through the middle, thickest section of the body and experience greater attenuation and hardening. The outer rays of the fan beam pass through the edges of the body,

where the thinner anatomy results in less attenuation and hardening. This difference in attenuation and hardening of the x-ray beam negatively affects the reconstruction of the image. In addition, projection measurements through the center of the patient result in a decreased number of transmitted photons as more photons are attenuated through its thick section. The lower number of detected photons for those projections, as compared to the peripheral sections, results in a decrease in the signal-to-noise ratio. In order to compensate for the non-uniform beam hardening and attenuation resulting from differences in transmitted intensities, a beam compensating filter is placed close to the x-ray tube within the gantry. This bowtie filter,⁹ named after its particular shape, effectively attenuates and hardens the x-ray beam to a greater degree at the edges of the beam, as compared with effect at the center of the beam, where the distance between the x-ray source and the subject is the shortest possible and the amount of attenuating material is the largest.

Several bowtie filters are found in MDCT scanners today; clinically, the selection of a particular bowtie filter is dependent on the tube voltage and more importantly, the field-of-view (FOV) selected. Clearly, larger FOVs require a wider filter to cover the entire fan beam scanning the anatomy. Correspondingly, a small filter is used for brain imaging because of the small diameter of the head. A larger filter is used for cardiac imaging because the diameter of the thoracic region is much greater than that of the head and therefore requires a larger filter to provide uniform beam characteristics.

An attempt was made to obtain specific information, such as the materials of these bowtie filters, but such information was deemed as proprietary by the manufacturer in spite of a cooperative agreement being in place and a non-disclosure agreement signed by the author. In order to investigate the characteristics and effects of these filters, the total filtration of the x-ray

beam was measured at points across the gantry using a solid-state detector described in Section 6.2. The CT x-ray beam was collimated to approximate the size of the detector. An initial measurement was made at isocenter; the detector was then moved in 2 cm increments across the gantry out to 24 cm from isocenter along the diameter of the gantry aperture. Because filters are assumed to be symmetric, only one set of measurements was made across one half of the gantry. Measurements were made at three nominal tube voltages: 80, 100 and 120 kV and for two filters: Small-S and Large-L with one exception; due to limitations of the solid-state detector, measurements could not be made using the Small-S filter at 80 kV along the gantry, with the only successful measurement at isocenter.

7.2.3 Half-Value Layer

The HVL of an x-ray system is defined as the thickness of a given material needed to attenuate the x-ray beam to one-half of its initial intensity. A 6-cc ionization chamber, described in Section 6.1.1, and readout unit (9095, Radcal, Monrovia, CA) was used to measure the air kerma in a standard HVL measurement procedure. The x-ray tube was positioned at the bottom of the scanner gantry (6 o'clock) and held stationary during each exposure. A lead shield with a small aperture was placed in the CT gantry between the x-ray tube and the ionization chamber to collimate the beam to approximately the size of the chamber in order to attain good geometry conditions. Standard first HVL measurements were performed: the initial measurement was made without filtration in the beam, followed by exposures made with increasing amounts of 1100 aluminum alloy filters of known thickness placed on top of the lead collimating device. Measurements were performed at 80, 100, 120 and 135 kV for the Small-S, Medium-M and Large-L filters in place for each of the tube voltages. HVLs were measured at the center of the field, i.e., corresponding to the center of the bowtie filter.

7.3 Beam Width

Actual beam width measurements were conducted for a 160 mm nominal width using a computed radiography (CR) imaging detector (AGFA CR MD4.0, AGFA, Teterboro, NJ) 35 cm x 43 cm in size. A 1 mm copper filter was placed between the x-ray tube and imaging plate to attenuate the x-ray beam and better match the exposure expected by the CR imaging plate. The image was processed by a CR digitizer (CR85-X, AGFA, Teterboro, NJ) using a flat-field algorithm and analyzed using the Image J (National Institutes of Health, Bethesda, MD) software analysis program. A beam profile was generated across the mid-point of the CT x-ray beam. The gray scale value was plotted as a function of distance. The beam width was calculated using the full width at half-maximum (FWHM) of the profile.

7.4 Dose Profile

7.4.1 X-Axis

In order to measure the intensity of the x-ray beam and create a beam profile, the Landauer OSL nanoDot dosimeters (described in Chapter 8) were positioned suspended at isocenter across the gantry opening of the CT scanner. Dosimeters were placed adjacent to each other and centered vertically in the gantry using the alignment lasers, as depicted in Figure 7-2. The x-ray tube was positioned at 90° in the gantry (3 o'clock position) and kept stationary during the exposure; the orientation of the x-ray tube with respect to the strip of dosimeters was intended to create a beam profile (x-ray intensity as a function of distance) in the scanning plane of the fan beam. The dosimeters were exposed and analyzed by the OSL reader (Chapter 8).

7.4.2 Z-Axis

The nanoDot dosimeters were positioned at isocenter in order to measure the x-ray beam profile in the anode-cathode direction of the x-ray tube and determine if any heel effect could be observed. The heel effect is an intensity gradient which is the result of the preferential

attenuation of the x-ray beam towards the anode side of the x-ray field by the anode itself.⁶ The angulation of the target causes photons to travel different distances through the anode towards the image detector and therefore the intensity is lower at the anode side than at the cathode side.

Nineteen dosimeters were placed in line to cover approximately 19 cm of the beam which had a nominal width of 160 mm (0.5 mm x 320 detector rows). One row of dosimeters was centered horizontally in the gantry. Other rows were placed 8 cm above and below the center line. This setup is depicted in Figure 7-3.

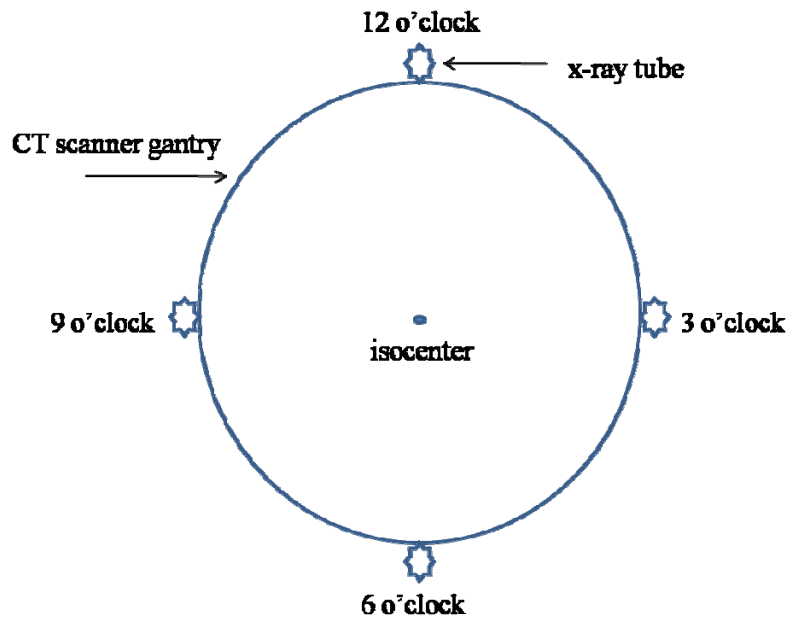


Figure 7-1. Representation of x-ray tube positions used for measurements. The star-like shape represents the x-ray tube.



Figure 7-2. Dosimeters suspended perpendicular to the anode-cathode axis, spanning only the top half of the gantry because of symmetry of the fan beam.

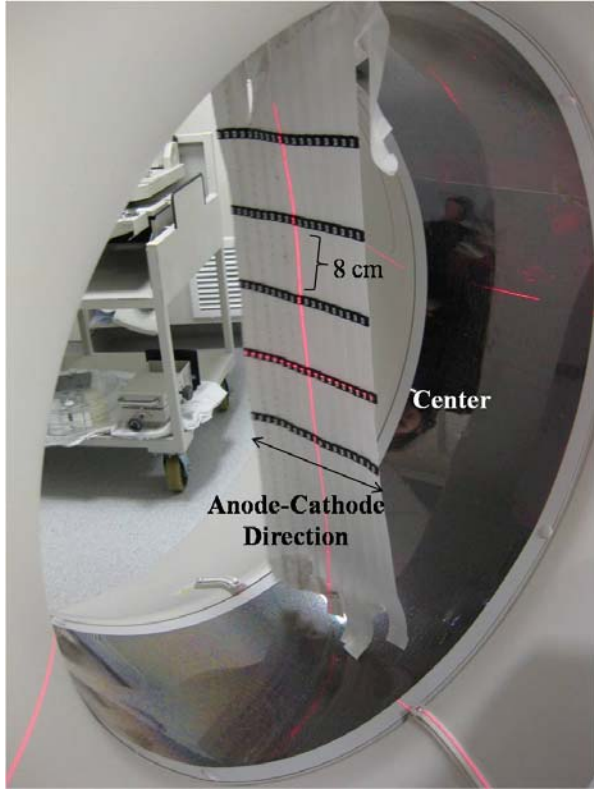


Figure 7-3. Setup to measure beam profile parallel to anode-cathode axis.

CHAPTER 8 OPTICALLY-STIMULATED LUMINESCENT DOSIMETERS

For the past few years, optically-stimulated luminescent (OSL) dosimetry has been adopted as the technology of choice in personnel dosimetry, and its use has now extended to clinical applications.⁴⁴⁻⁴⁷ The OSL process is similar to that of thermoluminescence (TL), with the primary difference that an optical stimulus is used in OSL instead of a thermal or heat stimulus (as is the case in the TL process) to induce post-exposure luminescence of the irradiated material. In the typical OSL reader, after irradiation, light emitting diodes (LEDs) supply the optical energy which releases the OSL signal, which is proportional to the dose absorbed by the dosimeters. This chapter details the methods of verifying the use of this system in the low-energy radiation fields used in diagnostic radiology.

8.1 Optically-Stimulated Luminescence

OSL has recently been evaluated for its use in dosimetry, as it offers great advantages over other conventional dosimetry systems. Only a small amount of OSL material is needed to capture sufficient numbers of photons during exposure to ionizing radiation, making small dosimeters possible, a useful feature for radiation dose estimates. Other positive characteristics include reusability, no observable dose-rate dependence and good spatial resolution. Jursinic conducted a thorough study in 2007 characterizing OSL dosimeters made by Landauer, Inc. (Glenwood, IL) for the high-energy radiation fields used in radiation oncology.⁴⁵ Among the properties he studied were angular and energy response, erasure using different light sources and signal depletion with repeated exposures. All measurements were conducted using x-ray beams with energies of 6-15 MV produced by a linear accelerator. Several others have performed studies similar to Jursinic utilizing high beam energies used in radiotherapy.^{48,49} The results reported by Jursinic and others imply that these OSL dosimeters are good candidates for

radiotherapy dosimetry. However, no similar study has been conducted to date in the lower energy range used in diagnostic radiology to determine whether the same advantages of OSL technology used in radiotherapy apply in diagnostic radiology.

8.1.1 Disadvantages of TL Dosimeters

While TLDs (thermoluminescence dosimeters) have been common in dosimetry for decades, there are many disadvantages to their use in clinical radiology.⁴⁷ It has been shown that the sensitivity of a TLD is dependent on the heat rate at which it is stimulated post-irradiation; as the heat rate increases, the sensitivity decreases. In addition, a lengthy annealing process is associated with each use of a TLD,⁴⁶ which limits practicality in clinical situations. Finally, correction factors need to be applied for characteristics such as a non-linear dose response, angular dependence, time between irradiation and readout, beam quality characteristics of the irradiation and attenuation of the actual TLD holder.

8.1.2 Advantages of OSL Dosimeters

The material used in OSL dosimeters is carbon-doped aluminum oxide ($\text{Al}_2\text{O}_3:\text{C}$). Because of its high sensitivity, only a small amount of material needs to be used in making a single dosimeter for adequate dose absorption, which has several advantages. First, the physical size of the dosimeter can be small, therefore increasing spatial resolution and localization of the dose measurement.⁴⁶ Second, depending on the method of readout, only a small amount of luminescence is necessary per readout, allowing a large amount of charge to be retained within the material which is available for subsequent readouts of the same exposure.⁵⁰ While a disadvantage of a TLD is its sensitivity to light, this can be turned into an advantage with OSL dosimeters. By encasing $\text{Al}_2\text{O}_3:\text{C}$ in a light-tight holder, the exact absorbed dose is held by the material. After readout, exposure to white light effectively erases the remaining signal within the $\text{Al}_2\text{O}_3:\text{C}$, and the dosimeter is ready for reuse.

8.2 Characterization of OSL Dosimetry System

A commercial dosimetry system (microStar, Landauer, Glenwood, IL) that employs OSL technology was acquired for its potential use in estimating doses resulting from CT scans. The microStar system uses small-sized dosimeters to capture and reports the shallow dose equivalent, also known as $H_p(0.07)$ and defined as the shallow dose equivalent at a depth of 0.07 mm in ICRU tissue.⁵¹ These nanoDot dosimeters (Landauer, Glenwood, IL), depicted in Figure 8-1, have specifications of 5 mm diameter, approximately 0.2 mm thickness and 10x10x2 mm³ holder dimensions. The diameter stated corresponds to the primary side of the dosimeter; the light-tight holder covers a very small amount of OSL material found on the back, or secondary side of the dosimeter. As the OSL process is stimulated by white light, care must be taken to shield the dot dosimeters from white light after use. Each dosimeter is uniquely identified by a barcode on the underside of the dot dosimeter. Thus, the dosimeter to be read can be simply scanner into the system. Each dosimeter is assigned its own sensitivity as determined by the manufacturer. The nanoDot dosimeters used in this study had a manufacturer-specified sensitivity of 0.91 and 0.93, respectively. The sensitivity is included in the readout value reported by the microStar system.

8.2.1 Other Radiation-Measuring Devices

Relevant exposures were made on a 32-slice CT scanner (Aquilion 32, Toshiba America Medical Systems, Tustin, CA) and a 320-slice CT scanner (Aquilion ONE, Toshiba America Medical Systems, Tustin, CA). Air kerma measurements were performed with a 6-cc ionization chamber and a 0.6-cc ionization chamber, both described in Section 6.1. The methods of individual tests are presented in the following sections.

8.2.2 Tracking of System Standards

The microStar reader uses two LED beams of different intensities to read the signal on the OSL material after exposure to radiation.⁵² The weak LED beam is first used to test the dosimeter to obtain a test count value; based on this value, the reader automatically determines if the weak or strong LED beam is necessary for readout. The signal on the dosimeter is proportional to the dose, and the reader estimates and reports the $H_p(0.07)$ dose for each dot dosimeter read in the microStar reader. The accuracy of the dose therefore depends on the stability of the LED beams.

To assess the functionality and reproducibility of the LED beams, a start-up protocol is used each time the microStar is powered on. Three measurements are made, with the first measurement done with the read dial on the “DRK” setting, which determines the dark current associated with equipment electronics and is obtained with the LED beam off and the shutter closed. The manufacturer-recommended limit for the DRK counts is less than thirty. The second measurement, made with the dial to the “CAL” setting, assesses the sensitivity and consistency of the photomultiplier tube (PMT). In it, the PMT counts are measured with the shutter open, and a reading from a small amount of ^{14}C radioactive material labeled CAL is made. The manufacturer suggests that this value be within $\pm 10\%$ of the standard operating average. The third measurement checks the consistency of the intensity of the LED beams and is labeled “LED” on the reader. In this research project, special attention was given to reproducibility of the LED measurements because the same beam intensities must be applied to the OSL material for each reading in order to have reproducible, reliable measurements; fluctuating LED beam intensities would lead to an incorrect measurement of the dose. The manufacturer-recommended tolerance limit for the LED measurement is $\pm 10\%$ of the standard operating average.

To establish standard operating values for the DRK, CAL and LED counts, twenty consecutive measurements were made and recorded. The mean values of those measurements were calculated and adopted as operating standards for the system. To ensure that the system was operating properly, the DRK, CAL, and LED counts were monitored for two working weeks (ten days) before the system was put into full use. On each day, five measurements were made at each dial position; the average was calculated and plotted against the established standards. These measurements were repeated and recorded each time the system was used.

8.2.3 Dosimeter Response

Two different types of nanoDot dosimeters were used in this research project: “standard” dosimeters with a manufacturer-specified sensitivity of 93% and “screened” dosimeters with 91% sensitivity. The manufacturer-specified accuracy of these dosimeters is $\pm 5\%$ and $\pm 2\%$, respectively. This difference in accuracy defines the “screened” type of dosimeters, which are selected due to their tighter accuracy and sold separately. Dosimeter precision was investigated to ensure that the dosimeters responded in the same way to an x-ray exposure. The precision was evaluated by the standard deviation of doses measured within each group, and results were analyzed within each group to ensure dosimeters of the same sensitivity had a uniform dose response. It was expected that the screened dots would have a smaller value of the standard deviation due to their higher manufacturer-specified accuracy. Since both dosimeter types are made of the same material, it was expected that standard and screened dots would measure the same dose. To ensure this was the case, the mean dose of each group was compared.

Ten dosimeters of each type were used to analyze dose response. For each measurement, one nanoDot dosimeter was placed in the center of the x-ray field on top of 5.1 cm of rectangular acrylic slabs. A 0.6 cc volume ionization chamber was also placed in the beam as a reference. A total of ten separate exposures was made under the same reference conditions for each dosimeter

type. The mean of each group was calculated, as well as the CV. The outcome of this test, and all others associated with the dosimetry system verification, are listed in Section 10.2.

8.2.4 Room-Light Erasure

During the length of this research project, each nanoDot dosimeter was used in multiple measurements. In most cases, a background reading of the dose was acquired first, followed by exposure to an x-ray beam, and then the actual post-exposure reading; the total dose was calculated as the difference of the post-exposure reading and the background reading. After usage, the OSL material was taken out of the light-tight casing and exposed to white room light to release the residual trapped energy in the dosimeter. The length of erasure time was determined to ensure acceptable background dose levels, as described below. Throughout this research project, a background limit of 1.0 mGy was established to decrease statistical uncertainty associated with measurements of the same order of magnitude as the background.

Prior to exposure, ten nanoDots were read to determine the background reading. The nanoDots were then exposed to a radiographic x-ray beam. Dosimeters were exposed one at a time, placed in the center of the x-ray field at a distance of 70 cm from the x-ray source. A 6 cc ion chamber was also placed in the x-ray beam to measure the air kerma for each exposure simultaneously. A post-exposure reading for each nanoDot was obtained, and the difference between the initial and post-exposure readings was calculated for all dosimeters. For the purpose of determining the necessary erasure time, this dose was considered to be the initial dose before white-light exposure, or $t=0$ reading.

Following this procedure, the dosimeters were exposed to room light for thirty minutes. After thirty minutes, one dosimeter was read. The displayed dose was recorded and compared to the initial dose reading. If it was greater than 1 mGy, the dosimeter was then returned to white light exposure to continue the erasing procedure. A second dosimeter was read ten minutes later

(total elapsed erasure time of forty minutes), and the process was repeated with all ten dosimeters until an acceptable background level of less than 1 mGy was reached.

8.2.5 Energy Response

The manufacturer provides a set of dosimeters that are calibrated at 80 kVp to beam code RQR6, defined by an effective energy of 44 keV and HVL of 2.9 mm Al and on PMMA material.^{53,54} This calibration set is used to calibrate the microStar OSL reader. CT beam energies used clinically are higher than 80 kVp, usually 120 kV and occasionally 100 kV, depending on the patient size and the anatomy to be imaged. Similarly, the HVLs found in typical CT systems are approximately 1-5 mm higher than the one used for calibration. Therefore, an energy correction procedure was performed to obtain factors to be applied to the dosimetric reading, to account for differences in x-ray beam characteristics.

To assess such energy response, dosimeters were placed in the center of an x-ray beam of a 320-slice CT scanner. The x-ray tube was held stationary during the exposure and positioned at the top of the gantry (12 o'clock). Five dosimeters and a 0.6 cc ionization chamber were placed on 5.1 cm of acrylic, as depicted in Figure 8-2. Because the calibration dosimeter set was originally exposed on acrylic, these reference conditions were matched as best as possible to assess energy response. The five dosimeters were positioned around the chamber to ensure that both the ion chamber and dosimeters would measure the same CT x-ray exposure. All other exposure parameters were kept constant, including filter and focal spot so that only the tube voltage was changed. The mean and CV were calculated for each tube voltage.

8.2.6 Scatter Response

The nanoDot calibration dosimeters were exposed on the surface of PMMA material, and the reader reports a shallow dose. While some organ doses measured in this research project were done with the dosimeters placed on the surface, some were also placed in the phantoms.

Because the conditions for non-superficial organs, dose measurements do not match those of the dosimeter calibration, scatter response was evaluated.

To do so, dosimeters were exposed under increasing thicknesses of acrylic, as diagrammed in Figure 8-3. A general x-ray tube was used in order to produce a flat x-ray field and avoid a non-uniform field due to the heel effect, and because there is not enough room in the CT scanner gantry to produce such a flat beam. The x-ray source was placed 100 cm from the surface of the acrylic. For the purpose of assessing the scatter response of the dosimeters, the three CT beams simulated using a general radiograph x-ray tube were the 80, 100 and 120 kV beams and the Small-S filter. The HVL of each of these three beams was measured (Section 7.2.3) and 1100 aluminum alloy was added to the x-ray beam until the HVL of the beam matched that of the CT beam.

To simulate different scatter conditions, five dosimeters were placed around a 0.6 cc ion chamber. The light field of the x-ray tube was used to position the dosimeters and ionization chamber at the center of the field. Surface dose measurements were made with this setup. For the rest of the measurements, 2.1 cm of acrylic were placed to the right and left of the ion chamber and the dosimeters to support the thicker acrylic slabs as well as to provide side scatter. More scattering material was placed superior and inferior to the chamber and dosimeters to simulate the situation of a dosimeter inside the phantom completely surrounded by scattering material. This setup is depicted in Figure 8-4.

The same methodology was followed, and scatter response was assessed in both the 320-slice scanner and the 64-slice scanner. However, instead of measurements at all beam energies, the tube voltage and bowtie filter combinations used within the clinical protocols used for organ dose measurements were used for evaluation of scatter response to the CT x-ray beams.

8.2.7 Dosimeter Calibration

The nanoDot dosimeters were calibrated for use in this research project. Due to the small size of the 0.6 cc ionization chamber, and the fact that its calibration is traceable to a national standards laboratory, it was the standard against which the nanoDot dosimeters were compared. First, the dosimeters were calibrated to each energy and filter combination by taking the ratio of the dosimeter dose to that of the ion chamber, as expressed in Equation 8-1,

$$C_{E,S} = \frac{\text{Raw dosimeter dose (mGy)}}{\text{Ion Chamber dose to air (mGy)}} \quad (8-1)$$

where $C_{E,S}$ is the energy and scatter correction factor. For organ doses that were measured on the surface of the phantom, specifically the pediatric doses (excluding the thyroid), lens of eye doses and skin doses, the surface $C_{E,S}$ correction factor was applied. For all other internal organs, the mean of the energy and scatter $C_{E,S}$ was applied to the raw organ dose measurements. The mean was chosen instead of separate depth-dependent correction factors because the uncertainty in which scatter correction factor to apply to each organ was large compared with the uncertainty that resulted in applying the mean.

For all ion chamber measurements involved in these calibration factors, the chamber measured dose to air. This value was converted to dose to tissue using the ratio of mass attenuation coefficients. These values are a function of effective energy, which is the energy of a polyenergetic x-ray beam that has the same attenuation characteristics of a polyenergetic beam. It was not possible to measure effective energy directly and therefore HVLs were measured on both the 320-slice and 64-slice scanner and converted to effective energies using a table provided by Bushberg⁶ and reproduced in Table 8-1. Mass attenuation coefficients (μ_{en}/ρ) for soft tissue (ICRU-44) and air were found at each effective energy calculated and the dose in air to tissue

was calculated for each of these effective energies as ratio of the two as described by Equation 8-2:

$$f = \frac{(\mu_{en} / \rho)_{tissue}}{(\mu_{en} / \rho)_{air}} \quad (8-2)$$

The organ doses reported, D , was finally obtained by dividing the uncorrected dosimeter dose reported by the reader, D_{raw} , by the $C_{E,S}$ correction factor, and then multiplying the result by the f -factor to calculate dose to tissue, as expressed in Equation 8-3.

$$D = \frac{D_{raw}}{C_{E,S}} \times f \quad (8-3)$$

8.2.8 Linearity Response

As with most dosimetry systems, it is important to ensure the dosimeters respond uniformly to different amounts of radiation. To assess linearity response, five dosimeters were positioned around a 0.6 cc ionization chamber and placed on 5.1 cm of acrylic, similar to the setup in 8.2.4 and 8.2.5. A tube voltage of 120 kV was used in the 320-slice CT scanner. The x-ray tube was positioned above the dosimeter and chamber setup at the top of the scanner gantry (12 o'clock position). Each exposure was one second in duration, and the tube current was changed from the minimum to maximum mA as allowed by the scanner operating in service mode (10 to 580 mA). Intermediate tube current values were also used to produce a linearity response curve for the OSL dosimeters.

These measurements were repeated to assess linearity over the range of doses measured throughout this research project. The same setup was used as previously described, however the second set of measurements were made with a fixed tube current of 500 mA. Multiple exposures were made to expose the dosimeters and ion chamber to a range of mA from 500 to 8000.

8.2.9 Angular Response

Because the geometry of a CT scan involves x-ray beam rotation, the angular response of the dot dosimeters was investigated, as the dosimeters receive exposure at all angles during a CT acquisition, with a variety of experimental setups. To investigate this angular response in a systematic manner, the CT scanner was operated in service mode, which allows the x-ray tube to be parked in a stationary position and at any angle. The zero-degree position was defined at the top, or 12-o'clock position, of the scanner gantry with the x-ray tube rotation in a clockwise direction through 360°. Angular response measurements were made both in-air and using a CTDI phantom, as described below.

8.2.9.1 In-air response

For each in-air measurement, a nanoDot dosimeter was suspended within the scanned region of the 320-slice CT scanner within the gantry at isocenter. Exposures were made from 0° to 180° at 15° intervals. Five measurements were made at each x-ray tube position. The mean and CV were calculated for each x-ray tube position.

8.2.9.2 In-phantom response

A standard CTDI phantom was used to assess the angular response of the dosimeters under scatter conditions. For each in-air measurement, one dosimeter was placed in the center hole at the Z-axis, midpoint in the phantom. PMMA rods were inserted into the center hole on each side of the dosimeter to fill voids and provide scatter. All other holes were also filled with PMMA rods. Figure 8-5 depicts the dosimeter setup in the phantom.

Exposures were made in the 320-slice scanner. The x-ray tube starting angular position was 270° (the 9 o'clock position within the scanner gantry) and repositioned clockwise to 90° with the dosimeters face-up in the phantom. The x-ray tube was moved at increments of 10° in order to include the 270° and 90° positions, i.e., when the primary x-ray beam is perpendicular to

the active area of the dosimeter. A second set of exposures was made with the dosimeters face-down, using the same tube positions and angular increments. The number of replicate measurements at each x-ray tube position was five.

8.2.10 Comparison of OSL Dosimeter in and out of its Light-Tight Case

In order to fit the nanoDot OSL dosimeters into the tomographic physical phantoms for certain organ dose measurements, the dosimeter material needed to be taken out of its light-tight case. The actual size of the active dosimeter is smaller than that of the case, making insertion into the phantom more feasible. To investigate this process and any effect it might have on accuracy and reproducibility of the dosimeters, identical CT exposures were made with two sets of dosimeters: one set in the case and one set out of the case. Comparison between the two was made to ensure there was no significant depletion of signal (dose) when the dosimeters were exposed outside of the light-tight plastic case. The nanoDot dosimeters were exposed using a preset clinical protocol (Baby Chest – Volume) using the 320-slice volumetric scanner. The CTDI head phantom was used for these exposures to simulate attenuation and scatter conditions. For each measurement, one dosimeter was placed at the longitudinal mid-point of the phantom. The protocol consists of two localizing tomographs in the AP and lateral orientations directly followed by a 0.4-second volumetric acquisition. This measurement process was repeated ten times with ten different dosimeters.

The dosimeters were placed at the 12 o'clock and center holes of the CTDI phantom. The 12 o'clock position was used to simulate organs at a shallow depth, such as the thyroid, while the center position was chosen as representative of deeper organs for example, the heart. Ten separate measurements were made with dosimeters exposed in the plastic case at each position; ten were taken out of the case and exposed individually at the same center and 12 o'clock phantom positions. The dimmest room lighting possible was used to minimize the dosimeter

background signal depletion while the active material was out of the case. After each measurement, the dosimeter was placed back into the light-tight case and read.



Figure 8-1. From top to bottom, nanoDot dosimeters with OSL material exposed, secondary side up and primary side up.

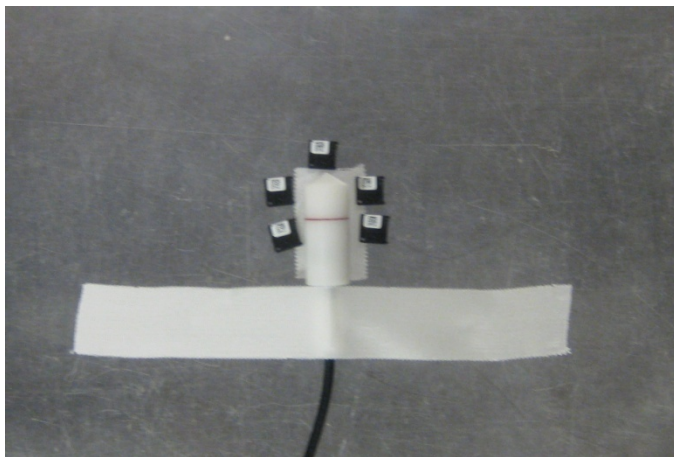


Figure 8-2. Energy response, dose rate response and scatter response surface setup; five nanoDot dosimeters placed around a 0.6 cc ionization chamber and on top of 5.1 cm of acrylic.

Table 8-1. HVL as a function of effective energy.⁶

HVL (mm Al)	Effective energy (keV)
1.25	24
1.54	26
1.9	28
2.27	30
3.34	35
4.52	40
5.76	45
6.97	50
9.24	60
11.15	70

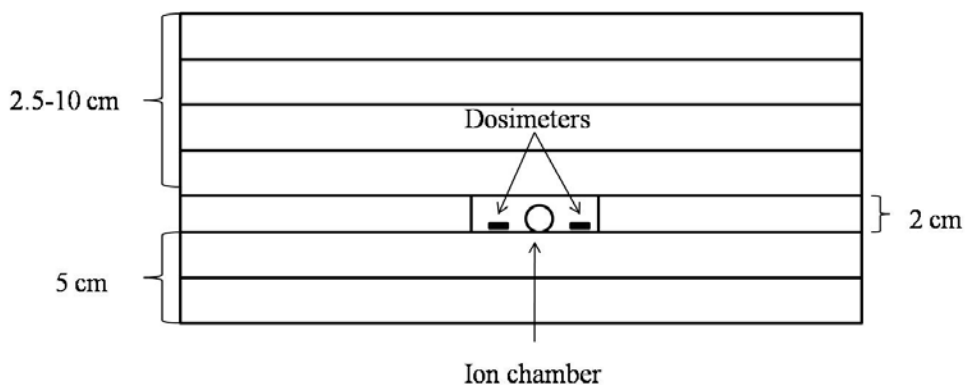


Figure 8-3. Diagram of cross-sectional view of ion chamber and dosimeters, placed on 5 cm of acrylic slabs. Acrylic slabs were added in 2.5 cm intervals on top of the ion chamber and dosimeters to evaluate the scatter response of the dosimeters.

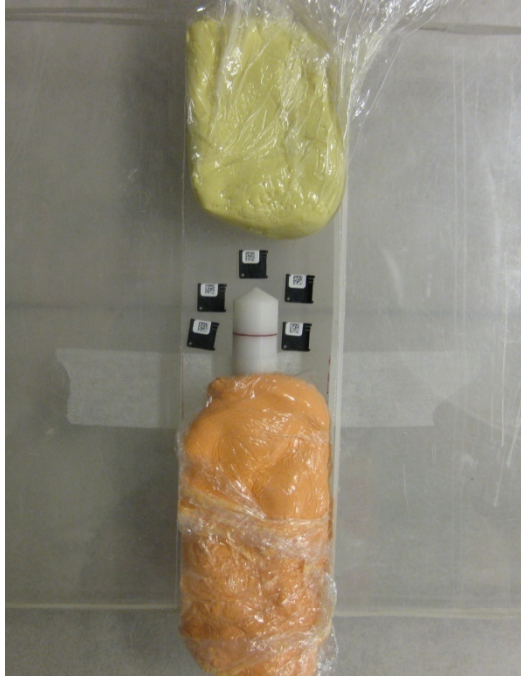


Figure 8-4. Setup of scatter response for measurements made with increasing thicknesses of acrylic, depicting the ionization chamber surrounded by nanoDot dosimeters. Scattering material was placed around both.

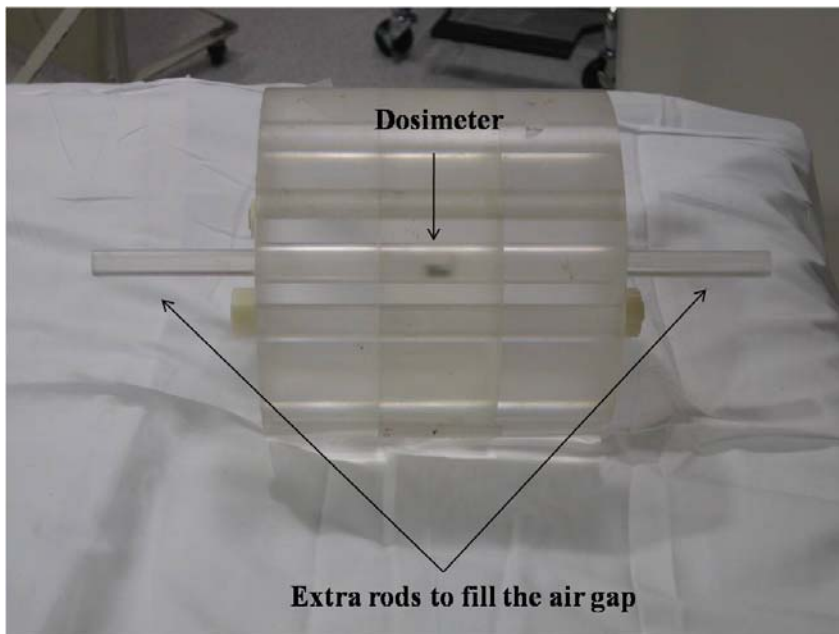


Figure 8-5. Setup of in-phantom angular response; nanoDot dosimeter placed at the mid-point of the CTDI head phantom.

CHAPTER 9 ORGAN DOSE MEASUREMENTS

This chapter details the procedure followed in performing organ dose measurements made using the tomographic physical phantoms described in Chapter 6. Three clinical protocols, developed and established by the RPC following the process detailed in Chapter 2, were used in conjunction with the nanoDot dosimeters to measure organ doses. The pediatric phantom was used for with the pediatric craniosynostosis protocol, and the adult phantom was used with brain perfusion and cardiac protocols. Localizing tomographs were used to set the boundaries of the scan, and the dosimeters were placed at predetermined locations on and in the phantoms after these tomographs were acquired. The scanner alignment lasers were used to ensure the positioning of the phantom was as close to that of the clinical study case as possible and also to ensure the phantom position on the scanner table was the same for each scan.

The nanoDot OSL dosimeters were used to measure mean organ doses. The small size of the nanoDots allows a single dosimeter to approximate a point organ dose. As much as possible, dosimeters were placed in numerous positions throughout an organ to cover as much of its volume as possible, and the point doses were averaged to obtain an average organ dose. As a more conservative figure, and to account for the fact that in CT, some organs are only partially exposed, the highest point dose reading was also recorded. Dosimeters were placed in organs of interest, as determined by their proximity to the primary CT x-ray beam as well as by their radiosensitivity (as inferred from their corresponding tissue weighting factors). Dosimeters in the phantom were put into place by cutting a small slit into the tissue-equivalent material of the desired slice. In the case of the adult phantom, a vacuum bag was used to stabilize the phantom and keep the different sections as compressed together as possible. A more complete description

of dosimeter locations and organ dose measurements is provided in the following sections for each protocol investigated.

9.1 Pediatric Head Study

A common CT study for pediatric patients is a non-contrast head scan to evaluate for craniosynostosis, a deformity of the skull caused by irregular fusing of cranial sutures.⁵⁵ In many cases of craniosynostosis, CT is used to evaluate the lengths of the patient's sutures. While this study has traditionally been performed on a 64-slice scanner, the ability to scan the entire head in a single rotation with the 320-slice scanner makes this study a good candidate for organ dose evaluation and comparison.

9.1.1 Volumetric Protocol

The increased coverage combined with the 0.35 ms rotation time make the 320-slice scanner conducive to pediatric studies, where patient motion during the acquisition is frequently a problem. The default parameters for the pediatric head CT study are listed in Table 9-1. The scan range was chosen, based on the localizing tomographs; a range of 120 mm ensured coverage of the entire brain for the phantom used. It is important to note that the range on the 320-slice scanner is adjustable in only 20 mm increments. Despite this limitation, the volumetric coverage selection depends on the size of the patient's skull and thus affects organ doses.

The 9-month-old phantom described in Section 6.4.2 was placed on the scanner table and positioned using the alignment lasers. The phantom position was also marked on the table to help with repositioning after dosimeter placement. Two perpendicular localizing tomographs were acquired, and after the scan boundaries were set, dosimeters were placed on and in the phantom. Organ doses resulting from the localizing tomographs were not measured. The selection of organs of interest was based on radiosensitive organs that are exposed directly to the

CT x-ray beam or in close proximity to be exposed to scattered radiation. The following organs were selected:

- a. Skin. Eight dosimeters were placed equidistant across the forehead to measure a representative average skin dose.
- b. Breast. Measurements were made on the surface of the pediatric phantom.
- c. Thyroid. A small hole was drilled into the phantom at the location of the thyroid and a dosimeter was taken out of its case to fit inside the orifice in the phantom.
- d. Lens of the eye. Two dosimeters were placed on the surface of each eye to measure dose to the lenses of the eyes.

Table 9-2 summarizes the number of dosimeters used for each of these organs of interest.

Because the thyroid measurement included only one dosimeter, the measurements with this protocol were repeated five times with five different sets of dosimeters to increase the statistical reliability of the measured thyroid dose. Figure 9-1 depicts the phantom setup on the CT scanner table.

To evaluate the potential for dose reduction, a second series of measurements was performed using the same phantom and protocol but decreasing the tube voltage from 120 kVp to 100 kVp. The same methodology for dosimeter placement and scanning sequence was followed. The results of this methodology, and all others described in this chapter, are presented in Chapter 10.

9.1.2 Helical Protocol

Dose measurements were performed on 64-slice CT scanner using a corresponding pediatric protocol, using a similar non-contrast head study specifically for the evaluation of craniosynostosis. Dosimeter placements and numbers were the same as those listed in Table 9-2 for the volumetric protocol. Similar scan parameters were chosen, including a range of 120 mm

to cover the entire head; these parameters are listed in Table 9-3. Positioning of the phantom within the scanner was done using the alignment lasers, and extensive efforts were made to position the phantom in the same way as on the volumetric scanner for best comparison.

9.1.3 Image Quality Analysis

In an effort to reduce organ doses resulting from the volumetric craniosynostosis protocol, an image quality evaluation was necessary to ensure that any reduction in tube voltage would provide images of diagnostic quality. To do so, an image quality phantom described in Section 6.5 was scanned on the 320-slice CT scanner used for organ dose measurements. The phantom was scanned using the same acquisition and reconstruction parameters as the volumetric craniosynostosis protocol. Images of the low-contrast module, acquired at 100 and 120 kV, were compared and scored by three experienced medical physicists. This scoring was performed by displaying the image in the center of module with the window and level settings optimized to display the number of objects seen in the image in the best way possible. Dim room lighting was used, and each viewer was seated 2-3 feet from the displayed image. The number of rods fully visible to each viewer was counted, and the total number of objects was reported for both images.

9.2 Adult Brain Perfusion

One of the most powerful tools of a 320-slice volumetric CT scanner is its ability to image an entire organ in a single rotation of the x-ray tube. As previously described in Section 3.2.3, one clinical application for this type of acquisition is the evaluation of suspected stroke patients using brain perfusion data. The RPC took on the task of designing this protocol in the clinical setting to maximize image quality and reduce dose, as described in Chapter 2. Organ dose measurements were made for each of the required iterations and then compared to the previous standard of perfusion imaging as preformed on a 64-slice scanner.

9.2.1 Volumetric Protocol

The volumetric adult brain perfusion protocol used for the evaluation of stroke consists of four general acquisitions. First among these is a non-contrast scan of the head to evaluate for potential bleeding. At Shands at UF, this is performed as a helical acquisition. This non-contrast scan is immediately followed by several dynamic volume scans to acquire perfusion data. The third and fourth acquisitions are a helical head scan with contrast, followed by a helical CT angiogram (CTA) of the head. These acquisitions are further detailed in Table 9-4.

Organ doses were measured for each part of this protocol. While the scanning parameters used in the non-contrast head, head with contrast and CTA of the head remained the same for all iterations, parameters for the dynamic volumes were varied to reflect the clinical changes the protocol underwent during development. The first volumetric acquisitions assessed were those suggested by the manufacturer and are labeled “Manufacturer at 80 kV” throughout this research project. During the optimization process, volumetric acquisitions were done with the tube voltage increased from 80 kV to 100 and 120 kV labeled “Manufacturer at 100 kV” and “Manufacturer at 120 kV,” respectively, and the organ doses were measured at identical locations. The fourth iteration of the dynamic volumes involved changing the timing of the arterial-phase acquisitions from intermittent to continuous, and is labeled “Continuous.” Finally, an altogether different acquisition protocol was evaluated. In this protocol, the tube current increased during a certain portion of the arterial phase. This protocol is labeled “mA Boost” in this research project.

A total of 27 nanoDot dosimeters was used to measure point organ doses for each of the resulting brain perfusion acquisitions. Similar to those of the pediatric study, organs were chosen based on radiosensitivity and proximity to the CT volume (Section 9.1.1). The following organs were chosen:

- a. Skin. 8 dosimeters were placed on the surface of the forehead to measure skin dose, as depicted in Figure 9-2.
- b. Lens of the eye. Two dosimeters were placed on the surface of each eye for the lens dose, also shown in Figure 9-2.
- c. Esophagus. There were three possible locations for dosimeter placed within the phantom for the esophagus. As was the case with all internal organs, the esophagus was outlined in the available phantom slices and was just hollow enough for the dosimeters to be placed in the hollow space. There were three slices with the denotation of the esophagus, and only one dosimeter would fit in each slice due to the small size of the esophagus. Thus, a total of three dosimeters was used, and their specific locations are pictured in Figure 9-3.
- d. Thyroid. The thyroid was contained in only one slice of the phantom, and three dosimeters were placed within the thyroid in left, center and right positions as shown in Figure 9-4.
- e. Brain. While the brain is fairly radioresistant, the average organ dose was measured, as it is within the primary beam during this protocol. Figure 9-5 shows five dosimeters placed in a slice mid-way through the brain. It was planned to have two additional dosimeters in the frontal portion of the brain; however, the bone-equivalent material directly below the slice prevented nanoDot dosimeters from being placed at this location.
- f. Breast. Finally, 2 dosimeters were placed between two slices of each breast, as illustrated in Figure 9-6. Breast tissue receives only scatter radiation with these acquisitions and therefore the nanoDots were placed with their primary side

perpendicular to the x-ray beam and flush against the two slices so that the active material of the dosimeters was in the same direction as the scattered radiation.

A summary of number and location of dosimeters is given in Table 9-5.

9.2.2 Helical Protocol

For comparison, the protocol used for evaluation of stroke utilized in the 64-slice scanner was also evaluated for organ dose measurements in the same locations and with the same adult phantom. Because of the smaller beam width (32 mm) compared to the volumetric scanner (160 mm), the entire brain is not covered during a single acquisition of the perfusion data. The full width of the beam is used, and images are acquired consecutively for 1 minute. As was the case with the volumetric scanner, a helical scan of the head without contrast was acquired before the perfusion acquisition. Helical CTA of the head and a second helical of the head with contrast are also acquired following the perfusion scan. The parameters for each of these acquisitions are detailed in Table 9-6.

9.2.3 Image Quality Evaluation

The advent of the 320-slice scanner and its volumetric acquisition capabilities led to a need to develop new imaging protocols to utilize the scanner in the most effective way possible. As previously explained, the scanner was equipped with standard protocols developed by the manufacturer, which were used as the starting point for the development process. An experienced neuroradiologist was in charge of assessing image quality by evaluating it throughout the development process of the brain perfusion protocol, as described in Chapter 2. Before additional changes were made to the protocol, the medical physicists in the RPC verified that any proposed change would not result in a significant dose increase. The CT technologists were given specific instructions from the neuroradiologist detailing which aspect(s) of the protocol to change prior to the study.

9.3 Adult Cardiac CT Angiography

A second powerful application of 160 mm volumetric CT scan coverage is cardiac imaging. Like the brain, the entire heart can be imaged with a single gantry rotation; in addition, cardiac CT angiography (CTA) is possible. Cardiac CTA is used for the detection of coronary artery disease (CAD).⁵⁶ While the American College of Cardiology (ACC) considers the 64-slice system as the current standard for cardiac CT studies, high doses have been seen as a limitation. However, cardiac CTA offers an alternative to the more invasive coronary angiography procedure for detection of CAD.

There are several advantages to the full cardiac coverage ability of the 320-slice system. Because images are acquired axially, the “stair-step” artifact commonly seen in helically-acquired images is eliminated.⁵⁷ As is the case in brain perfusion studies, the short rotation time allows the contrast bolus to be imaged at a single point in time producing temporally-uniform images,⁵⁷ actually placing the temporal resolution at one-half the rotation time.

There are three general acquisition protocols for cardiac CTA available on the 320-slice scanner:

- a. Cardiac functional analysis (CFA). If cardiac function needs to be assessed, the CT exposure begins with a half-rotation acquisition just before the R-R interval, continuing through the full R-R interval and ending with another half-rotation acquisition just after the R-R interval, as illustrated in Figure 9-7A. Image acquisition during the entire heartbeat allows reconstruction images at any point during the cardiac cycle. This protocol is used in the evaluation of the ejection fraction, stroke volume, cardiac output, end-systolic and end-diastolic volumes and segmental wall motion.⁵⁸
- b. CFA with dose modulation. In an effort to reduce dose to the patient, the CFA protocol may be performed with a dose modulation. While the image acquisition

process is the same, the mA is decreased during the diastole portion of the heart beat cycle, as depicted in Figure 9-7B.

- c. Prospective electrocardiogram (ECG) gating. When functional information is not necessary, prospective ECG gating is the preferred protocol. If the patient's heart rate is below 65 beats per minute (bpm), images are acquired using a single exposure with one-half rotation of the x-ray tube (0.35 s) at diastole, illustrated in Figure 9-7C. Because of the shorter exposure time, the dose is generally lower than in the previous protocol. If the patient's heart rate is above 65 bpm, several acquisitions occur during different heart beats. In the case of prospective ECG gating, less contrast is administered to the patient because of the decreased time needed for the entire study.⁵⁸

Details of the cardiac CTA protocols used to measure organ doses are listed in Table 9-7.

While there have been several studies comparing these various imaging protocols for cardiac CTA,^{58,57,59} all of them report effective doses measured from pencil chambers and CTDI phantoms. Similar to the methodology and selected criteria described in previous sections, nanoDot dosimeters were placed in or on radiosensitive organs within the primary x-ray beam and those in close proximity to the primary beam to receive a significant amount of scatter. As detailed in Table 9-8, five organs were selected to measure average organ doses:

- a. Thyroid. Three dosimeters were placed in the thyroid at the left, center and right positions of the organ (see Fig. 9-4).
- b. Lungs. A total of 20 dosimeters was used to measure an average dose to the lungs. Because of their large size, and the fact that only a portion of the lungs is exposed in the primary beam, doses were measured at five different sections of the phantom. For each slice, two dosimeters were placed in each lung. Two different orientations were

used: dosimeters were aligned in the coronal and sagittal directions. The dosimeter orientation was alternated with each phantom slice, as depicted in Figure 9-7.

- c. Stomach. The stomach has a relatively high tissue weighting factor, and, while it may not be in the primary beam, the stomach could receive a significant amount of scatter. A total of 8 dosimeters was used to measure the stomach dose as shown in Figure 9-8. Four dosimeters were positioned around the stomach in the two slices that contained the organ.
- d. Skin. Similar to the brain perfusion measurements, 8 dosimeters were placed on the surface of the phantom in two rows across the chest to measure skin dose and are pictured in Figure 9-9.
- e. Breast. Dose to the breast was of most concern for this protocol, as breast tissue was in the primary beam and is also highly radiosensitive. The male phantom was used and therefore lacked the anatomy of the female breast. However, dosimeters were placed to estimate female breast dose. Because a 1 cm layer of fatty tissue was assumed to line the breast; dosimeters were placed 1 cm beneath the surface⁶⁰ and also approximately 1 cm from the chest wall. Two dosimeters were placed at the right and left locations underneath the armpit to measure dose to the axillary tail of the breast. This area is where the most radiation-induced breast cancers are located.⁶¹ Breast tissue was located in two slices of the phantom, shown in Figure 9-10, and a total of 24 dosimeters were used to measure breast dose.

9.3.1 Volumetric Protocol

Three cardiac CTA protocols were used to measure organ doses on a 320-slice volumetric scanner: prospectively-gated, functional analysis and functional analysis with dose modulation. The details of these three protocols are listed in Table 9-10. For all protocols, the volumetric

scan is a single axial half-rotation. The scan begins based on the patient's heart rate, which was simulated for phantom measurements using an ECG simulator (Model EHS10, Dale Technology, Everett, WA).

9.3.2 Helical Protocol

For comparison, a cardiac CTA protocol was utilized on the 64-slice scanner. This protocol was chosen as the best comparison to the three volumetric protocols and is the most commonly-performed cardiac CTA protocol on this scanner. The parameters are detailed in Table 9-7. The scan consists of a single helical scan that covers the entire heart. As with the volumetric protocol, the scan begins at the appropriate time in the patient's heart cycle.

Table 9-1. Scan parameters for volumetric pediatric head protocol in Aquilion One 320-slice CT scanner.

Scan Parameter	
Nominal Tube voltage	120 kV
Tube Current	200 mA
Tube Rotation Time	0.6 sec
Effective mAs	121
Scan Range	120 mm
Acquisition Thickness	0.5 mm x 320
Focal Spot	Small
Filter	Small – S

Table 9-2. Locations and number of dosimeters used in and on pediatric phantom.

Organ	Number of dosimeters
Lens of Eye	4 (two on each eye)
Skin	8
Thyroid	1
Breast	6 (three on each breast)

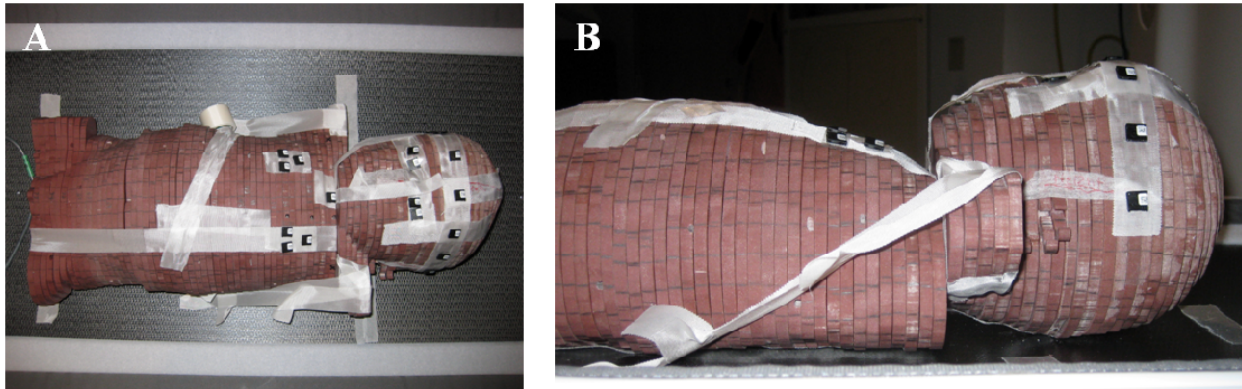


Figure 9-1. Pediatric phantom with surface dosimeters to measure skin, eye and breast doses; A) anterior view, and B) lateral view.

Table 9-3. Scan parameters for helical pediatric head protocol in Aquilion 64 64-slice CT scanner.

Scan Parameter	
Tube Voltage	120 kV
Tube Current	200 mA
Tube Rotation Time	0.5 sec
Effective mAs	157
Helical Pitch	0.641
Scan Range	120 mm
Acquisition Thickness	0.5 mm x 64
Focal Spot	Small
Filter	Small - S

Table 9-4. Details of volumetric brain perfusion protocols.

Scan name	Scan type	Tube voltage (kV)	Tube current (mA)	Rotation Time (s)	No. of volumes
Head without	Helical	120	300	0.5	-
CTA head	Helical	120	400	0.5	-
Head with	Helical	120	300	0.5	-
Original at 80 kV	Dynamic volume 1	80	310	0.75	5
	Dynamic volume 2	80	150	0.75	1
	Dynamic volume 3	80	150	0.75	13
Original at 100 kV	Dynamic volume 1	100	310	0.75	5
	Dynamic volume 2	100	150	0.75	1
	Dynamic volume 3	100	150	0.75	13
Original at 120 kV	Dynamic volume 1	120	310	0.75	1
	Dynamic volume 2	120	150	0.75	13
	Dynamic volume 3	120	150	0.75	5
Continuous	Dynamic volume 1	80	300	1.0	1
	Dynamic volume 2	80	120	1.0	17
	Dynamic volume 3	80	120	1.0	7
mA boost	Dynamic volume 1	80	310	0.75	1
	Dynamic volume 2	80	150	0.75	2
	Dynamic volume 3	80	300	0.75	7
	Dynamic volume 4	80	150	0.75	4
	Dynamic volume 5	80	150	0.75	6



Figure 9-2. Placement of skin and lens dosimeters on the forehead and lens of the eyes on the adult phantom for the brain perfusion protocol.

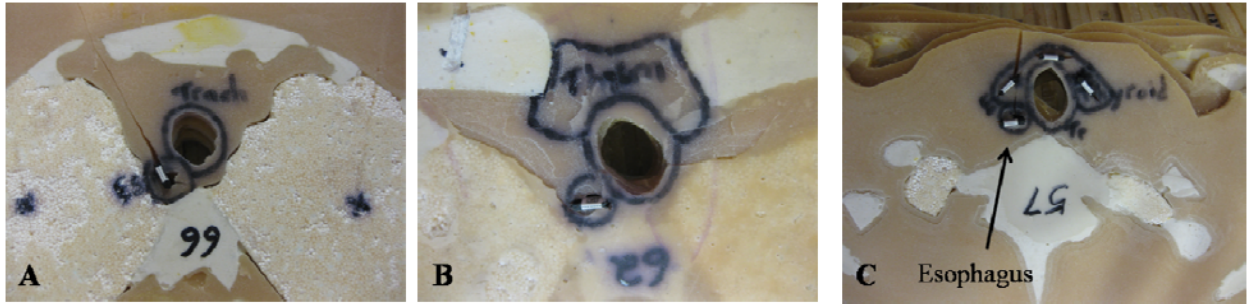


Figure 9-3. Dosimeter placement in the esophagus, measured in three slices (A-C) of the adult phantom from the brain perfusion protocol.

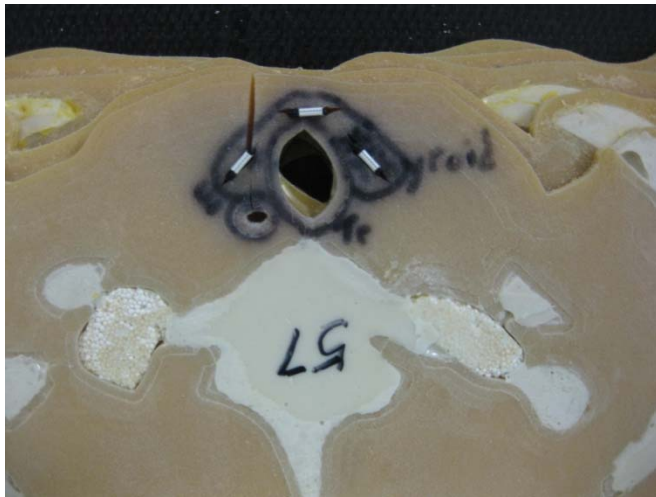


Figure 9-4. Locations of dosimeters within the thyroid.

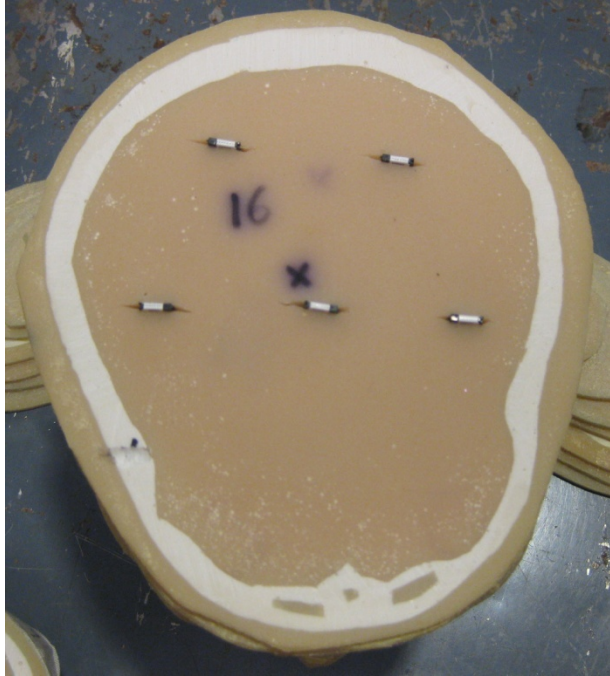


Figure 9-5. Locations of the dosimeters within the brain.

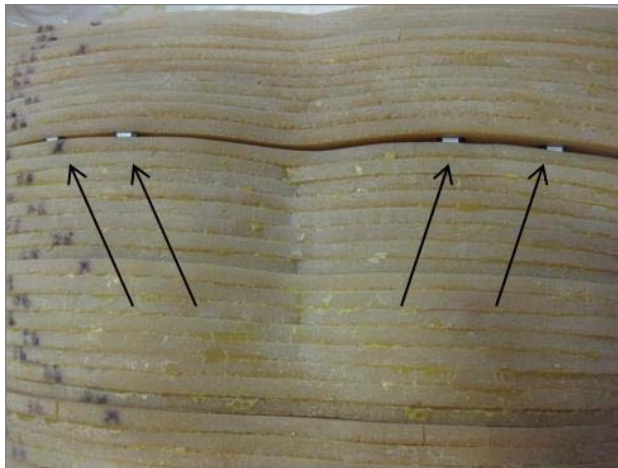


Figure 9-6. Locations of dosimeters within the breast to capture scattered radiation.

Table 9-5. Locations and number of dosimeters used in and on adult phantom for brain perfusion protocol.

Organ	Number of dosimeters
Esophagus	3
Thyroid	3
Brain	5
Skin	8
Breast	4 (two on each side)
Lens of Eye	4 (two on each eye)

Table 9-6. Scan parameters for helical adult brain perfusion protocol.

Scan name	Scan type	Tube voltage (kV)	Tube current (mA)	Rotation Time (s)	Helical Pitch	Detector Array
Head without Perfusion	Helical	120	300	0.75	0.641	0.5 x 64
CTA Head	Dynamic vol.	120	150	1.0	--	8.0 x 4
Head w/ delay	Helical	120	400	0.5	0.641	0.5 x 64

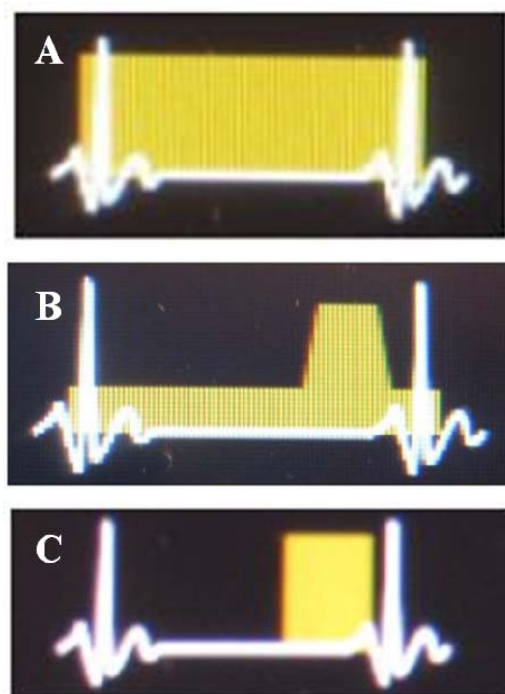


Figure 9-7. Cardiac R-R cycles are shown with exposure conditions of, A) functional analysis, B) functional analysis with dose modulation, and C) prospective ECG gating.

Table 9-7. Scan parameters for adult cardiac CTA protocol.

Protocol	Tube voltage (kV)	Tube current (mA)	Rotation time (s)	Slice thickness (mm)	Helical pitch
Prospectively-gated CTA	120	P400	0.35	0.5	--
Functional analysis with dose mod.	120	M500	0.35	0.5	--
Functional analysis	120	M500	0.35	0.5	--
64-slice	120	490	0.4	0.5 x 64	0.21

Table 9-8. Location and number of dosimeters used in and on adult phantom for cardiac CTA protocol.

Organ	Number of dosimeters
Thyroid	3
Lung	20
Stomach	8
Breast	24
Skin	8

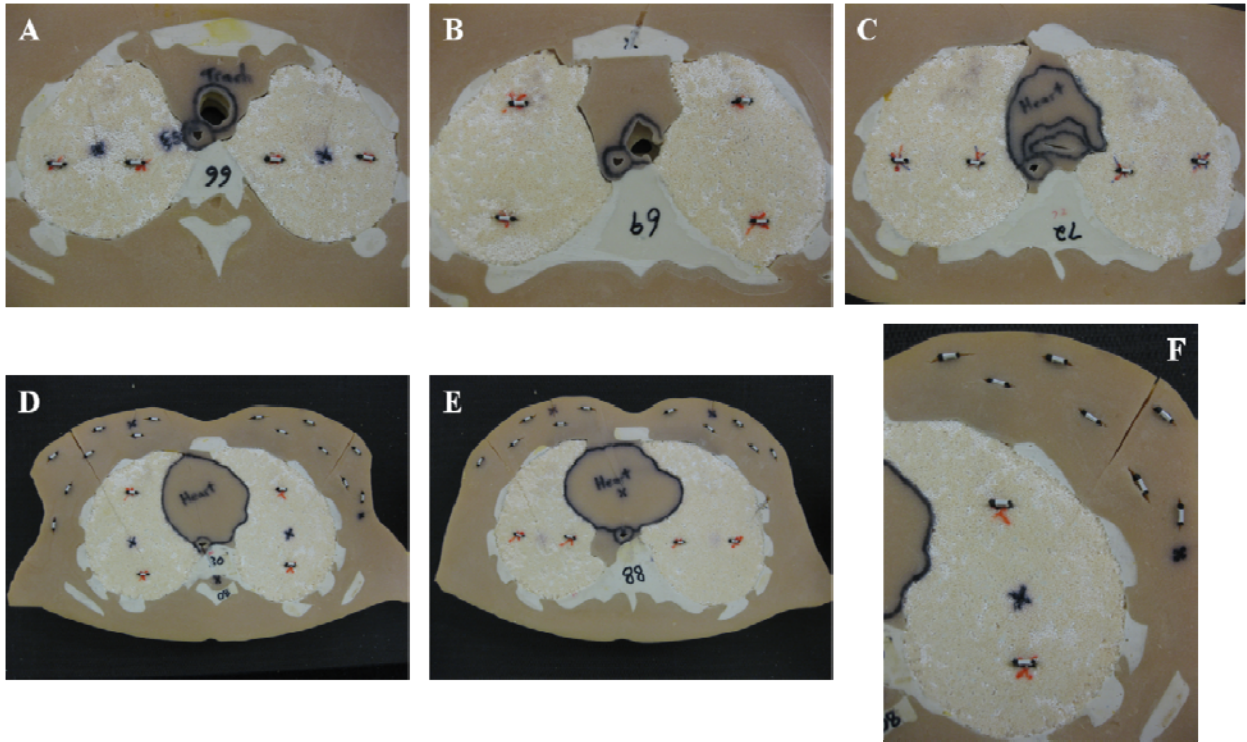


Figure 9-8. Placement of dosimeters in the lungs, A,C,E) with dosimeters aligned right to left in the lung, and B,D) with dosimeters aligned in the anterior-posterior direction, and F) as magnified view.

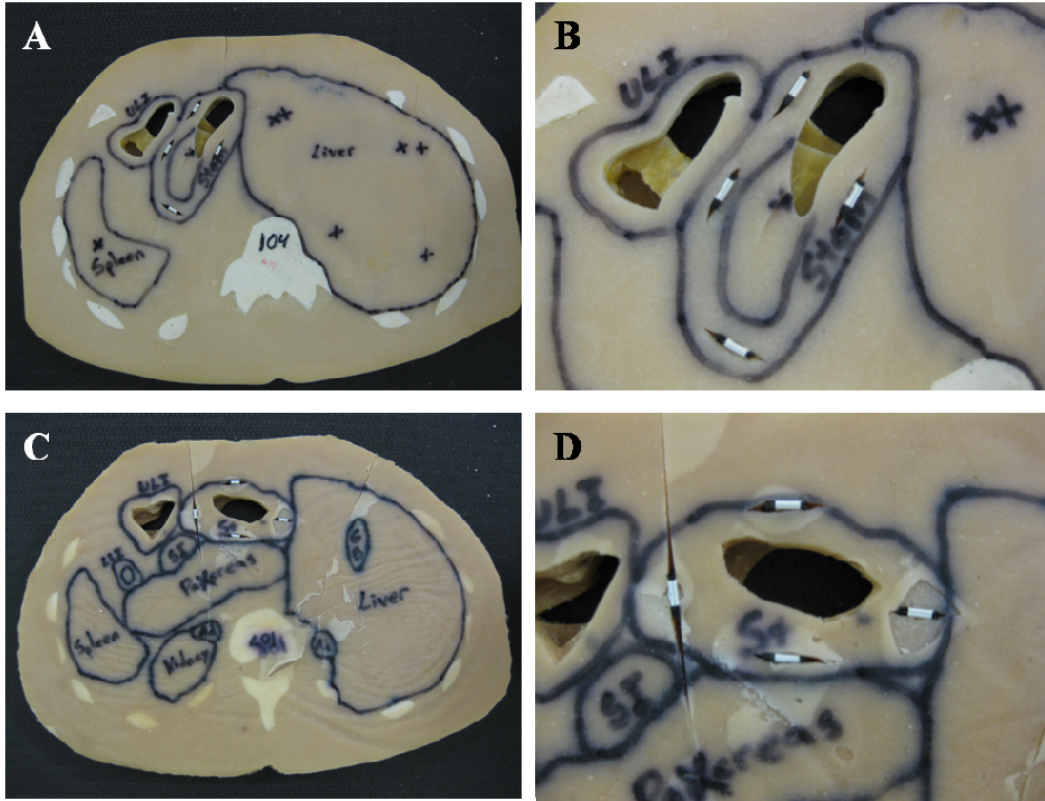


Figure 9-9. Placement of dosimeters within the stomach as the A) inferior slice, B) magnified view of the superior slice, C) inferior stomach slice and D) magnified view of the inferior slice.



Figure 9-10. Placement of the dosimeters to measure skin dose across the breasts.

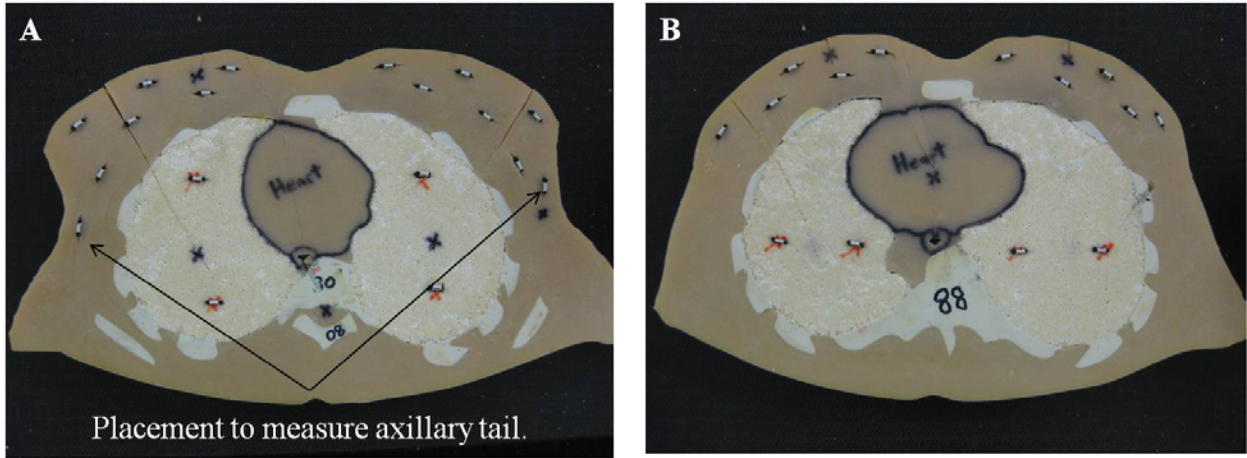


Figure 9-11. Locations of dosimeters for breast dose measurements using the cardiac CTA protocols with A) specific location of the two dosimeters measuring dose to the axillary tail of the breast and B) the inferior slice of the phantom.

CHAPTER 10 RESULTS

The measurements and results of this research project are presented in this chapter. The characterization of the wide-beam CT scanner was both interesting and informative. A novel method was developed to describe the bowtie filters used by the 320-slice CT system, information which is usually proprietary. A commercially-available dosimetry system was verified for use in diagnostic radiology, and a methodology is presented to allow the OSL dosimeters and reader to be used for organ dose measurements. Finally, using this OSL system and tomographic physical phantoms, organ doses were measured for three clinical protocols, redesigned by the RPC, using two CT systems: a 320-slice CT scanner and a 64-slice CT scanner for comparison. An image quality analysis was performed for each protocol thereby completing the aims of this research project.

10.1 Characterization of X-Ray Beams of Volumetric CT Scanner

10.1.1 Exposure Reproducibility

10.1.1.1 Service mode

Exposures performed in service mode, as detailed in 7.1.1, were reproducible to 0.03%. These measurements are provided in Table 10-1. The importance of this result is the reliability of the x-ray tube to reproduce its output. When multiple exposures were made to analyze the OSL dosimeters (section 8.2), it was important to minimize sources of error, including variability in the x-ray tube exposure. More specifically, this high degree of reproducibility guarantees very little source of error from the scanner in dosimeter measurements.

10.1.1.2 Clinical mode

Reproducibility was assessed for a volumetric and a helical protocol (7.1.2). For the volumetric protocol, the smallest CV was 1.2% at the center position, and the largest CV of

6.2%, was found at the 9 o'clock position. Full details are provided in Table 10-2. The difference among these sets of measurements are most likely due to the starting position of the x-ray tube for each volumetric acquisition, which is not controllable. When the speed of the rotation of the tube is reached, the acquisition then begins when the technologist manually starts the scan. The measured doses vary by position within the phantom because of this variability in starting tube position. It follows that the center position experiences the least amount of fluctuation in the dose measurements, as this position is independent of x-ray tube position; the measurement is made at isocenter, and the material surrounding the center position is uniform in the radial direction. Although minimal, this inherent fluctuation of dose due to the starting position of the x-ray tube is less than 6.2% and contributed to the uncertainty in organ dose measurements.

For the helical protocol, the measured doses were reproducible at all phantom positions, as shown in Table 10-3. The coefficients of variation were 0.1% or less. This high degree of reproducibility is most likely due to the helical rotation of the x-ray tube around the phantom and pencil chamber. While the starting position of the x-ray may be just as variable as seen in the volumetric protocol, the x-ray tube rotates around the phantom so many times during the full 160 mm scan that any variability in tube starting position is negated.

10.1.2 Beam Quality

10.1.2.1 Tube voltage

The differences in tube voltage measured in the 320-slice scanner (7.2.1) were less than 2.1% of the nominal value. Energies were also measured on the 64-slice scanner and were less than 2.4% of the nominal energy. In both cases, the largest inaccuracy of 2.4% occurred at 135 kV. For both scanners, the other three energies were accurate to less than 1.4%. These measurements are detailed in Table 10-4.

10.1.2.2 Total filtration

Measurement of the total filtration of the x-ray beam is described in 7.2.2. The effects of the Large-L filter at three beam energies are shown in Figure 10-1. The measured total filtration is graphed as a function of measurement position across the CT gantry, with isocenter defined as 0 mm. Despite this instrument having an energy range from 60 to 120 kV, as described in Section 6.2, this graph suggests that the instrument is not accurate at 80 kV. The shape of the curve at 80 kV should behave in a similar way as the 100 and 120 kV curves because these bowtie filters are not dependent on energy, only FOV.

Figure 10-2 displays the filtration differences between the Small-S and Large-L filters. In both cases, the increase in filtration measured from 0 cm to 15 cm approximates the shape of the bowtie filter. The decrease in total filtration past 15 cm may reflect the edge of the filter, as illustrated in Figure 10-3. The peak at 15 cm corresponds to what may be assumed to be the thickest part of the filter.

It is interesting that the Small-S filter has less total filtration at the center ($X=0$ cm) than the Large-L filter. One might assume a Small-S filter would have the highest total filtration to reduce radiation dose to the skin in pediatric studies, which would use the Small-S filter because of small FOVs. Similarly, one of the most important clinical applications of this scanner is brain perfusion studies. Brain images are acquired with a small field-of-view and use this Small-S filter. A thinner filter would allow for a reduction in tube current which would lower the overall dose to the patient, as compared to a thicker filter that would require a higher tube current to compensate for the increase in attenuation of a thicker filter, assuming all other parameters remain the same.

10.1.2.3 Half-value layer

Tables 10-5 and 10-6 display the HVLs measured at the nominal beam energies for the 320-slice and 64-scanners, respectively, in the center of the beam, as described in 7.2.3. As expected, for the same filter, the HVL increases with increasing energy as lower-energy photons are preferentially absorbed, producing a harder x-ray beam. For the 320-slice scanner, separate measurements were made using the Medium-M and Large-L filters; the calculated HVLs were the same for both filters; they are listed together in Table 10-5. Similarly, separate HVL measurements were made on the 64-slice scanner using the Small-S filter and Small-M, or medium filter, and these filters were found to be the same.

There is a 9% to 17% difference between the HVLs measured on the 320-slice scanner with the Small-S filter in place and either the Medium-M or Large-L. The x-ray beam is softer when using the Small-S filter, meaning the effective energy of the beam was shifted to lower energy in the spectrum and could affect organ doses.

There is also a significant difference between the HVL measurements between the 320-slice and 64-slice scanners. For all measurements, the HVLs of the 64-slice scanner are larger than those of the 320-slice scanner. These differences affect both skin doses and image quality. When compared, a lower HVL (for the same CT system) results in higher skin doses than a higher HVL because, as discussed in Section 7.2.1, attenuation coefficients are energy-dependent and more low-energy photons in the polyenergetic beam will be absorbed by the skin in a CT beam with a lower HVL. On the hand, a lower HVL allows for a reduction in tube current because of the increased transmission of photons.

10.1.3 Beam Width

The CR image of the beam width, acquired as described in 7.3 and displayed in Figure 10-4, was analyzed by Image J software. Calculating the FWHM of the beam profile in Figure 10-5,

the beam width was found to be 17.6 cm across the center of the radiographic image of the nominal 16 cm CT beam. This result is in agreement with a beam width of 18 cm measured by Geleijns *et al.*⁶² for the same type of scanner. One possible contributor to this discrepancy between the nominal and measured beam width is the need for all detector elements to be within the primary x-ray beam to ensure that the photon intensity is the same across all detectors thereby avoiding ring artifacts⁹ caused by inadequate signal at a single detector. In this case, the actual beam width is wider than the detector elements to avoid the penumbra of the x-ray beam falling on the detectors and known as overbeaming.⁶³ By increasing the width of the beam just slightly beyond the edge of the detector array, the penumbra falls outside the array and ring artifact is avoided.

10.1.4 Dose Profile

10.1.4.1 X-axis

As described in 7.4.1, a dose profile was measured in air in the direction perpendicular to the anode-cathode axis, which is the same direction as the fan beam. The normalized dose is displayed as a function of distance from isocenter ($X=0$ mm) in Figure 10-6. As expected, there is a decrease in dose as the distance from isocenter increases.

10.1.4.2 Z-axis

The beam profile in the direction of the Z-axis was also measured and detailed in 7.4.2. The dose measured by the dosimeter was normalized to the measurement at the center of the beam ($X=0$ mm) and plotted as a function of distance, as displayed in Figure 10-7. As expected, there is a small decrease in dose in the direction parallel to the anode-cathode axis due to the heel effect. This result could be due to the radiation field being so large in order to accommodate the 160 mm beam width that the heel effect is exaggerated on this 320-slice scanner. However, this profile is inconsistent with the beam profile produced using data acquired with the CR imaging

plate, as described in Section 10.1.3. The beam profile shown in Figure 10-5 does not exhibit the heel effect to the same degree as Figure 10-7. The profile produced using the dosimeters used raw dosimeter dose in air measurements. Because of the shape of the bowtie filters, and the fact that the dosimeters show a non-uniform energy response (see Section 10.2.4), the dosimeters used to measure the beam profile should be corrected. However, it was outside the scope of this research project to determine correction factors for this measurement. Instead, the beam profile in Figure 10-5, which does show a small decrease in beam intensity corresponding to the heel effect, is a more accurate assessment of the Z-axis profile.

10.2 Characterization of OSL Dosimetry System

10.2.1 Tracking of System Standards

As described in 8.2.1, standard operating values were established for the microStar OSL reader to ensure proper functioning of the LED beams used to read the dosimeters. The numerical means of these 50 measurements are 1.6 counts for the DRK, 2301.3 counts for CAL and 590.3 counts for the LED. These values, as well as the corresponding limits are listed in Table 10-7. After the standard values for the system were established, all three measurements were tracked over the course of two weeks to ensure system stability. Figures 10-8, 10-9 and 10-10 display the counts of the DRK, CAL and LED measurements, respectively, graphed at each day measurements were made and shown with the standard value. The DRK is displayed with the manufacturer-recommended upper limit; CAL and LED are displayed with the manufacturer recommended upper and lower limits. After the DRK, CAL and LED were tracked for two business weeks and all measurements remained within the established limits, it was decided that the system was functioning properly and ready for use.

10.2.2 Dosimeter Response

The results of the methodology outlined in 8.2.2 to assess the dose response of the dosimeters are shown in Table 10-8. Exposed under the same conditions, the means of the dose measured by the standard dosimeters (93% sensitivity) and screened dosimeters (91% sensitivity) was 47.36 mGy and 48.11 mGy, respectively. The coefficients of variation (CV) of the same measurements are 4.2% and 2.3%. These values are in agreement with the manufacturer-specified accuracies of 5% and 2% for the standard and screened dots. The OSL reader takes the sensitivity of each dosimeter into account during the calculation of dose, so it is expected that there is no significant difference between the means measured by the two sets of dosimeters.

Although there was no difference in the dose response of these two types of dosimeters, the manufacturer-specified accuracy, as well as the difference in the standard deviations of the measured dose response, were the differences between two dosimeter types, and this difference was taken into consideration when choosing which type to use for measurements. Because energy and scatter correction factors were applied to organ doses, the most accurate and precise measurements for energy and scatter corrections were desired. Thus, the screened dosimeters were used for both energy and scatter correction factors (10.2.4 and 10.2.5). In the case of the adult brain and cardiac protocols, both dosimeter types were used for organ dose measurements. The screened dots were used for the single exposure because of their tighter specifications, while the standard dosimeters were exposed five times.

10.2.3 Room-Light Erasure

After exposure, dosimeters were exposed to white light and periodically analyzed by the OSL reader, as described in 8.2.3. When all ten dots were read once (elapsed time 120 minutes), there was still a significant amount of dose trapped within the OSL material, approximately 73%

of the initial dose. Therefore, the process of reading the dosimeters at 10-minute intervals was repeated. After 320 minutes, almost 92% of the initial dose had been erased by the room light. After 1460 minutes (over night white-light exposure), 98% of the initial dose was depleted. A graph of these results is depicted in Figure 10-11. A 24-hour erasure period was sufficient to erase the dosimeters to an acceptable background level.

10.2.4 Energy Response

Energy response of the dosimeters was measured as outlined in 8.2.4. As expected, the dosimeters did not show a uniform response, when compared to the ionization chamber, at CT energies. Due to the small size of the 0.6 cc ionization chamber, it was the standard against which the nanoDot dosimeters were compared. Table 10-9 displays the mean of the five dosimeters used at each tube voltage, the dose measured by the ionization chamber and the ratio of the two.

While the dots are calibrated at 80 kV, the HVL used in calibration (2.9 mm Al) is much lower than the one measured for the CT beam (4.65 mm Al, Table 10-5) used for these measurements. Therefore, the dosimeters show a surprisingly good response at this energy. A caveat in this analysis is the fact that the energy response of the 0.6-cc chamber is not well-established at 80 kV, introducing a level of uncertainty in the doses measured at that tube voltage, a matter of future work, as described in the next chapter. However as the tube voltage increased, the response of the dosimeters decreased when compared to the ionization chamber. For 100, 120 and 135 kV, the difference between the mean dose measured by the dosimeters and the dose measured by the ionization chamber was 5, 11 and 17%, respectively. Because of these significant differences, an energy correction factor was applied to the dosimeters during organ dose measurements (further detailed in 10.2.5).

10.2.5 Scatter Response

The response of the dosimeters to scatter was first measured using the flat beam of a general x-ray tube, as outlined in Section 8.2.5. First, aluminum was added to the x-ray beam to simulate the HVL of the CT beam at three different tube voltages. The CT HVL, the simulated HVL and the percent difference between the two is given in Table 10-10. To compare the dosimeter response to the ionization chamber, the average of the five dosimeters measurements was divided by the ionization chamber dose. This quotient was calculated for measurements made at the surface and under increasing thicknesses of acrylic for each tube voltage. Specific values are given in Table 10-11. The largest difference between the dosimeters and the ionization chamber occurred for measurements made using the 80 kV beam and was 7%, which as explained in the previous section, is most likely due to the unknown energy response of the 0.6-cc ion chamber at 80 kV. This result is not expected, as the dosimeters were calibrated at this energy. A small contribution to this discrepancy could be reproducibility of the x-ray tube; however reproducibility was monitored throughout the measurement process because each exposure was made three times. Another contribution could be the positioning of the dosimeters and ionization chamber. The chamber was localized in position and an effort was made to keep it fixed in the same location because even though a flat radiation field was used for the exposure, small differences in position could result in small differences in the measurements. Similarly, the dosimeters were placed in the same locations around the chamber; however, differences in placement would increase the differences among measurements. Smaller differences were calculated for the 100 and 120 kV beam, 2% and 4%, both of which are more consistent with expected measurement error with sources of error being the manufacturer-specified accuracy of the dosimeters.

Because both energy and scatter corrections would need to be applied to the organ doses, scatter response was repeated. However this second set of measurements utilized the CT x-ray beams used to measure organ doses (Chapter 9). The results were similar to those measured using the flat x-ray field. The small size of the 0.6 cc ionization allowed the five surrounding dots to be close together, thereby minimizing the heel effect of the CT beam. Measurement details are listed in Table 10-12. The tube voltage and filter used on the 64-slice scanner was included with the measurements on the 320-slice scanner to obtain correction factors for all clinical protocols used to measure organ doses.

10.2.6 Dosimeter Calibration

Effective energies were calculated from measured HVLs of the beams used for clinical protocols, as described in Section 8.2.6 . Table 10-13 lists the effective energies, mass attenuation coefficients for tissue and air and calculated calibration factors for each HVL measured during this research project. Values of effective energy range from 37.2 keV to 53.1 keV which is consistent with those measured by Mori *et al.* for a 256-slice scanner.⁶⁴ The range of the f-factor calculated was from 1.05 to 1.07, consistent with the value of 1.06 published recently by the American Association of Medical Physicists (AAPM) report on the measurement of radiation dose in CT.¹¹

10.2.7 Linearity Response

As described in 8.2.6, the linearity response of the OSL dosimeters was analyzed by exposing the dosimeters to changing tube currents. The minimum tube current available in service mode was 10 mA and the maximum was 580 mA. The mean dose was plotted as a function of the tube current-time product and is displayed in Figure 10-12. The measurements were fitted to a linear line and the resulting correlation coefficient (R^2) was 0.9972, indicating that the dose was linear across the range of mAs values.

If the appropriate energy correction factor is applied to the dosimeters, comparison can be made between the mean dosimeter dose and the ion chamber dose. A correction factor of 0.86, corresponding to the 120 kV and the Medium-L filter, was applied to the mean dosimeter doses and plotted as a function of mA in Figure 10-13. The ion chamber dose is also plotted in the same figure as a function of mA. As evident by many overlapping measurements, the dosimeter linearity is comparable to that of the ion chamber.

In order to assess the linearity of the dosimeters in dose range used in this research project, a second set of measurements was made using a tube current range of 500 to 8000 mA. As shown in Figure 10-14, the dosimeters the linear response over the range of tube currents with an R^2 value of 0.9998. When the same energy correction of 0.86 is applied to the dosimeters, agreement is seen in Figure 10-15 between the response of the dosimeters with that of the ion chamber.

10.2.8 Angular Response

10.2.8.1 In-air response

The mean doses measured by the nanoDot dosimeters in air, as described in 8.2.7.1, are presented as a function of x-ray tube angle in Figure 10-16 with the corresponding 95% confidence interval (CI). The mean doses at the 0°-75° and 105°-180° positions were fairly constant: the range of mean doses measured at x-ray tube angles of 0° to 75° and 105° to 180° was 8.0 to 8.5 mGy and 7.9 to 8.4 mGy, respectively. The small variation in these doses suggests the dosimeters show very little dependence with angle of exposure when the dosimeters are used in-air. The minimum mean dose for the in-air measurements was 6.45 mGy measured at the 90° x-ray tube position with respect to the dosimeter. This result is expected, as it corresponds to the situation when the x-ray tube is perpendicular to the active area of the

dosimeter. The poor response measured at the 90°-position is of no concern for clinical purposes, as the dosimeters were not used in air for clinical organ dose estimates.

10.2.8.2 In-phantom response

Figure 10-17 depicts the dose response of the nanoDot dosimeters exposed in the head phantom at different x-ray tube positions. Measurements were made at 15° intervals to include the two positions (90° and 270°) when the CT x-ray beam is perpendicular to the active material of the OSL dosimeter. One might expect a dramatic decrease in dose at these two positions, but that was not observed; rather a one-way ANOVA suggests that the means of this data set are not significantly different ($p=0.680$), indicating that the dosimeters respond similarly to all angles of the x-ray tube.

10.2.9 Comparison of OSL Dosimeter In and Out of Its Light-Tight Case

Section 8.2.8 described the method in which dosimeters were exposed with the OSL material out of the light-tight plastic case. The mean of these measurements was 10.97 mGy at the 12 o'clock position and 8.54 mGy at the center position. For comparison, the same measurements were made with the dosimeters inside their cases. Means in the same phantom locations were 10.78 mGy and 8.28 mGy, respectively, as listed in Table 10-14. A one-way analysis of variance (ANOVA) suggests that the means of the measurements made with the dosimeters in and out of the plastic case at the 12 o'clock position are not significantly different ($p=0.657$). Similar results were found when comparing the means at the center position (ANOVA $p=0.116$). Therefore, the measured dose is not affected when the OSL material is removed from its plastic casing for organ dose measurements.

10.3 Organ Dose Measurements

For each of the three clinical protocols used for organ dose measurements, small dosimeters were used, and point doses were approximated by these dosimeters. For most organs,

multiple dosimeters were placed within the phantom at several locations within the organ. Large organs, such as the lungs, required a larger number of dosimeters to cover the full volume of the organ, compared to small organs, such as the thyroid. In the case of large organs, there is a possibility that the organ was only partially irradiated by the CT x-ray beam. For example, the lungs extend throughout most of the thoracic cavity. The 160 mm length of the cardiac CTA volumetric scans did not cover the entire lung volume. Instead, the volume of the lungs in the primary beam received both primary and scattered radiation, while the rest of the lung volume only received scatter. The averaging of all doses measured in the entire lung volume may not be representative of this non-uniform dose distribution when considering the risk of radiation-induced damage to lung tissue. To account for this uncertainty in the organ doses measured in this research project, two values were reported for all organ dose measurements: the mean and the maximum. The mean would most likely represent a realistic analysis of the risk associated with each CT study analyzed in this research project due to the limitations of dosimeter distribution in the phantom. In this case, the maximum would result in a conservative risk calculation that would also represent the “worst-case scenario.”

10.3.1 Pediatric Head Study

10.3.1.1 Organ doses

A comparison of the mean organ doses resulting from the pediatric craniosynostosis protocol measured with five sets of dosimeters and one set of dosimeters is given in Table 10-15. The mean, maximum and 95% confidence interval (CI) are listed in Table 10-16 for the set of five measurements. Energy correction factors were applied to surface measurements and were acquired as described in 8.2.5 and listed in Table 10-10. Skin, lens of eye and breast doses were corrected using the factor calculated on the surface of acrylic. The thyroid doses, which were measured in the phantom, were corrected using a scatter correction factor corresponding to 1” of

acrylic. These factors are listed in Table 10-10. The volumetric protocol used the Small-S filter for both 100 and 120 kV; the helical protocol used the Small-S filter and 120 kV.

As expected, all organ doses were higher using a tube voltage of 120 kV as compared to 100 kV. For all protocols, the dose to the lens of the eyes was slightly higher (approximately 16% higher) than the dose to the skin. Because these surface measurements were made in close proximity to each other on the phantom, the doses should be about the same. The small difference between dose to the skin and lens of the eye could be due to vertical height of the dosimeters; those close to the x-ray tube should receive a higher dose simply due to the closer proximity to the x-ray source.

The small values of the thyroid dose suggest that the dosimeter located in the thyroid was not in the primary x-ray beam, as expected. While an effort was taken to reduce statistical uncertainties by using five different sets of dosimeters and measuring organ doses five separate times, the 95% CI associated with the thyroid dose is greater than both the mean and maximum of the measurements performed on the 320-slice scanner at 120 kV. The fact that the measured doses are small adds to this statistical error. At the same tube voltage (120 kV), the thyroid dose measured on the 64-slice scanner is roughly 70% higher than the dose measured on the 320-slice scanner. Since the scan lengths were the same for both acquisitions, the difference in thyroid dose is most likely due to the difference acquisition techniques of the scanners: volumetric axial acquisition and helical acquisition. As described in Section 3.2.2, helical CT scans required an additional half-rotation of the x-ray tube at the beginning and end of the scan boundaries to information there is enough data for the necessary interpolation. This over-beaming effect is investigated by Winslow⁶⁵ and contributes to the measured in organ at the periphery of the scan boundaries. Furthermore, the numerous rotations of the x-ray tube during a helical scan produce

an increasing amount of scattered radiation to tissues and organs inside and outside of the primary beam. This increasing scatter effect is more obvious for organs outside of the primary beam, as the thyroid was for this protocol. Because of the wider beam coverage of the 320-slice scanner, only one rotation of the x-ray tube is required to cover the same area and less scatter is produced by this single rotation as compared to the multiple rotations of the tube during the helical scan.

For all protocols, the breast dose was less than 2 mGy. The means follow the same trend as the other organ measured: the dose measured at 100 kV was the smallest and of the two scanners, the 320-slice scanner resulted in a lower dose for the 120 kV set of measurements than the 64-slice scanner. Similar to the thyroid, the dosimeters that measured dose to the breast were not in the primary x-ray beam during the scan. However, because the breast dose was measured on the surface, the effect of the increased scatter due to the multiple rotations during the helical scan was not observed. Surface measurements are not as susceptible to scatter radiation within the phantom as in-phantom measurements because surface dosimeters receive only backscatter from the phantom while in-phantom dosimeters receive scatter from material surrounding the entire dosimeter. Therefore the breast doses were only slightly higher for the 64-slice scanner.

While the difference in the thyroid dose between the two CT scanners may be explained by an increase in the amount of scatter, the significant difference in surface dose measurements between the two different CT scanners was not expected. The lower HVLs measured using the 320-slice scanner might imply a higher skin dose because of the softer beam, as compared to the 64-slice scanner. This trend was not observed and may be due to a difference in the effective tube current for each scanner. The effective tube current (for this manufacturer) is equal to the produce of the tube current and rotation time for the 320-slice scanner and was equal to 121 for

this protocol. For helical scans, this value is divided by the pitch to account for over- or underscanning. In this case, a pitch of 0.641 was used on the 64-slice scanner, resulting in an effective mAs of 156. The higher effective mAs used for during acquisition on the 64-slice scanner contributed to the overall higher doses than the same acquired on the 320-slice scanner.

One parameter that would impact the measured organ doses that could vary by patient is the total scan length. For a volumetric acquisition, the scan range may be changed by the user from 100 mm to 160 mm in 20 mm increments. The scan length needed to cover the entire brain is determined clinically from the localizing tomograph. This process was used to measure organ doses, and a range of 120 mm was selected. However an increase in this range would most likely increase organ doses, especially to that of the thyroid, as the scan length extends down towards the neck bringing the primary radiation field closer to the organ. Similarly, a small patient might require a smaller range and receive a slightly smaller radiation dose. As described in 9.1, the same scan length was used for all phantom measurements for the best comparison.

One limitation of this pediatric phantom study was an inability to assess patient motion. A single volumetric acquisition acquired in 0.6 seconds will most likely result in significantly less patient motion than the helical comparison. While the actual x-ray tube rotation is of shorter duration (0.5 second), the smaller beam width of the 64-slice scanner requires several rotations of the x-ray tube about the patient to cover the entire scan range adequately. This longer total scan time allows more time for the patient to move during the scan. Limiting patient motion is of special concern in pediatric cases simply due to the nature of young babies. This phantom study did not allow for investigation into this issue; however, one can conclude the lower dose and decreased total scan time make this protocol a more viable option on the 320-slice scanner than the 64-slice scanner.

A second limitation of this pediatric phantom was the inability to measure organ doses other than the thyroid in the phantom. Unlike the adult phantom, the tissue-equivalent material of the pediatric phantom is solid. A hole needed to be drilled into the phantom for the measurement of the thyroid dose, and the same would have had to be done for other organ doses. Since a head protocol was chosen to assess pediatric doses, surface measurements to assess dose to the skin, lens of the eye and breast were appropriate as these are the organs of concern in a head protocol.

10.3.1.2 Image quality

To evaluate any possible dose reduction options as outlined in 9.1.3, three medical physicists scored images, shown in Figure 10-18, of the LCD section of the Catphan acquired using the same parameters as those of the volumetric craniosynostosis protocol (Table 9-1). The complied scores are listed in Table 10-17. Viewer 1 observed a difference in LCD between the images acquired at 100 and 120 kV, scoring a total of 20 objects for the 120 kV case and only 10 objects for the 100 kV case. Differences in scores of the combined supra-slice (A-C) and separately, of the combined sub-slice (D-F) objects also indicate that Viewer 1 observed a difference in LCD between the two images. Viewer 2 did not observe a difference between the two images because the total number of objects was scored equally. Similarly, the number of combined supra-slice and combined sub-slice objects was scored the same for the two images. Viewer 3 scored the two images similarly, with small differences between the total number of low-contrast objects detected in the two images, and small differences between the combined supra-slice and combined sub-slice objects.

Because no definite trend could be inferred from the LCD scores, further analysis was done. The mean of the combined supra-slice objects was calculated from the scores of the three viewers for the 120 kV and 100 kV images and found to be 10 and 9, respectively. Similarly, the

mean of the combined sub-slice scores was 7 and 5 for the 120 kV and 100 kV images, respectively.

To determine if these results are significant, a one-way analysis of variance (ANOVA) was used to compare the total scores of all three viewers of the 120 kV and 100 kV images. The difference between the means of the LCD scores was not found to be significant ($p=0.4830$). The same analysis was used to compare the means of the combined scores for the supra-slice and sub-slice groups; there was no significant difference between the 120 kV and 100 kV images for both combined groups ($p=0.6784$ and $p=0.3206$, respectively), either. While these results appear to indicate that there is not a significant degradation in image quality when lowering the tube voltage for this protocol, it is clear that future work in this area of the research project must include a larger sample of viewers in order to make more definite conclusions.

10.3.2 Adult Brain Perfusion

10.3.2.1 Organ doses

Table 10-18 lists two sets of data for each protocol and organ resulting from the brain perfusion protocol were measured as described in 9.2. One set of standard nanoDot dosimeters was placed on and in the phantom, and the scan was repeated five times with the same set of dosimeters. The mean of these five scans was calculated. This method was chosen to reduce statistical error in measuring the organ doses once, as well as to minimize error due to reproducibility of the x-ray tube. As seen in 10.1.2, up to a 6.2% standard deviation was measured using the clinical mode of the scanner, and therefore measured organ doses are subject to this variability. Since only one set of dosimeters is used, any defect in a single dot is exaggerated by scanning five times. To verify these organ doses, screened nanoDot dosimeters were used for the same measurement but scanned only once. As evident by the small differences in the means using these two methods, organ doses are very comparable. The mean organ doses,

as well as the maximum and 95% CI of the measurements are given in Table 10-19. As with the pediatric phantom measurements, surface measurements, were corrected for energy and organ doses measured in the phantom were corrected for energy and scatter.

Of the three original manufacturer protocols, the acquisitions performed at 120 kV resulted in the highest mean organ doses, as expected. For all three protocols, the mean dose to the eyes was the largest dose measured and 10-14% higher than the skin dose measurements. This trend was also observed for the same measurements performed with the pediatric protocol, and as described in 10.3.1.1 could be due to the vertical position of the dosimeters at each organ location and the heel effect. The breast dose was the lowest of all organs measured, as expected because the breast was set outside of the boundaries of the scan.

The doses measured in the esophagus provide a good example of reporting the mean and maximum doses. This organ was outlined in three different slices of the phantom. Because the esophagus is not in the direct radiation field, the amount of scattered received by the dosimeters increases as the slices get closer to the head. A non-uniform dose distribution was measured in this organ as a result of different amounts of scattered radiation reaching different parts of the organ.

The mA boost and continuous protocols resulted in approximately the same mean doses for all organs. Although the acquisitions differ between these two protocols, the total tube current-time product is approximately the same for both protocols. This total mAs is calculated by multiplying the tube current, rotation time and the number of volumes acquired. The mA boost protocol uses a scan time of 0.75 s, where the continuous protocol volumes are acquired with a 1.0 s rotation. However the tube current is higher for the mA boost protocol compared to the continuous protocol, so the mAs is comparable.

Despite the total scan volume being smaller, the mean skin dose resulting from the 64-slice scanner was higher than all other mean doses. The smaller volume spares dose to the eyes, but the mean skin dose is approximately 4.5 times higher in the 64-slice scanner when compared to the mean skin doses resulting from the volumetric protocols. The mean skin dose resulting from this protocol was the highest measured during this research project. Skin erythema effects can occur for doses above 2 Gy.⁶⁶ While this limit is not approached for a single brain perfusion study in the 64-slice scanner, it could be approached if the scan needed to be repeated. With the development of the brain perfusion protocol in the 320-slice scanner (discussed in 10.3.2.2) complete, the mA boost and continuous protocols are recommended in place of the 64-slice scanner whenever possible.

Comparison of the mean doses of the dosimeters scanned five times to those scanned once shows one of the largest differences for the skin measurements on the 64-slice scanner. For the skin measurements, dosimeters were placed on the surface of the phantom, as shown in Figure 9-2. Along with the axially-acquired volumetric scan, the helical protocol also consists of three helical scans, detailed in Table 9-7. While the nominal beam width used was 32 mm and able to cover the active volume of the OSL dosimeters, the helical nature of the scan could result in the beam not directly passing over one or more of the surface dosimeters. If the x-ray tube is at the bottom of the gantry these dosimeters measure the radiation transmitted through the entire head. Because the CT scanner table moves during helical acquisitions, the dosimeter may not be exposed fully to the primary beam. This pattern may result in an inaccurate dose measurement if the primary beam was not measured by the dosimeters. However, this pattern would be representative of the dose distribution experienced by a single patient undergoing the same scan and therefore a reasonable measurement. To report an average dose for this particular scan, the

more representative measurement is that of the dosimeters scanned five times; there is a better chance of full exposing the dosimeters during the scan resulting in an average skin dose measurement.

10.3.2.2 Image quality

As detailed in 9.2.4, the brain perfusion protocol underwent several changes during the development process in an effort to produce high-quality images with the lowest reasonable dose. The initial brain perfusion protocol (Manufacturer at 80 kV, Table 10-5) resulted in an image set that was of inferior image quality compared to the current perfusion studies performed on 64-slice scanner. The timing of the dynamic volumes generated image sets that was lacking diagnostic information during the arterial phase of contrast-agent uptake. In order to ensure that a complete set of diagnostic images were acquired, the first amendment to the brain perfusion exam was the addition of a helically-acquired CT angiogram (CTA) of the head. Once the timing issue with the dynamic volumes had been resolved, the diagnostic quality of the dynamic volume image sets were still considered poor; the neuroradiologist proposed an increase of the tube voltage used to acquire those volumes from 80 kV to 120 kV. While this is a reasonable approach, the medical physicists suggested an increase to 100 kV, as dose to the patient increases with increasing tube voltage. The second and third iterations of the protocol involved modifying the tube voltage to 100 kV and 120 kV, respectively.

As expected, the image sets acquired at 120 kV were deemed of higher image quality by the neuroradiologist compared to the same acquired at 80 and 100 kV. However, due to the considerable dose savings, especially to the skin and eyes, and the fact that the images acquired at 100 kV were deemed by the neuroradiologist to be of diagnostic quality, the RPC accepted the 100 kV modifications to the protocol.

A second protocol, originally designed for evaluation of arterio-venous malformations (AVM), was proposed by the neuroradiologist. This protocol (Continuous, Table 10-5) uses a continuous acquisition of 19 volumes with a one-second tube rotation and therefore the beam is on continuously for 19 seconds. The neuroradiologist presented this to the RPC, and, after preliminary dose measurements, the protocol was used clinically. The success of this protocol for AVM evaluation led the neuroradiologist to propose the same protocol for brain perfusion. Thus far, this protocol has been a success and offers the lowest organ doses to the patient.

Finally, a fifth iteration of the brain perfusion protocol was developed by the manufacturer in response to the image quality issues reported by the neuroradiologist and the RPC. Instead of increasing the tube voltage of the original protocol (Manufacturer at 80kV, Table 10-5), the manufacturer's proposed protocol increased the tube current from 100 mA to 310 mA during the initial arterial phase. While the increase in tube current will increase the organ doses compared to those of the original protocol, the increase in dose due to increase mA was less than using a higher tube voltage to achieve images of diagnostic quality, as determined by the neuroradiologist.

At the time of the conclusion of this research project, the Continuous protocol was being used clinically more frequently than any of the other RPC-approved protocols. Considering that this protocol resulted in the lowest measured organ doses, a balance of image quality and dose was achieved. The protocol development process involved several iterations of the protocol, as well as the involvement of several members of the RPC and radiology department and resulted in successfully providing high-quality care to patients.

10.3.4 Adult Cardiac CTA

10.3.4.1 Organ doses

The mean organ doses resulting from the volumetric and helical protocols are listed in Tables 10-20, detailing the doses measured from five exposures and single exposure. Table 10-21 lists the mean doses averaged over the five exposures, including the maximum and 95% CI associated with the doses. As with all other measurements, organ doses were corrected with energy and scatter corrections appropriate, as expressed in Equation 8-3, to the tube voltage and filter combination used for each protocol, as listed in Table 10-12. As described in 10.3.2.1, two sets of dosimeters were used to measure organ doses: one set of standard dosimeters was scanned five times and averaged, and screened dots were scanned one time.

For all protocols, the breast and skin doses were the highest among the organ doses measured. Skin doses were measured on the surface across the breast in two longitudinal locations illustrated in Figure 9-9. Breast dose was measured in the phantom, as depicted in Figure 9-10. These results were expected, as both organs are within the radiation field centered at the heart for cardiac imaging. The mean and maximum lung doses were less than those of the skin and breast doses. The result may be explained by the differences in scatter characteristics of the lung tissue and breast tissues. The lung-tissue equivalent material is similar to an air cavity which provides less scatter than soft-tissue equivalent material. The decrease in the amount of scatter in the lungs compared to the breast resulted in smaller measured doses in the lungs. The same rationale may be applied to the dose differences between skin and lung measurements. The skin measurements were made on the surface of the phantom; the dosimeters absorb the primary beam radiation on the surface as well as backscatter. While the dosimeters in the lung are completely surrounding by lung tissue-equivalent material, minimal scatter is produced and the dose absorbed is less than that on the surface of the skin.

Of the three protocols evaluated on the 320-slice scanner, the prospectively-gated protocol resulted in the lowest mean organ doses. Whenever possible, and clinically indicated, this is the protocol that should be used. The clinical limitation of this protocol is the requirement of a low heart rate. The manufacturer-specifies a maximum heart rate of 60 bpm; if the heart rate is too high, the 175 ms scan time is too long to be completed while the heart is in diastole. Therefore, patients with heart rates higher than 60 bpm need to be given medication to slow the heart during the scan or receive higher doses because more than one acquisition is required by the system.

When complete functional analysis of the heart is clinically necessary, the prospectively-gated protocol is not an option. Of the two functional analysis protocols, the protocol that includes dose modulation resulted in lower organ doses, as expected. On average, there was a 40% dose reduction in all mean organ doses using the dose modulation feature for the functional analysis protocol and is the preferred protocol for functional analysis.

In general, the 64-slice protocol resulted in higher doses than all of the volumetric protocols. Of particular interest are the mean skin doses measured using a single scan with a mean of 25.37 mGy and those averaged over five scans with a mean of 76.14 mGy. There was not another set of measurements with a difference this large between the two sets of dosimeters. One contributor to this large difference is the helical nature of the scan. Although measures were taken to reproduce the position of the phantom and the dosimeters within the CT scanner, there was no guarantee that the x-ray tube exposure would begin at the same location with respect to the phantom. Additionally, the helical scan means the table translates through the gantry while the exposure is taking place. The spiral dose profile that results could explain the difference in the skin dose measurements, as also described for the skin doses measured for the brain perfusion protocol on the 64-slice scanner (section 10.3.2.1). On the surface, the x-ray beam

may not have directly exposed the dosimeters, or some of the dosimeters, causing a non-uniform dose deposition. It is more likely that this was the case of the single exposure; performing the scan 5 times and taking the average should cause the x-ray tube to travel in a different path with each scan due to the differences in start positions of the tube. The fact that this difference in mean doses is seen only on these skin dose measurements lends credibility to this argument, despite having no means available for confirmation; skin dose measurements on the surface of the phantom were subject to both the primary x-ray beam as well as scattered radiation. Organ doses measured in the phantom result from the attenuated x-ray beam (as it passes through the phantom) and scattered radiation.

Similarly, the mean dose to the stomach is significantly larger with the 64-slice protocol than all volumetric protocols. The obvious contributor to the larger dose could be that the organ was included in the helical and not in the volumetric scan. However, the scan range was 160 mm for all cardiac scans, and the beginning of the scan was also set to the same slice on the phantom, based on the alignment lasers and localizing tomographs. One possible reason for this discrepancy between mean stomach doses is the added half-rotation necessary for helical CT scanning. Despite data being acquired helically, images are reconstructed in the axial plane. There is a half rotation of the x-ray tube at the beginning and end of each helical scan that exposes the patient without data being used for reconstruction purposes. If this half rotation at the end of the scan contained the stomach, a higher dose would be measured than if only scattered radiation contributed to the mean dose. These added half rotations are not necessary in the axial acquisition of the volumetric protocols, hence the stomach dose is lower in the volumetric protocols. A second contribution involved the increased amount of scatter generated by helical scans. As previously described (section 10.3.3.1), the small beam width results in an

increased number of helical scans to cover the same total scan length as the volumetric protocol. As the number of x-ray tube rotations increase, the amount of scatter produced within the phantom also increases and resulted in higher stomach doses measured on the 64-slice scanner compared to those on the 320-slice scanner.

10.3.4.2 Image quality

To evaluate image quality of these cardiac CTA protocols, the Catphan image quality phantom was used, as described in 9.4.2. The first protocol analyzed was the prospectively-gated protocol. The images are reconstructed at 0.5 mm slices, and Catphan images of the low-contrast module were also acquired at that slice thickness; the image in the center of the module is displayed in Figure 10-19. During scoring of the image, window width and level were used to adjust the image for best visualization of the low-contrast objects. Despite this manipulating, none of the objects were visible in the image. The same situation occurred with the image set reconstructed at 1.0 mm slices. Not being able to score this low-contrast module with these reconstruction parameters is a limitation of the Catphan and its ability to assess image quality for new volumetric scanners. Thicker slices are needed to combine information from neighboring thin slices for proper viewing of objects in the phantom. Growing technology has allowed for much thinner slices to be reconstructed than older generation scanners. Clinical indications for this protocol involve the imaging of small vessels which is achieved with images reconstructed with thin slices.

Despite the limitations of the Catphan for this analysis, the parameter of most concern in these cardiac protocols is the temporal resolution of the acquisition. Because cardiac motion cannot be stopped, it is important to acquire images at the correct point in the cardiac cycle and to do so while the heart is in as motionless of a state as possible. Where this short acquisition time is the parameter that dictates these cardiac protocols, such that time cannot be changed

without negatively affecting temporal resolution, other parameters may be changed, but doing so will most likely not affect image quality and dose in a positive way. The effective tube current used for prospectively-gated and functional analysis protocols was 140 and 175, respectively. While these values may appear low, they are the result of the short acquisition time. The actual tube current is 400 and 500, respectively; the maximum tube current available on the scanner is 580, so the values used for these protocols are approaching the maximum tube current. The tube voltage could be increased to 135 kV, but this increase would result in an increase in organ doses. Since the image quality at 120 kV is sufficient, as evidenced by the number of clinical cardiac CTA studies that have been performed without image quality complaints by the radiologists to the RPC, there is no clinical need to increase the tube voltage and consequently organ doses. Furthermore, cardiac images are acquired with the use of a contrast agent to image vessels. The clinical use of a contrast agent may be better assessed using the high-contrast resolution module of the Catphan. However, the technology of modern CT scanners has placed the limiting resolution of the images in the detector resolution, i.e., the size of the detectors used to acquire the images defines the limiting resolution, thereby limiting the Catphan in its ability to measure the resolution of a CT system.

10.3.5 Comparisons to Monte Carlo Organ Dose Simulations

Work was done by Ghita⁶⁷ to estimate organ doses using Monte Carlo simulations for the same three clinical protocols investigated in this research project. These simulations were done for the 320-slice scanner and include most of the organs chosen for dose measurements using the OSL dosimeters.

Comparisons of the measured and simulated doses for the pediatric craniosynostosis protocol are shown in Table 10-20. The relative differences listed compare the MC-simulated doses to the mean dose of the OSL dosimeter measurements for the organs selected. The

smallest relative difference (1.72%) among the doses measured is for the lenses of the eyes for the 100 kV case and is due to the fact that the lens of the eye is a small organ completely positioned with the primary CT beam during the scan. Two dosimeters were used for these measurements, and therefore the dose was well-sampled; in addition, the small size of the organ makes the numerical measured average a more realistic representation of the dose throughout the organ. The largest relative difference is 11.38% for the thyroid doses at 120 kV; this organ is at the edge of the actual scan boundaries and most likely it is only exposed to scattered radiation from the scan. However, one limitation of the dosimeter measurements is highlighted by the results shown for this organ. The fact that the thyroid is assessable only in one slice of the phantom limits the ability to achieve a uniform dosimeter placement throughout the organ; measurements therefore correspond only to that slice of the phantom, whereas the Monte Carlo simulations used data for the entire volume of the organ. The relative differences among the measured and simulated skin doses are -4.93% and -8.32%, at 120 and 100 kV, respectively. In fact, the simulated doses fall in between the mean and the maximum measured doses, further justifying the reporting of both the maximum and mean measured doses as described in Chapter 9.

The comparisons between measured and simulated organ doses for the adult brain perfusion protocols are given in Table 10-21. For the five protocols, doses to the lenses of the eyes are most comparable among all other organs investigated. The relative differences range from 2.01% to 7.15%, due to the adequate sampling because of the small size of the organ and its location in the primary beam during the scan. Of the other four organs, the relative differences among the skin doses are comparable, and range from 12.04% to 33.07%. Similar differences are seen among the thyroid doses, with a range of 13.20% to 21.96%. The thyroid is a small

organ at the edge of the primary beam and, while the relative differences are apparently large, this difference is rather misleading as the doses are small thereby inflating the relative difference. For example, a measured difference of only 1.3 mGy between the simulated and measured thyroid doses for the mA boost protocol, which corresponds to a 20% relative difference. The same was found with the comparison among measured and simulated esophagus doses; the differences in doses range from approximately 1 to 3 mGy, whereas the relative differences range from 41 to 58%. The largest discrepancy between measured and simulated doses for the brain perfusion protocols corresponds to the brain doses, ranging from -21.8 to 26.6%. This discrepancy is attributed to dosimeter placement being non-uniform throughout the organ because of limitations in access to it from all slices in the phantom, as described in Section 9.2.1.

Finally, comparisons were made among measured and simulated doses for the thyroid, lung, stomach and skin resulting from the adult cardiac CTA protocols and are found in Table 10-22. Of these four organs, the best comparison was made for the doses to the lungs and the relative differences range from 2.22 to 8.35%. Dosimeters were placed throughout the lung volume in a systematic way, as described in Section 9.3 and depicted in Figure 9-7, and thus are a good representation of the average organ dose because of a better uniformly-distributed dosimeter placement. Good comparison is also seen for the thyroid and stomach doses. Large relative differences among the skin doses for each protocol are the result of using the entire volume of skin in the MC simulation whereas the dosimeters were placed only on the section of the skin that was in the primary beam and therefore averaged over a smaller area as compared to the simulated skin doses.

While limitations existed in both dosimeter measurements and MC simulations, good comparison between the doses obtained from the two methods was achieved. Although it is clear

that the two methods cannot benchmark each other, the overall good agreement among all of the results allows for some general conclusions to be drawn. First, dosimeter placement within the phantom has a direct effect on the average organ dose, which is critical especially for larger organs. The lungs were well-sampled by the dosimeters for the cardiac protocol and compared well with the MC simulations of the same protocols. Conversely, due to limitations in the access to all areas of the brain in the phantom, the brain doses resulting from the perfusion protocols was not uniformly-sampled and led to larger discrepancies when compared to the corresponding MC-simulated doses. Doses measured in small organs, such as the lenses of the eyes and the thyroid compared well with simulated doses. Generally speaking, the dose comparisons support the methodology used to measure organ doses using the OSL dosimeters with limitations of accessibility for certain organs in the phantom which, account for the few organ doses that were not as comparable between the measured and simulated results.

Table 10-1. Reproducibility of x-ray tube operated in service mode.

Measurement	Measured air kerma (mGy)
1	48.26
2	48.28
3	48.29
4	48.30
5	48.30
6	48.29
7	48.28
8	48.32
9	48.29
10	48.30
Mean (mGy)	48.30
CV	0.03%

Table 10-2. Reproducibility of volumetric clinical protocol.

Measurement		Position within phantom				
		Center	3 o'clock	6 o'clock	12 o'clock	9 o'clock
Measured dose (mGy)	1	20.10	22.12	24.65	22.74	18.96
	2	20.15	21.33	22.98	22.13	20.03
	3	20.64	22.00	25.32	21.88	21.12
	4	20.35	21.72	24.52	24.08	19.31
	5	20.68	21.80	23.00	23.58	19.47
	6	20.17	22.60	26.18	24.74	19.62
	7	20.65	23.30	23.07	26.29	20.67
	8	20.13	21.74	24.10	23.82	19.61
	9	20.59	21.63	23.93	24.99	19.54
	10	20.59	21.31	26.40	21.88	20.95
Mean (mGy)		20.41	21.96	24.42	23.61	19.93
CV		1.2%	2.8%	5.1%	6.2%	3.7%

Table 10-3. Reproducibility of helical clinical protocol.

Measurement		Position within phantom				
		Center	3 o'clock	6 o'clock	12 o'clock	9 o'clock
Measured dose (mGy)	1	76.49	78.78	77.08	81.65	80.13
	2	76.59	78.83	77.20	81.76	80.23
	3	76.60	78.83	77.11	81.80	80.21
Mean(mGy)		76.56	78.81	77.13	81.74	80.19
CV		0.1%	0.0%	0.1%	0.1%	0.1%

Table 10-4. Measured beam energies of scanners used for organ dose measurements.

Nominal tube voltage (kV)	80	100	120	135
Measured tube voltage (kV): 320-slice Scanner	80.9	101.3	121.7	137.8
% Error	1.1	1.3	1.4	2.1
Measured tube voltage (kV): 64-slice Scanner	80.8	100.9	121.7	138.3
% Error	1.0	0.9	1.4	2.4

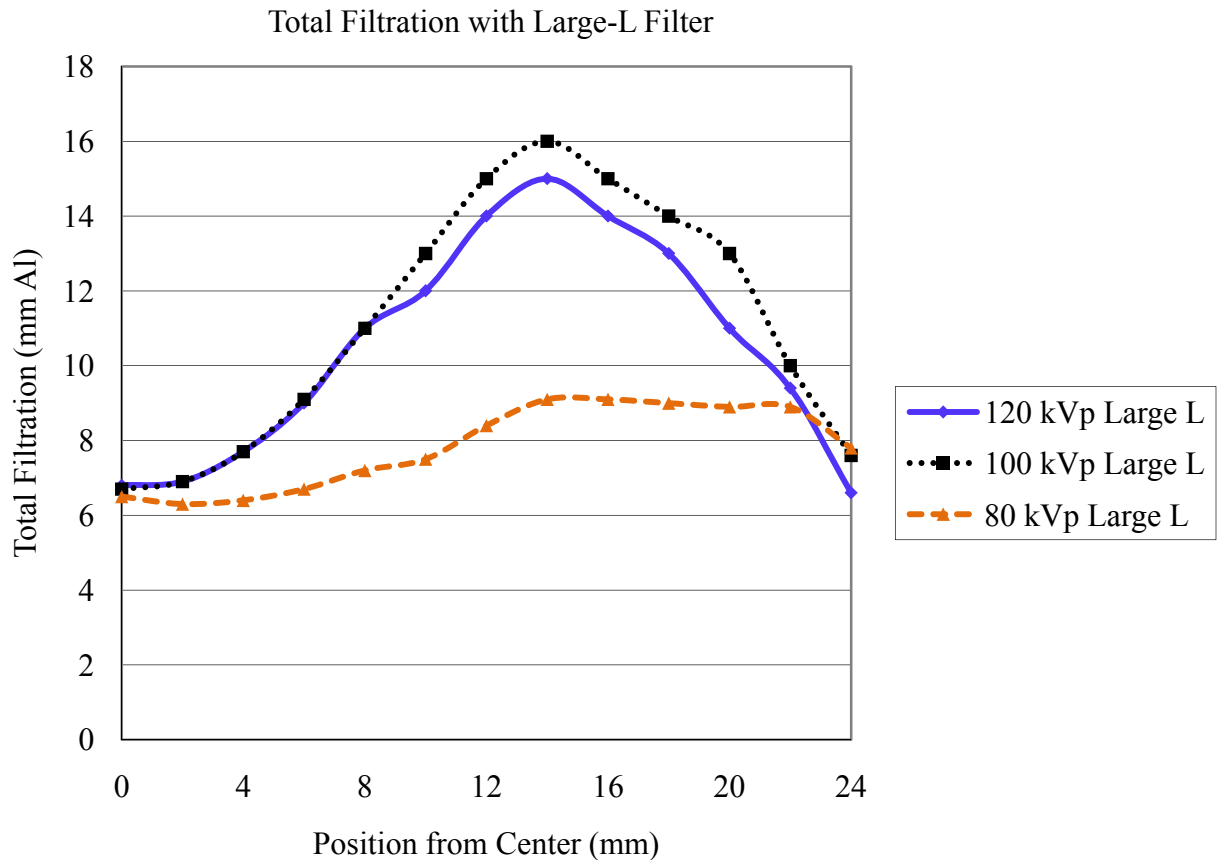


Figure 10-1. Total filtration of x-ray beam using the large filter and depicted for three beam qualities. The increase in total filtration as the distance from isocenter increases is representative of the shape of the bowtie filter.

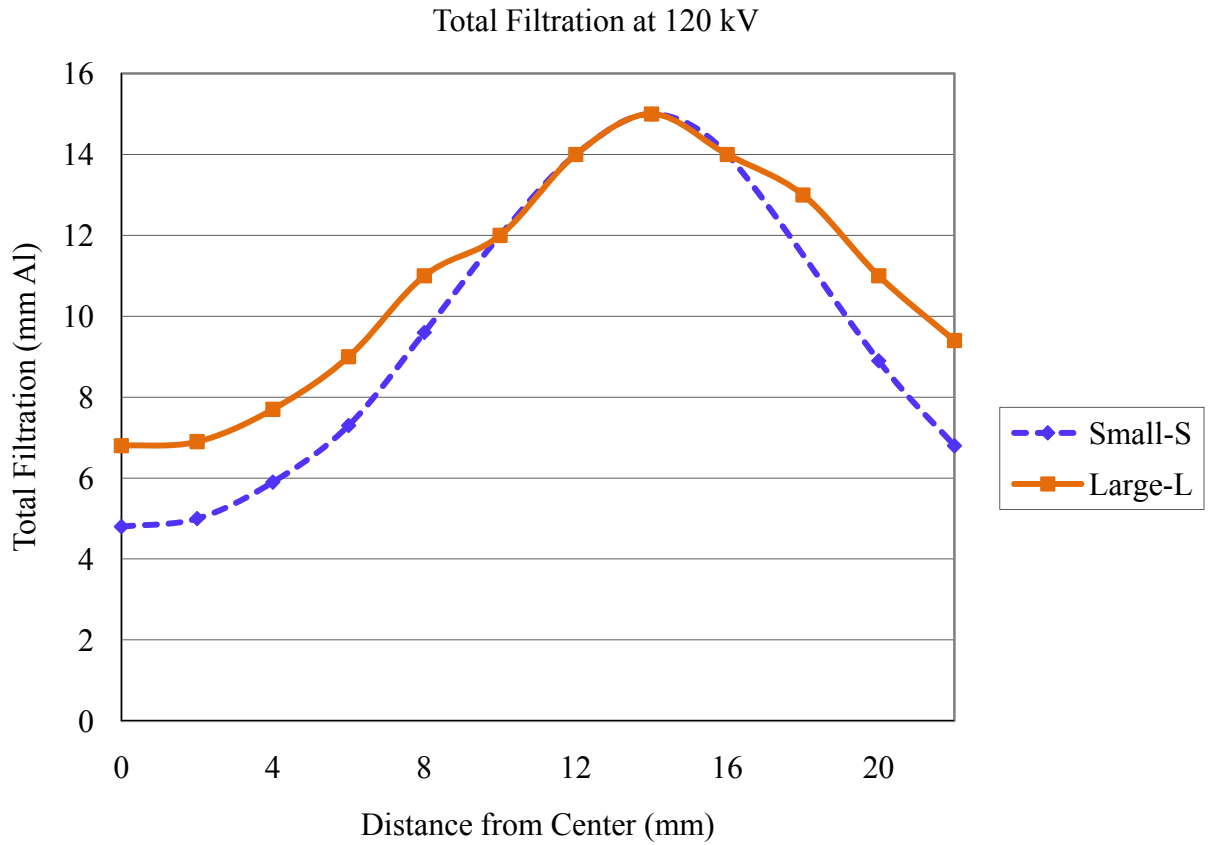


Figure 10-2. Total filtration of x-ray beam for small and large filters using a 120 kV x-ray tube voltage.

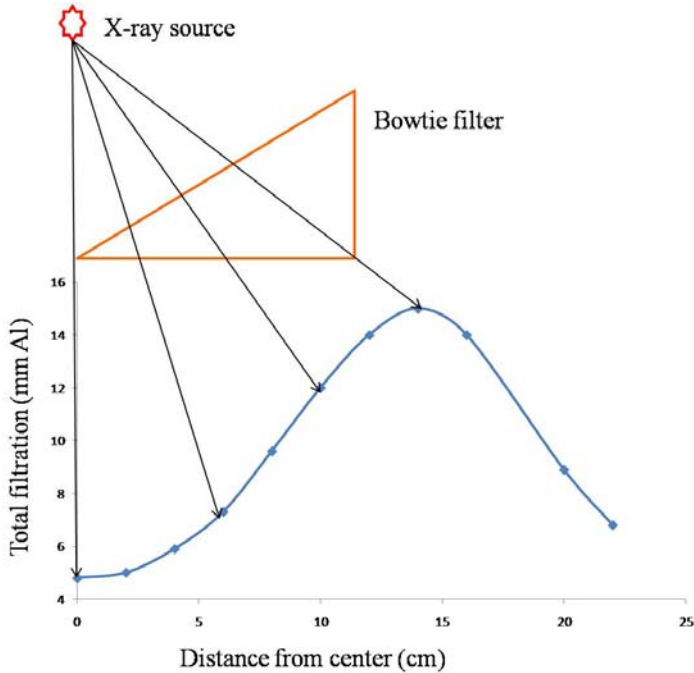


Figure 10-3. Effect of bowtie filter on total filtration measurements. While the exact shape of the bowtie filter is unknown, the shape depicted here is to illustrate the shape of the total attenuation curve.

Table 10-5. Measured HVLs for each nominal x-ray tube voltage for the Aquilion One 320-slice scanner.

Nominal tube voltage	Filter	Measured HVL (mm Al)
80 kV	Small-S	3.90
80 kV	Medium-M/Large-L	4.65
100 kV	Small-S	4.98
100 kV	Medium-M/Large-L	5.80
120 kV	Small-S	6.02
120 kV	Medium-M/Large-L	6.85
135 kV	Small-S	6.76
135 kV	Medium-M/Large-L	7.53

* Note: For simplicity of display, the Medium-M and Large-L filters correspond to the 320-slice scanner.

Table 10-6. Measured HVLS for each nominal x-ray tube voltage for the Aquilion 64 MDCT scanner.

Nominal tube voltage	Filter	Measured HVL (mm Al)
80 kV	Small-S/Small-M	4.84
100 kV	Small-S/Small-M	6.09
120 kV	Small-S/Small-M	7.16
135 kV	Small-S/Small-M	7.92

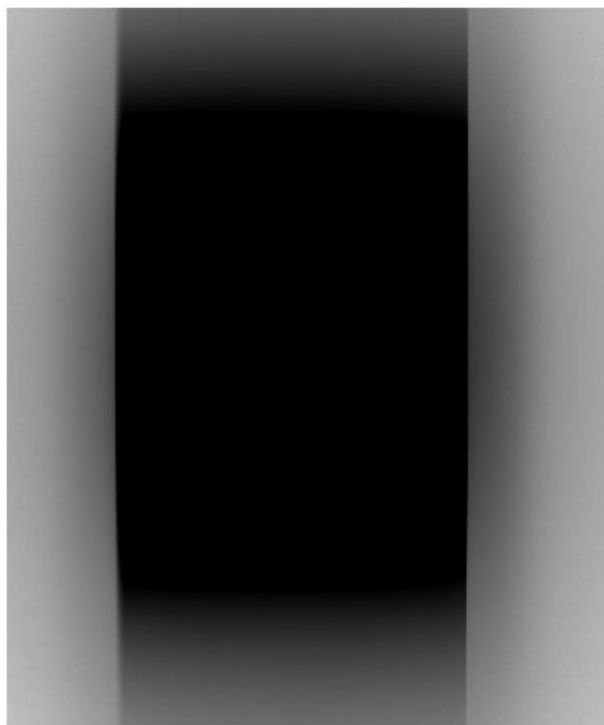


Figure 10-4. Radiographic image of the 16-cm nominal beam width.

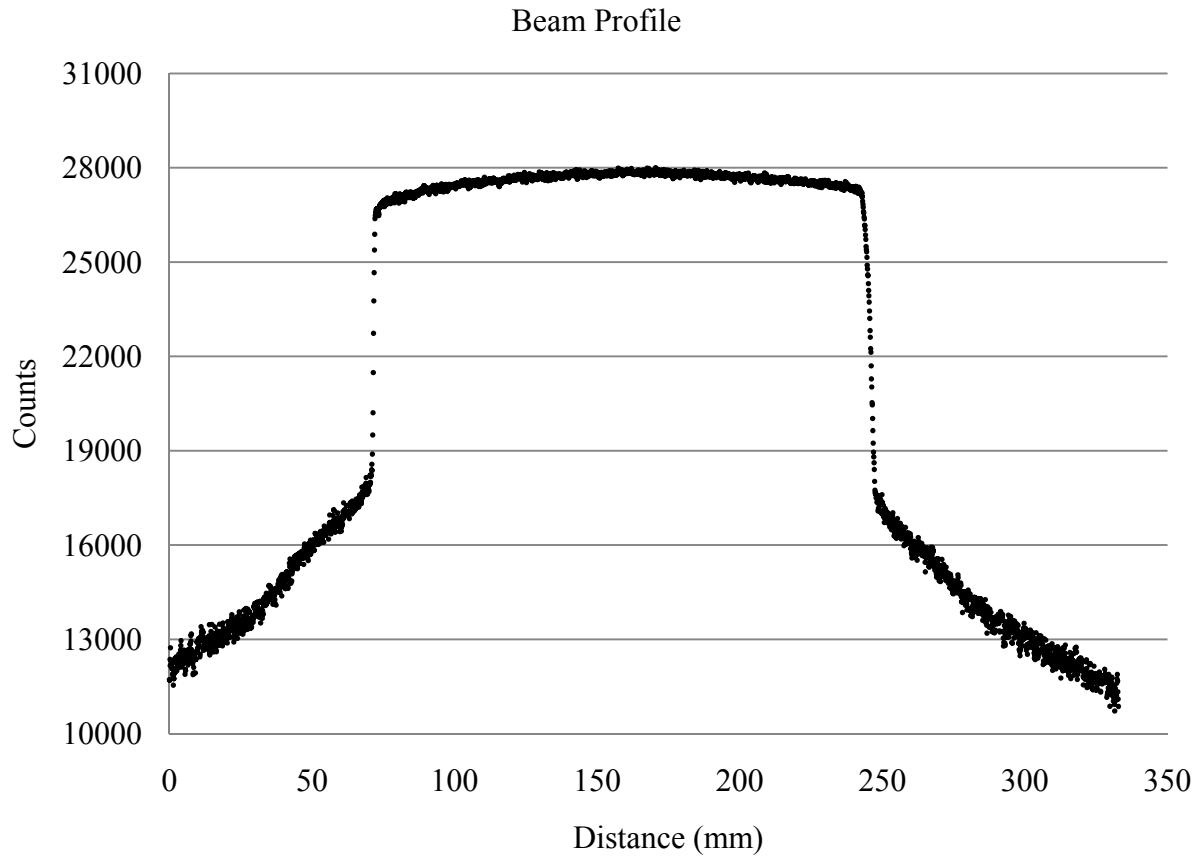


Figure 10-5. Beam profile of the 16-cm nominal CT x-ray beam obtained in air and at scanner isocenter. Gray scale values are plotted as a function of distance.

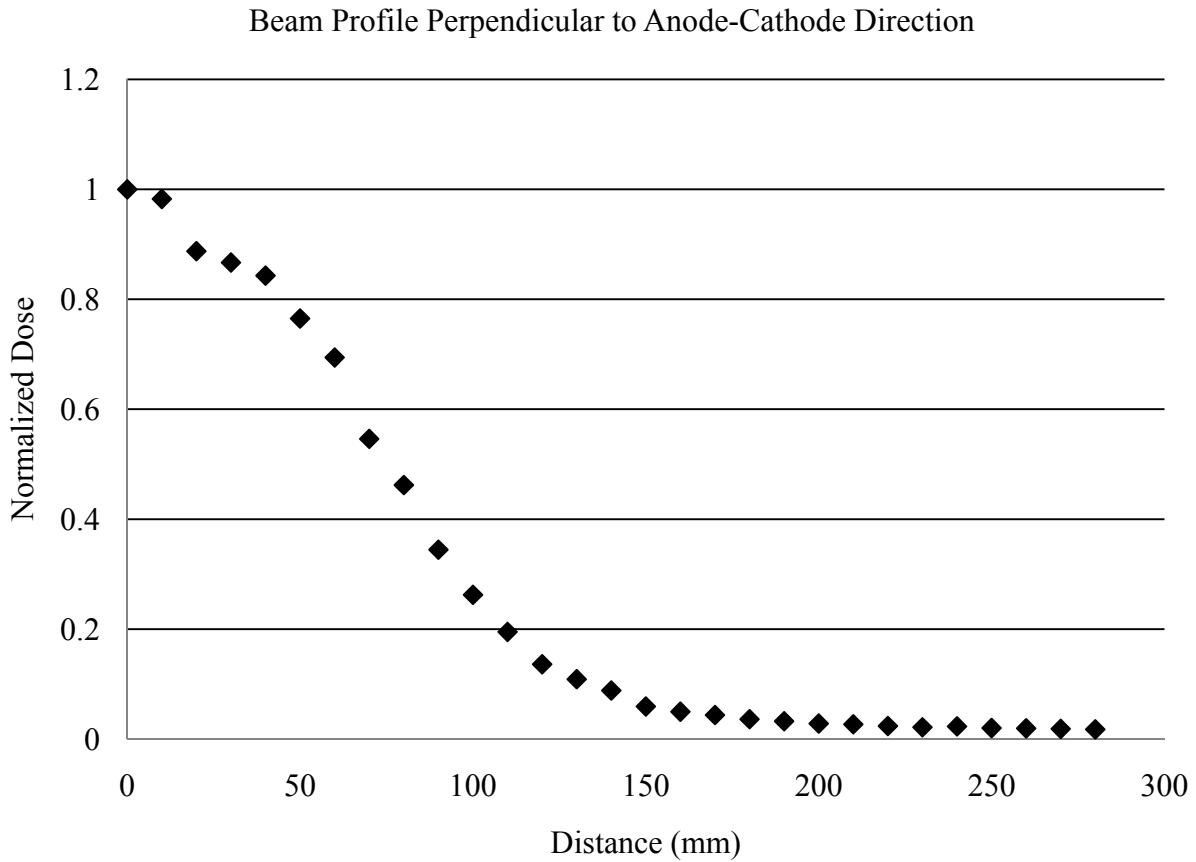


Figure 10-6. Normalized dose in air across the CT scanner gantry perpendicular to the anode-cathode direction.

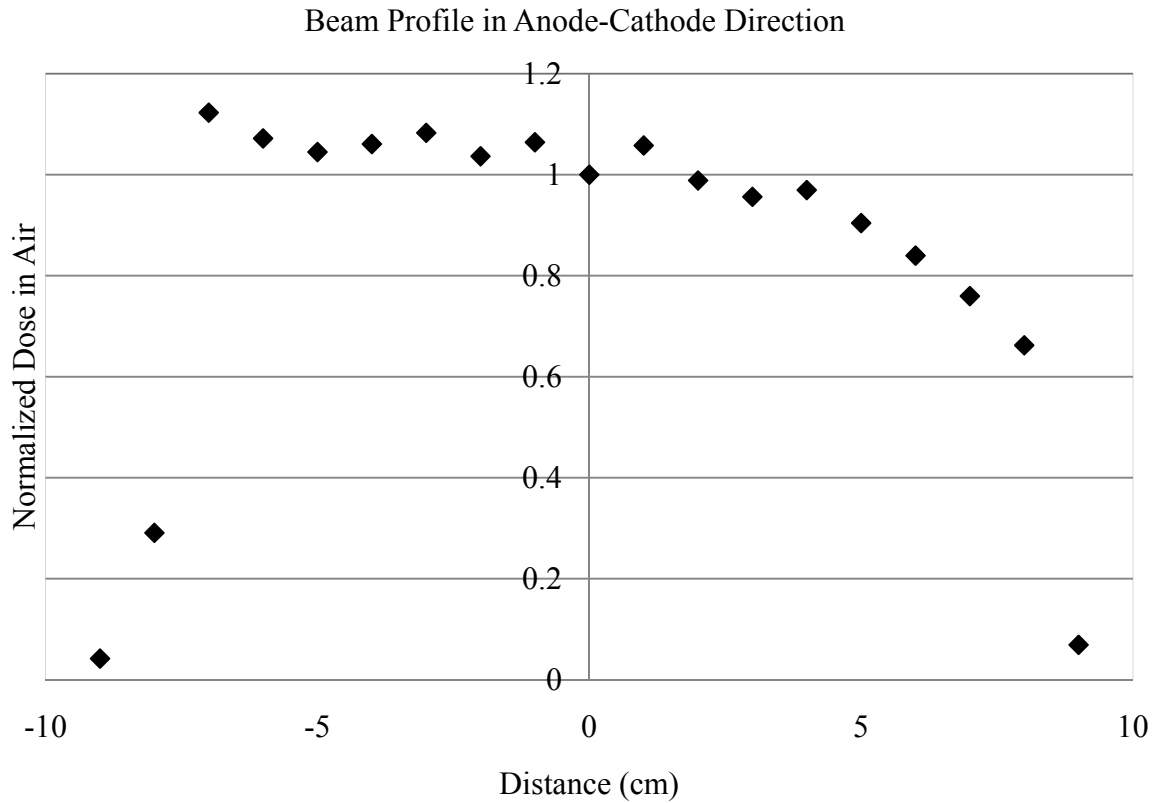


Figure 10-7. Normalized dose in air across the CT scanner gantry in the anode-cathode direction.

Table 10-7. Measurement standards for microStar reader.

Reading	Established average (counts)	Acceptable limits (counts)
DRK	1.6	DRK < 30
CAL	2301.3	2071 < CAL < 2531.4
LED	590.2	531.2 < LED < 649.2

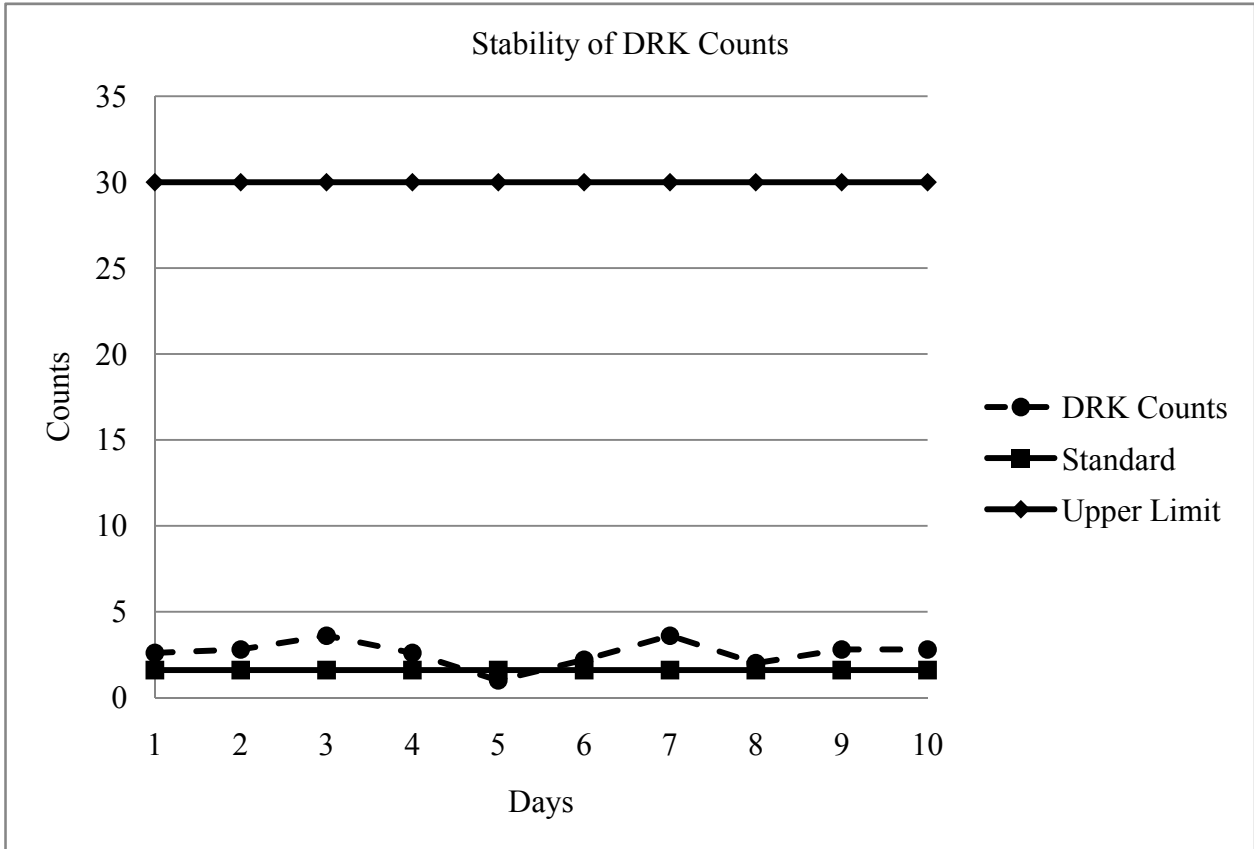


Figure 10-8. Measurement of DRK counts over time, plotted with the standard value and upper limit.

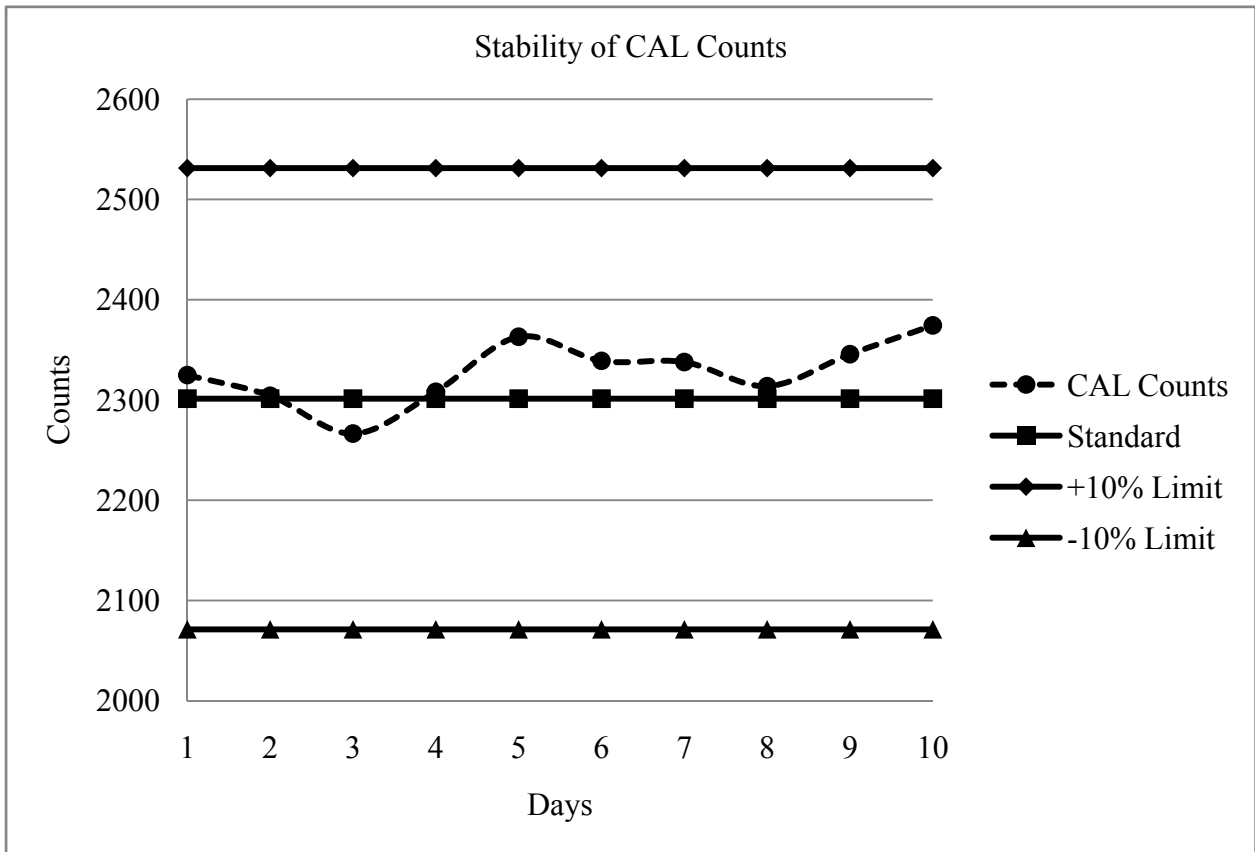


Figure 10-9. Measurement of CAL counts over time, plotted with the standard value and upper and lower limits.

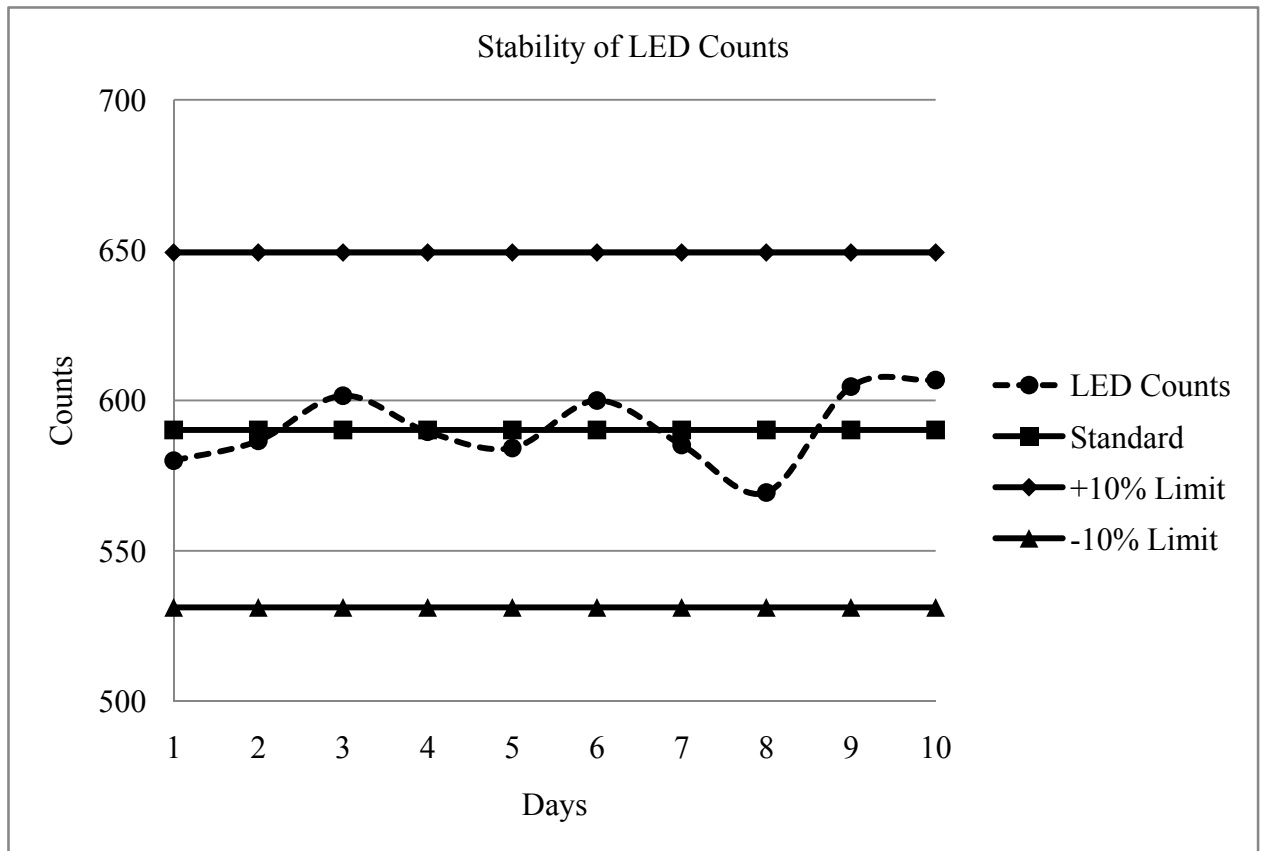


Figure 10-10. Measurement of LED counts over time, plotted with the standard value and upper and lower limits.

Table 10-8. Dose response of standard and screened dots.

	Standard dots	Screened dots
Measured dose (mGy)	43.92	49.00
	48.03	49.66
	50.22	47.78
	48.06	47.06
	45.79	47.18
	49.93	49.67
	45.47	46.47
	46.46	48.52
	48.25	47.82
	47.44	48.00
Mean dose (mGy)	47.36	48.11
CV	4.2%	2.3%

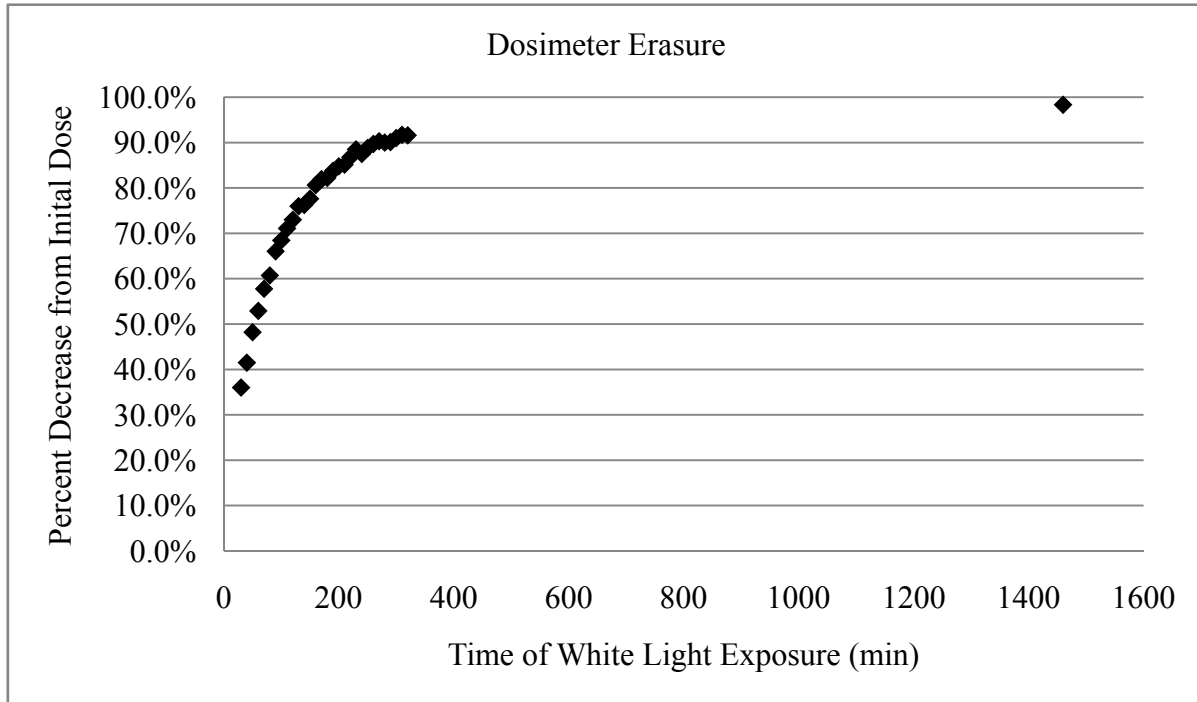


Figure 10-11. Percent decrease from initial dose is displayed as a function of white-light erasure time.

Table 10-9. Energy response of the OSL dosimeters.

	80 kV	100 kV	120 kV	135 kV
Mean dose (mGy) measured by the dosimeters	17.07	27.76	43.75	46.42
Dose (mGy) measured by the ion chamber	16.91	29.2	39.09	56.03
Ratio of mean dosimeter dose to ion chamber dose	1.01	0.95	0.89	0.83

Table 10-10. HVLs used in flat-field scatter response. Aluminum filtration was added to a radiographic x-ray beam to match HVLs measured on the 320-slice scanner.

Tube voltage	Measured CT HVL (mm Al)	Measured HVL of radiographic beam (mm Al)	Difference
80 kV	3.90	3.82	2.1%
100 kV	4.97	5.04	-1.4%
120 kV	6.02	6.02	< 0.5%

Table 10-11. Response of the dosimeters to scatter and a flat x-ray field.

Ratio of dose measured by the dosimeters to that measured by the ionization chamber				
Thickness of acrylic (in)	Nominal tube voltage			
	80 kV	100 kV	120 kV	
0 (surface)	1.05	0.95	0.92	
1	1.04	0.96	0.90	
2	1.01	0.94	0.91	
3	1.01	0.96	0.90	
4	0.98	0.94	0.89	
5	1.01	0.94	0.91	
6	1.01	0.94	0.93	
Minimum	0.98	0.94	0.89	
Maximum	1.05	0.96	0.93	
Mean	1.02	0.95	0.91	

Table 10-12. Response of energy and scatter to the CT x-ray beams used for clinical protocols.

Thickness of acrylic (in)	Ratio of dose measured by the dosimeters to that measured by the ionization chamber					
	80 kV M S	100 kV M S	120 kV M L	100 kV S S	120 kV S S	120 kV M S (64-slice)
0 (surface)	1.01	0.95	0.86	0.96	0.90	0.84
1	0.99	0.90	0.86	0.93	0.89	0.83
2	0.96	0.91	0.86	0.91	0.87	0.83
3	0.97	0.89	0.87	0.90	0.87	0.83
4	0.97	0.90	0.85	0.92	0.88	0.82
Minimum	0.96	0.89	0.85	0.90	0.87	0.82
Maximum	1.01	0.95	0.87	0.96	0.90	0.84
Mean	0.97	0.90	0.86	0.91	0.88	0.83

Note: Tube voltage is given at the top of each column, followed by the bowtie filter (M=medium, S=small) and focal spot size (S=small, L=large).

Table 10-13. The calculated f-factors as a function of HVLs measured for all tube voltage and filter combinations of the clinical CT protocols.

HVL (mm Al)	Effective energy (keV)	$(\mu_{en}/\rho)_{\text{tissue}} (\text{cm}^2/\text{g})$	$(\mu_{en}/\rho)_{\text{air}} (\text{cm}^2/\text{g})$	f-factor
3.87	37.2	9.68E-2	9.18E-2	1.05
4.65	40.5	7.07E-2	6.69E-2	1.06
4.84	41.3	6.85E-2	6.48E-2	1.06
4.88	41.5	6.80E-2	6.44E-2	1.06
5.80	45.2	5.74E-2	5.42E-2	1.06
5.91	45.6	5.61E-2	5.30E-2	1.06
6.09	49.5	4.50E-2	4.23E-2	1.06
6.84	46.4	5.40E-2	5.09E-2	1.06
6.85	49.4	4.52E-2	4.25E-2	1.06
7.16	52.5	4.09E-2	3.84E-2	1.06
7.53	50.8	4.27E-2	4.01E-2	1.07
7.92	53.1	4.02E-2	3.77E-2	1.07

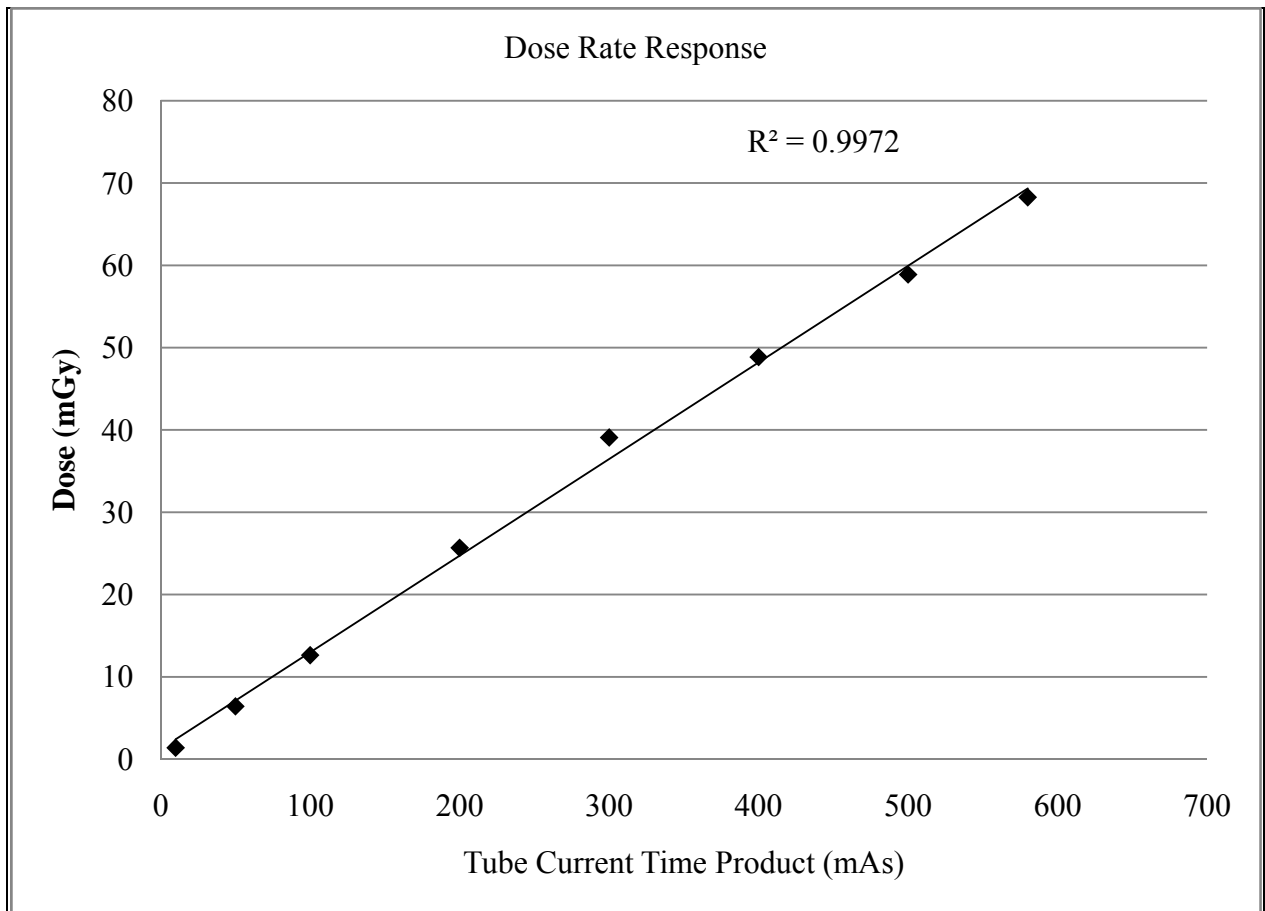


Figure 10-12. Response of the OSL dosimeters to increasing dose rates.

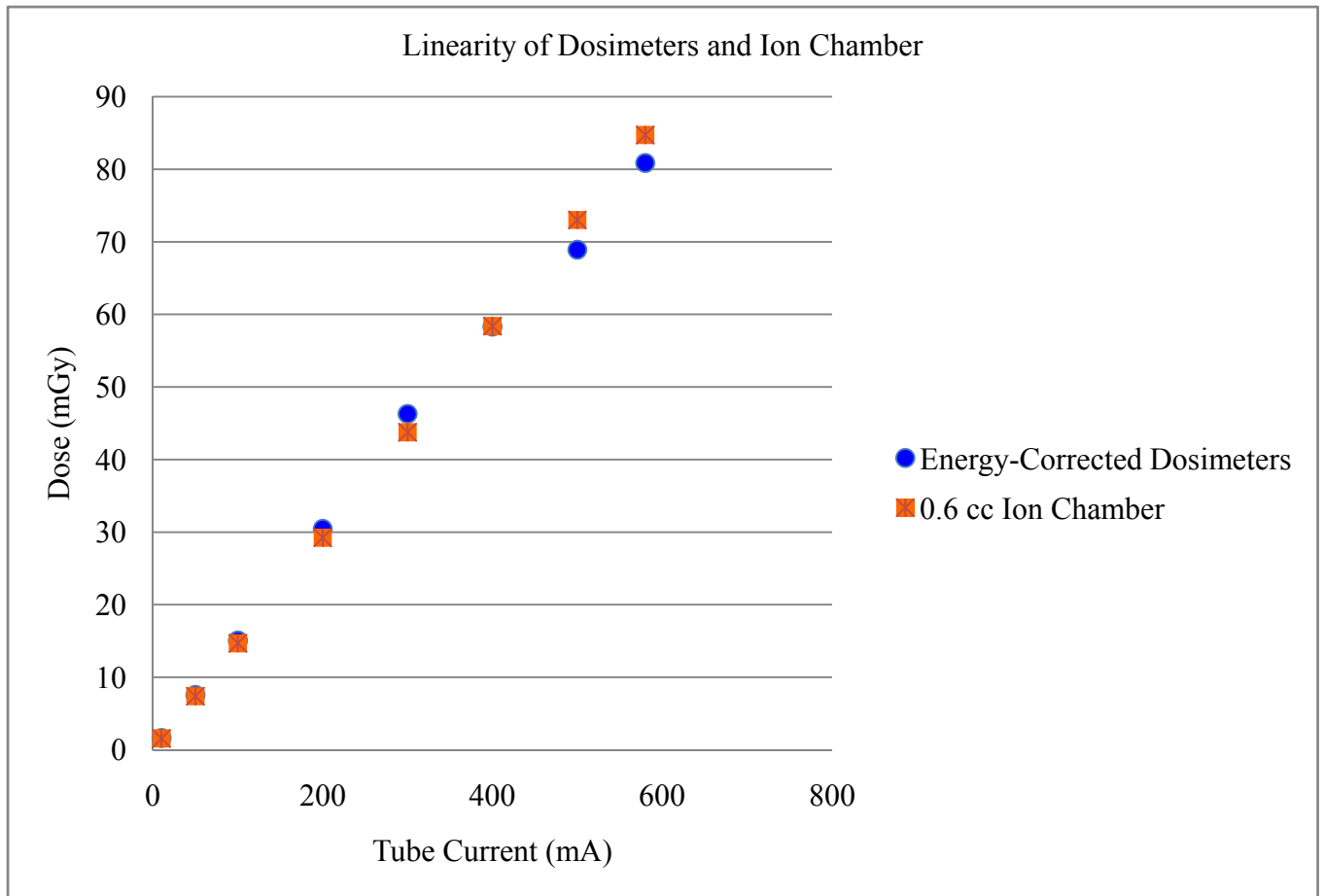


Figure 10-13. Linearity of the energy-corrected dosimeter doses, as depicted with corresponding ion chamber measurements.

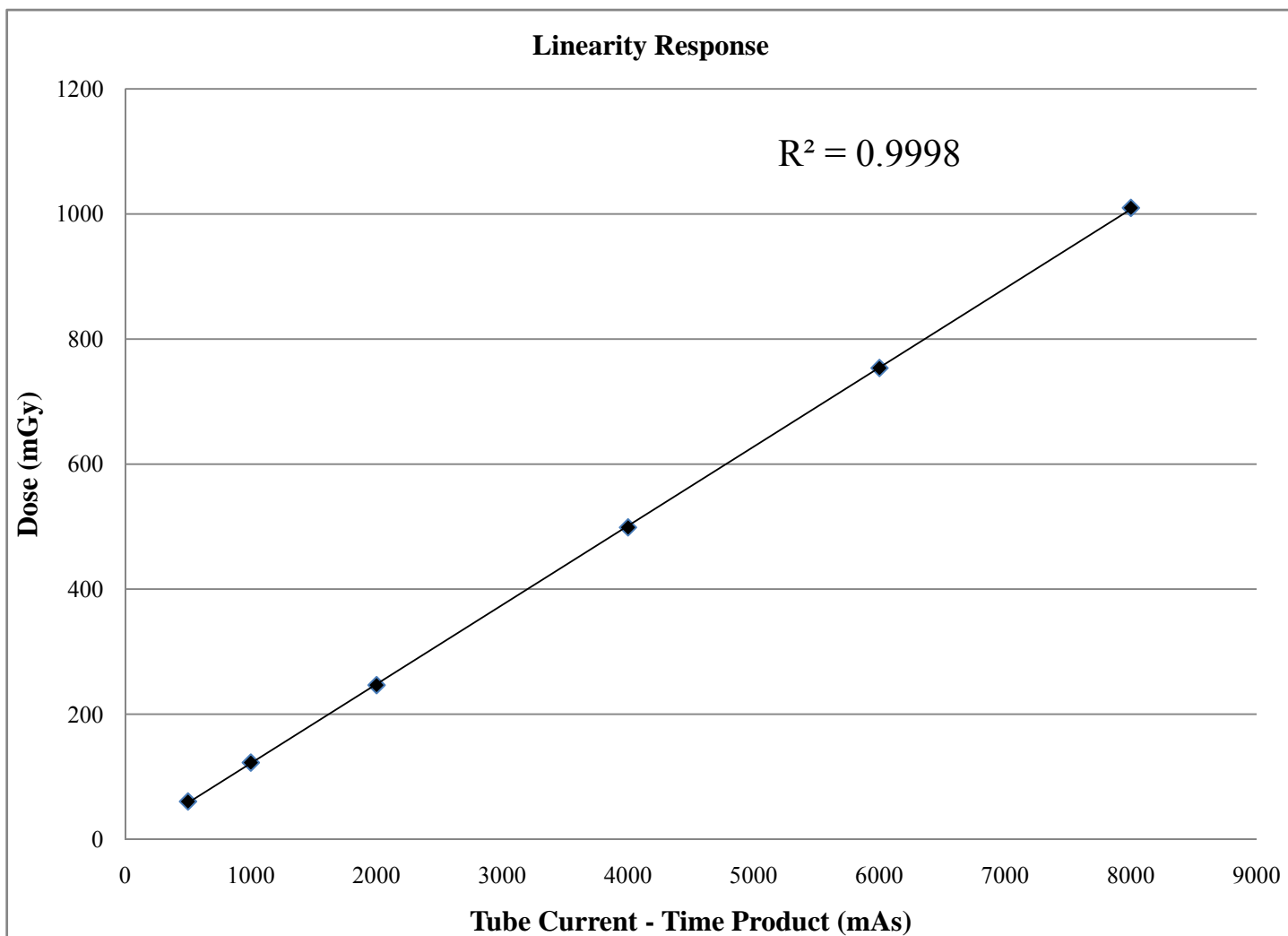


Figure 10-14. Linearity response of the OSL dosimeters to increasing tube currents, representative of the range of doses measured.

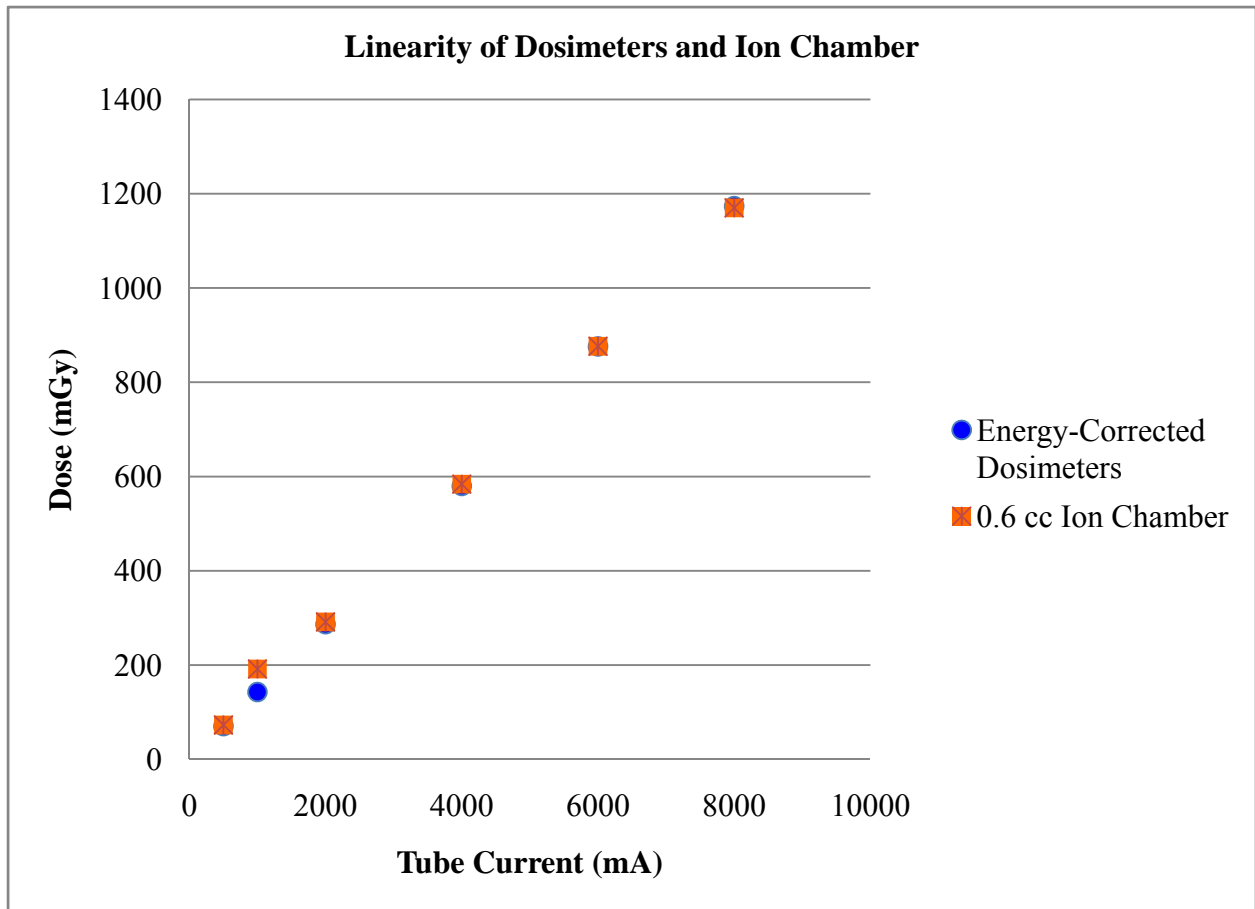


Figure 10-15. Linearity response of the OSL dosimeters and ion chamber to increasing tube currents, representative of the range of doses measured.

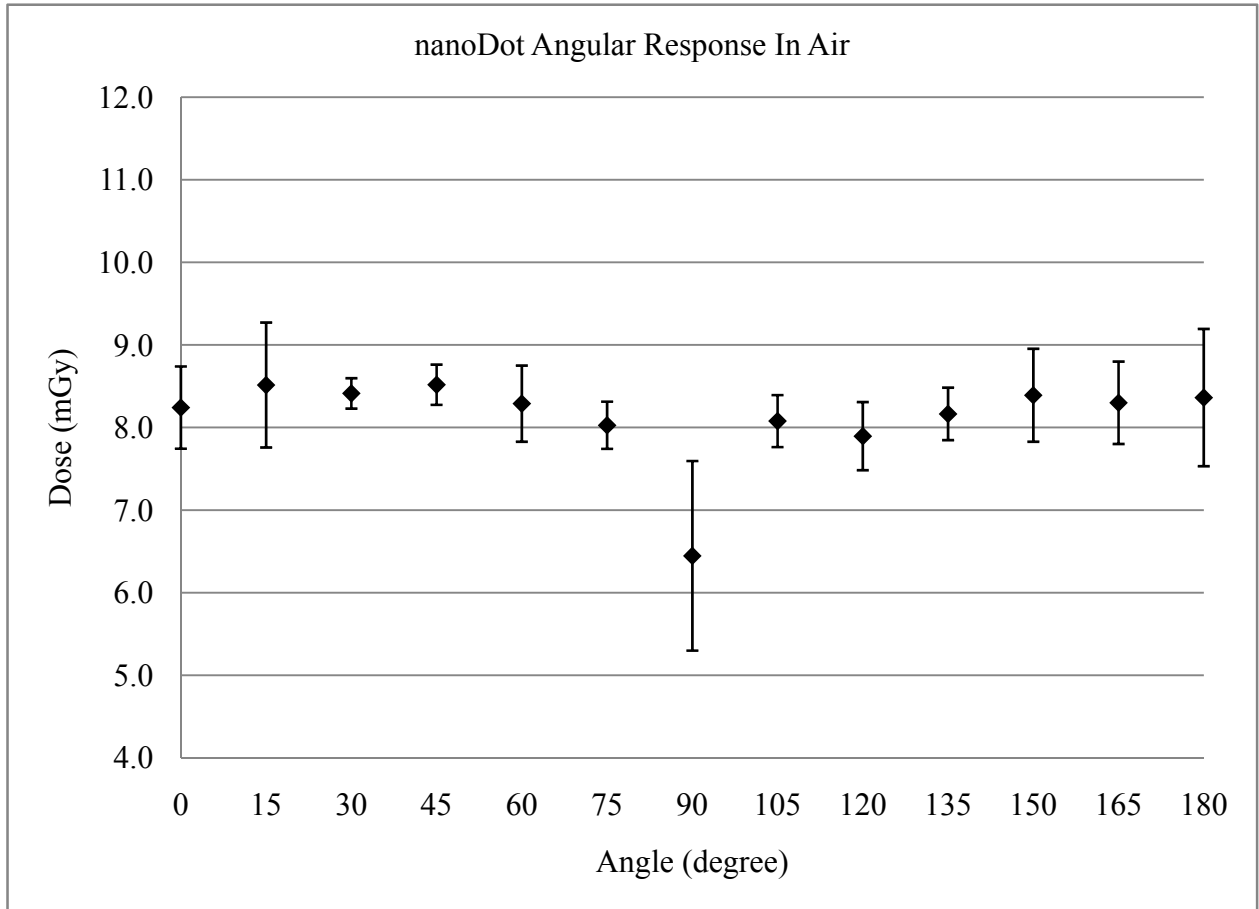


Figure 10-16. Dose absorbed by the nanoDot dosimeters, in air, as a function of x-ray tube angle. Error bars are displayed as the 95% confidence interval.

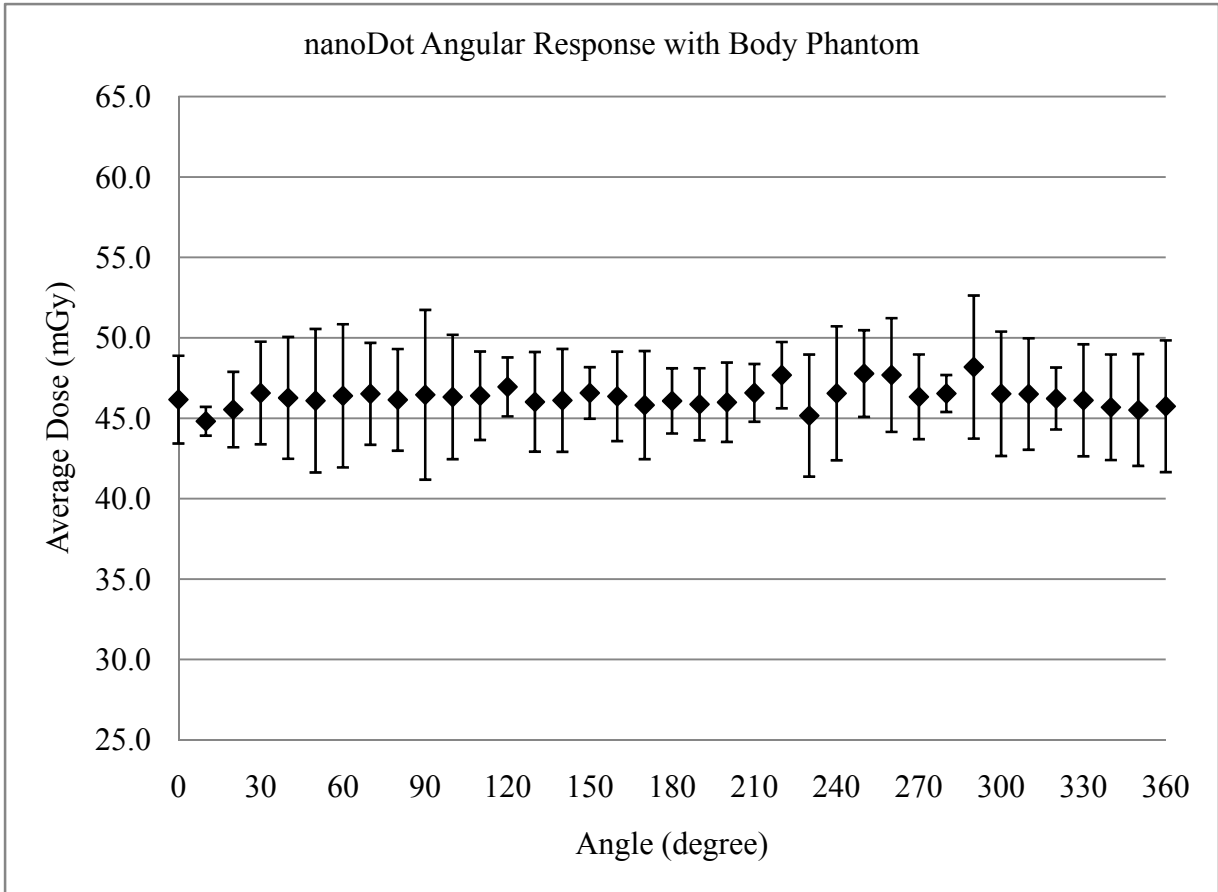


Figure 10-17. Dose absorbed by the nanoDots in the head phantom, displayed as a function of x-ray tube angle and with 95% confidence intervals.

Table 10-14 Mean doses with a 95% confidence interval measured by the dosimeters in and out of their plastic cases in two different positions within the CTDI phantom.

Position	Dosimeter in case	Dosimeter out of case
12 o'clock	10.97 (8.73,13.21) mGy	10.78 (9.79,11.77) mGy
Center	8.54 (7.88,9.20) mGy	8.28 (7.64,8.92) mGy

Table 10-15. Mean organ doses for pediatric craniosynostosis protocol.

Scanner	Tube voltage	Eff. mAs	No. of Scans	Mean organ doses (mGy)			
				Skin	Lens of eye	Thyroid	Breast
320-slice	120 kV	121	1	18.98	22.14	1.95	0.81
			5	18.95	23.24	1.85	0.84
320-slice	100 kV	121	1	12.02	13.85	1.15	0.48
			5	12.85	15.18	1.17	0.50
64-slice	120 kV	157	1	22.97	25.63	6.79	1.55
			5	24.07	25.54	7.39	1.56

Table 10-16. Organ doses measured using the pediatric phantom and craniostynosis protocol; mean and maximum report with 95% confidence interval.

Scanner	Tube voltage	Organ Doses (mGy)			
		Skin	Lens of eye	Thyroid	Breast
320-slice 120 kV	Mean	18.98	22.14	1.95	0.81
	Maximum	22.57	24.08	2.13	1.30
	95% CI	(15.62,22.33)	(19.73,24.55)	(1.67,2.23)	(0.51,1.11)
320-slice 100 kV	Mean	12.02	13.85	1.15	0.48
	Maximum	14.21	15.33	1.22	1.14
	95% CI	(10.28,13.76)	(12.53,15.17)	(1.01,1.30)	(0.19,0.78)
64-slice 120 kV	Mean	22.97	25.63	6.79	1.55
	Maximum	28.24	32.40	8.30	2.01
	95% CI	(18.10,27.84)	(13.31,37.95)	(4.84,8.73)	(1.02,2.08)

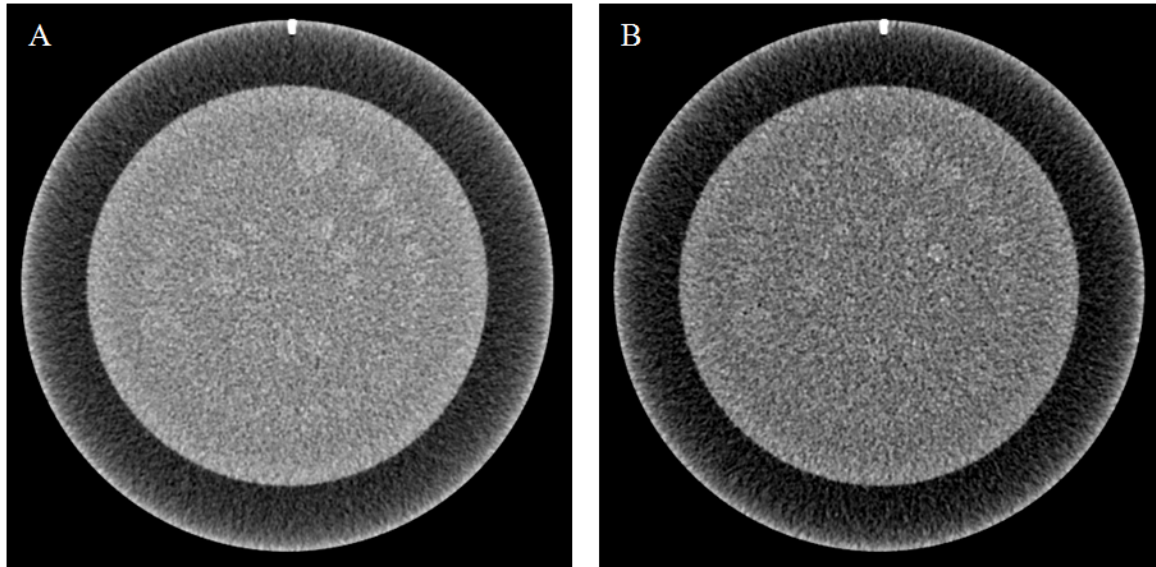


Figure 10-18. Image quality phantom images for pediatric protocol image using, A) 120 kV and, B) 100 kV. All other parameters remained the same.

Table 10-17. Number of low-contrast objects viewed using pediatric craniosynostosis protocol parameters.

Viewer	Energy (kV)	Number of observed low-contrast objects						Total
		A	B	C	D	E	F	
1	120	6	3	3	3	3	2	20
	100	5	2	0	2	1	0	10
2	120	6	4	0	2	3	1	16
	100	5	4	1	3	3	0	16
3	120	6	2	0	3	3	1	15
	100	5	4	1	3	3	0	16
Mean		A-C	D-F	Total				
	120	10	7	17				
	100	9	5	14				

Table 10-18. Mean organ doses resulting from brain perfusion protocol.

Protocol	Tube voltage (kV)	No. of scans	Mean organ doses (mGy)					
			Esophagus	Thyroid	Brain	Skin	Breast	Eyes
Manufacturer	80	5	2.47	3.90	168.96	225.84	1.09	263.88
		1	3.02	3.63	189.72	250.64	1.21	286.18
Manufacturer	100	5	5.22	7.96	325.71	392.39	2.23	459.18
		1	6.85	7.81	349.89	407.94	2.50	465.88
Manufacturer	120	5	9.02	13.28	530.80	569.76	3.46	660.09
		1	12.30	13.22	588.91	650.98	3.93	723.84
Continuous	80	5	3.46	5.02	193.56	233.32	1.41	263.54
		1	3.57	4.20	203.63	250.06	1.54	296.42
mA boost	80	5	3.43	5.14	191.76	241.37	1.42	273.08
		1	3.59	4.30	196.81	266.24	1.57	293.98
64-slice	120	5	5.02	7.04	419.59	1175.70	2.24	198.15
		1	4.95	6.95	457.15	1240.97	2.22	205.33

Note: Mean organ doses measured with a single scan are reported on the first line. Mean organ doses measured using five consecutive scans are reported on second line.

Table 10-19. Mean and maximum organ doses in mGy measured with adult brain perfusion protocol.

Protocol		Organ					
Tube voltage		Esophagus	Thyroid	Brain	Skin	Breast	Eyes
Manufacturer 80 kV	Mean	2.47	3.90	168.96	225.84	1.09	263.88
	Maximum	3.42	4.09	191.14	253.24	1.24	284.58
	95% CI	(1.17,3.78)	(3.61,4.20)	(144.70,193.22)	(194.49,257.19)	(0.83,1.35)	(229.64,298.12)
Manufacturer 100 kV	Mean	5.22	7.96	325.71	392.39	2.23	459.18
	Maximum	7.25	8.27	351.31	410.54	2.52	464.28
	95% CI	(2.09,8.35)	(7.47,8.46)	(285.97,365.44)	(371.23,413.56)	(1.72,2.74)	(453.11,465.25)
Manufacturer 120 kV	Mean	9.02	13.28	530.80	569.76	3.46	660.09
	Maximum	12.71	13.68	590.33	653.59	3.95	722.25
	95% CI	(2.90,15.13)	(12.62,13.94)	(444.43,617.17)	(465.12,674.41)	(2.67,4.25)	(558.78,761.41)
Continuous 80 kV	Mean	3.46	5.02	193.56	233.32	1.41	263.54
	Maximum	4.87	5.19	208.05	254.14	1.62	290.46
	95% CI	(2.18,4.74)	(4.79,5.24)	(180.08,207.03)	(218,248.25)	(1.19,1.63)	(238.31,288.77)
mA boost 80 kV	Mean	3.43	5.14	191.76	241.37	1.42	273.08
	Maximum	4.89	5.29	201.23	270.32	1.65	288.02
	95% CI	(2.13,4.73)	(4.98,5.30)	(1.83,199.87)	(217.48,265.27)	(1.18,1.66)	(256.10,290.06)
64-slice 120 kV	Mean	5.02	7.04	419.59	1175.70	2.24	198.15
	Maximum	6.74	7.27	529.61	1225.80	2.39	203.66
	95% CI	(2.01,8.04)	(6.42,7.65)	(305.47,533.70)	(1112.88,1238.52)	(1.92,2.55)	(187.61,208.69)

172

Table 10-20. Mean organ doses in mGy resulting from adult cardiac protocol.

Protocol	No. of Scans	Organs				
		Thyroid	Lung	Stomach	Breast	Skin
Prospectively-gated CTA	5	2.50	13.94	2.08	20.10	21.29
	1	2.55	15.22	2.09	25.18	27.09
Functional analysis	5	7.81	43.77	6.25	67.72	69.98
	1	8.16	46.09	6.28	68.52	71.49
Functional Analysis with dose modulation	5	4.61	26.07	3.73	40.03	41.84
	1	4.76	27.82	3.79	41.56	43.95
Cardiac CTA (64-slice)	5	5.93	52.03	55.95	100.11	97.24
	1	5.81	52.46	62.91	97.60	32.40

Table 10-21. Mean and maximum organ doses in mGy resulting from adult cardiac protocol.

Protocol		Organs				
		Thyroid	Lung	Stomach	Breast	Skin
Prospectively-gated	Mean	2.50	13.94	2.08	20.10	21.29
	Maximum	2.61	20.62	2.78	24.75	25.05
	95% CV	(2.26,2.61)	(7.50,20.38)	(1.15,3.01)	(15.81,24.39)	(16.30,26.29)
Functional analysis	Mean	7.81	43.77	6.25	67.72	69.98
	Maximum	8.54	61.76	8.66	80.60	81.34
	95% CV	(6.38,9.25)	(24.07,63.47)	(3.29,9.21)	(55.53,79.90)	(54.99,84.96)
Functional Analysis with dose modulation	Mean	4.61	26.07	3.73	40.03	41.84
	Maximum	4.74	36.06	4.87	52.97	48.25
	95% CV	(4.23,4.98)	(14.31,37.83)	(1.90,5.56)	(29.79,50.27)	(33.52,50.15)
64-slice scanner	Mean	5.93	52.03	55.95	100.11	97.24
	Maximum	6.16	105.08	86.21	139.37	124.99
	95% CV	(5.31,6.54)	(0,113.81)	(18.54,93.36)	(58.37,141.85)	(58.04,136.44)

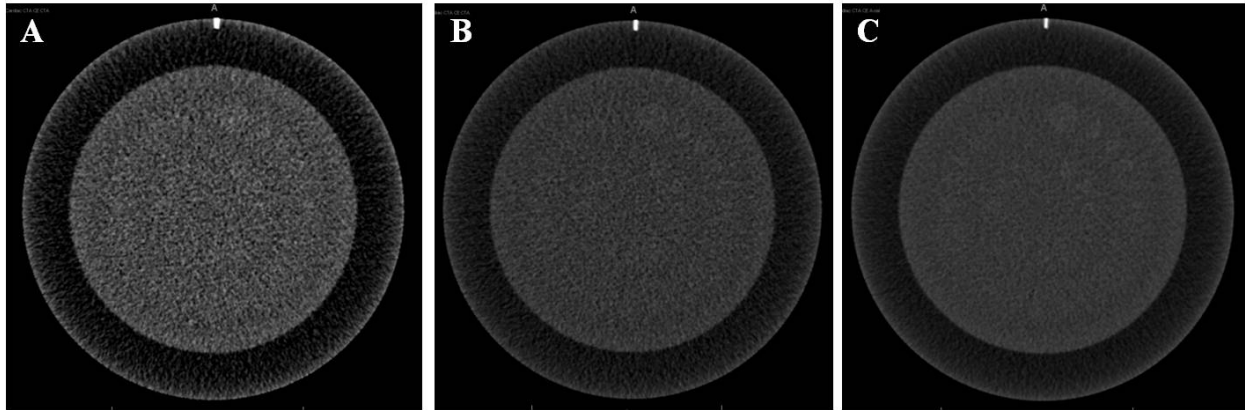


Figure 10-19. Image quality phantom images for cardiac protocol. A) imaged using 0.5 mm slices, B) using 1.0 mm slices, and C) 3.0 mm slices. All other parameters remained the same.

Table 10-22. Organ dose comparison for the 320-slice CT pediatric craniosynostosis protocol between measured doses (mGy) and Monte Carlo (MC) simulated doses (mGy).

	120 kV				100 kV			
	OSL		MC	Rel. Diff. (%)	OSL		MC	Rel. Diff. (%)
	max	mean	max		mean			
Skin	22.57	18.98	19.96	-4.91	14.21	12.02	13.11	-8.31
Lenses	24.08	22.14	21.36	3.54	15.33	13.85	13.62	1.69
Thyroid	2.13	1.95	2.20	-11.36	1.22	1.15	1.28	-10.16

Table 10-23. Organ dose comparison for the 320-slice CT adult brain protocols between measured doses (mGy) and Monte Carlo (MC) simulated doses (mGy).

Protocol		Organ				
		Esophagus ^a	Thyroid ^b	Brain ^c	Skin ^d	Eyes ^e
Manufacturer 80 kVp	OSL	2.47	3.90	168.96	225.84	263.96
	MC	1.56	4.50	221.97	337.40	247.64
	Rel. Diff. (%)	58.33	-13.33	-23.88	-33.06	6.53
Manufacturer 100 kVp	OSL	5.22	7.96	325.71	392.40	459.26
	MC	3.56	9.72	420.92	501.27	428.61
	Rel. Diff. (%)	46.63	-18.11	-22.62	-21.72	7.13
Manufacturer 120 kVp	OSL	9.02	13.28	530.80	569.77	697.53
	MC	6.39	17.02	678.97	710.98	675.52
	Rel. Diff. (%)	41.16	-21.97	-21.82	-19.86	3.28
Continuous	OSL	3.46	5.01	193.56	233.33	269.74
	MC	2.29	6.40	260.18	273.12	264.43
	Rel. Diff. (%)	51.09	-21.56	-25.61	-14.57	-0.34
mA Boost	OSL	3.43	5.14	191.76	241.38	273.24
	MC	2.29	6.42	261.28	274.42	265.60
	Rel. Diff. (%)	49.78	-19.94	-26.61	-12.04	2.82

^along organ outside of primary beam; ^bsmall organ outside primary beam; ^clarge organ inside primary beam; ^donly volume of skin inside the primary beam was included in simulation; ^esmall organ inside primary beam

Table 10-24. Organ dose comparison for the 320-slice CT adult cardiac CTA protocols between measured doses (mGy) and Monte Carlo (MC) simulated doses (mGy).

Protocol		Organ Dose (mGy)			
		Thyroid ^a	Lung ^b	Stomach ^c	Skin ^d
Prospectively-gated CTA	OSL	2.50	13.94	2.08	21.29
	MC	2.76	15.21	2.97	17.34
	Rel. diff. (%)	-9.42	-8.35	-29.97	22.78
Functional Analysis (CFA)	OSL	7.81	43.77	6.25	69.98
	MC	8.12	44.76	8.75	51.02
	Rel. diff. (%)	-3.82	-2.21	-28.57	32.16
CFA with Dose Modulation	OSL	4.61	26.07	3.73	41.84
	MC	4.88	26.90	5.26	30.66
	Rel. diff. (%)	-5.53	-3.00	-29.00	36.46

^asmall organ outside primary beam; ^blarge organ inside primary beam; ^clarge organ at the edge of the primary beam; ^donly volume of skin inside the primary beam was included in simulation

CHAPTER 11 SUMMARY AND CONCLUSIONS

11.1 Summary of This Research Project

There were several purposes of this research project, each of which was completed with a methodical process and in the most efficient way possible. A standardized set of CT protocols was created by the RPC, and volumetric protocols were developed for the wide-beam technology of the 320-slice scanner. Scan parameters were chosen by the radiologists on the committee, who also assessed the image quality of these protocols in a clinical setting. Medical physicists on the committee were successful in assessing dose considerations of the chosen scan parameters. With the CT protocols standardized and established at Shands at UF, an OSL dosimetry system was verified for its use in clinical CT dosimetry. Several characteristics of the system were described, including the ability to erase the dose on the dosimeters using exposure to room light, the ability to reuse the dosimeters; energy, scatter, linearity and angular responses; as well as the ability to take the OSL material out of its case for select dose measurements. Because of the advancements in CT technology and the wide beam width of the 320-slice scanner used in this research project, several characteristics of the scanner and x-ray beams were described, including reproducibility, tube voltage accuracy, HVL, beam width and dose profiles. With both the dosimetry system and CT scanner characterized, organ dose measurements were made for three clinical protocols that were approved and implemented by the RPC. Physical, tomographic phantoms were used to measure organ doses in select organs that were in the direct radiation field, or close enough to it to receive a significant amount of scatter. Organ dose measurements were made on two separate CT systems for comparison: a wide-beam 320-slice scanner and a 64-slice MDCT scanner. Finally, image quality was assessed for the three protocols. This analysis was done by a neuroradiologist on the RPC during the clinical

development of the brain perfusion protocol. An image quality phantom was used to assess the low-contrast resolution of the pediatric head adult cardiac protocols, and analysis was performed by medical physicists.

The combination of dosimetry system, tomographic phantoms and 320-slice volumetric CT scanner makes this research project unique to any other. There has very little work to date published with commercial OSL dosimeters in the diagnostic energy range; a complete evaluation of the system for use in CT was completed through the work of this research project and verified for use. A method is described that details measurements needed to correct for energy and scatter for dose measurements made on other CT systems. The small dosimeters allowed for numerous point organ doses to be made at one time, thus streamlining the measurement process and overcoming some of the challenges to established dose metrics in CT. Because organ doses were measured directly, scattered radiation was captured by the dosimeters and therefore representative of true organ dose measurements.

While physical, tomographic phantoms have been used by others at UF, they have not been used with these OSL dosimeters in a wide-beam MDCT scanner. Shands at UF is one of the few hospitals in the world with the Aquilion ONE 320-slice CT system. Dose measurements resulting from the 320-slice scanner that have been reported to date have been in the form of effective dose and the CTDI values displayed by the scanner, and not actual organ doses. Furthermore, comparisons were made between clinical volumetric and helical protocols, and a dose reduction was reported in most cases using the volumetric scanner for the protocols evaluated. Specifically, doses measured on the Aquilion One were lower than the 64-slice scanner for all organs evaluated with the pediatric craniosynostosis protocol. The skin dose measured with the brain perfusion protocol was at least two times higher on the 64-slice scanner

compared to the Aquilion One, and this measured skin dose approaches the threshold for radiation-induced skin effects. With the exception of the thyroid, all organ doses compared using the adult cardiac CTA protocol were higher on the 64-slice scanner than on the Aquilion One. The clinical impact of these findings is tremendous, especially in the case of pediatric patients. A recommendation to scan pediatric patients with the 320-slice scanner will save radiation dose to the patient, in accordance with the ALARA principle.

11.2 Future Work

The precision of the OSL dosimeters has been described in this dissertation; however, their accuracy must be benchmarked against a known and proven radiation dose-measuring instrument. The accepted benchmark is a small-volume Farmer chamber, or any small-volume ionization chamber that is calibrated in the energy range for which it will be used. To satisfy these conditions to benchmark the dosimeters, the 0.6-cc ion chamber was calibrated at 100 kV for use in this research project and was the initial approach to quantifying the energy and scatter responses of the dosimeters; future work should include an investigation into the energy and scatter characteristics of the 0.6-cc chamber to conduct a better assessment of the accuracy of the dosimeters.

If organ doses were to be measured in the future using the methodology presented in this dissertation on a CT scanner other than the two specific scanners used in this research project, a minimal number of measurements will need to be made, especially the measurements detailed in Sections 8.2.5 through 8.2.6 to correct the non-uniform response of the dosimeters to energy and scatter. While the method recommended by the author is the use, for these measurements, the exact scanner to be used for organ dose measurements, the flat-field measurements described in Section 8.2.5 could also be used if a service mode in the CT scanner was not available to allow stationary CT exposures. If the flat-field method is followed, the second HVL should be

measured after filtration has been added to the radiographic tube in order to compare the homogeneity coefficients of the radiographic tube with added filtration to those of the CT x-ray tube, at each tube voltage and bowtie filter combination to be used for organ dose measurements. This comparison would require, of course, the additional measurements of the second HVL in the CT scanner, but would provide a better assessment and comparison of the two beams.

Furthermore, future work should include measuring the HVLs of the CT scanner across the gantry at the same tube voltage and bowtie filter combination to analyze any effect of the shape of the bowtie filter on the dosimeter energy response. Further investigation into the characteristics of the bowtie filters could include analysis using a different method to measure total filtration. The instrument used in this research project may respond differently to different angle of x-ray beam incidence, meaning that the methodology followed was to move the instrument across the CT scan gantry thereby making the initial measurement at isocenter when the beam is perpendicular to the instrument (0°); as measurements were made at increasing distance away from isocenter, the angle of incidence also increased and could have affected the measurements of total filtration.

Future work that could be continued as an extension of this research project could include measuring organ doses for other clinical protocols. The RPC has discussed linking a range of doses to each protocol. This information would be available with all other information pertaining to the CT scan. While organ doses should not be the prime reason for ordering a particular diagnostic study, they should be a consideration. A dose range could help a physician choose between a CT and MR protocol, assuming both provide the necessary information for proper diagnosis. Furthermore, a dose range for each protocol would lay the groundwork for tracking the total dose accumulated by a patient resulting from medical exposures. If the dose

information for a CT scan is available, it could be put into the patient's medical record and followed over time.

A female tomographic phantom is currently in development at UF. Where the average female size is smaller than that of a man, organ doses are expected to be different. Similarly, the female phantom has breast tissue and structure, which would allow for more realistic breast dose measurements. Similarly, as the family of physical, tomographic phantoms developed by the UF group continues to grow, there will be more phantoms with which to make these types of organ dose measurements.

The issue of using small dosimeters to obtain an average organ dose was addressed in 10.3. An issue with all dose measurements is the number of (approximate) point dose measurements needed to calculate an average dose accurately. Theoretically, an infinite number of point doses is needed for a true average dose. However, doing so is not realistic in any. Now that a method has been established to reliably measure organ doses with the dosimeters and physical phantoms, future work in this area could include determining the minimum number of dosimeters needed to measure an accurate average dose.

Finally, this research project focused on measuring dose to organs that had a high degree of sensitivity to radiation and were located within or very close to the primary radiation field. However, as evidenced by the high stomach doses measured for the cardiac CTA protocol on the 64-slice scanner, a significant amount of radiation may be added to organs adjacent to the scan volume for helical protocols due to scan overranging. Where this is a consequence of the helical rotations of the x-ray tube around the phantom resulting in additional dose of two half-rotations, there is a possibility to measure even larger reductions in dose to these organs outside the

boundaries of the scan by using the wide-beam volumetric scanner that does not require these two extra half-rotations for interpolation.

11.3 Final Words

While the medical information acquired from CT scanning is a benefit that normally outweighs the risk associated with radiation, it is important to follow the ALARA (as low as reasonably achievable) principle and keep patient doses as small as possible. The 320-slice volumetric scanner is a perfect example of the rapid increase in CT technology. Though not addressed in this research project, the competing technologies of dual-source and dual-energy CT scanners are also available and should be included in the discussion. With the concerted effort of the RPC at Shands at UF and the ongoing research of its medical physicists, the safety of patients is a priority and one that has been achieved through this research project.

APPENDIX A EXAMPLES OF IMPLEMENTED CT PROTOCOLS

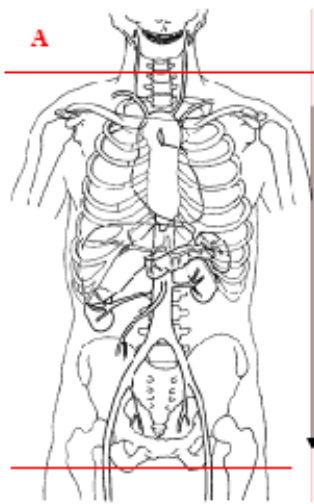
CT protocols were completed for radiology sub-specialty areas including body, cardiac, neurological, musculoskeletal (MSK)/orthopedic, and ear, nose and throat (ENT). The complete list of protocols can be found on the UF College of Medicine website.¹⁰

An example of a body protocol is the Chest/Abdomen/Pelvis protocol displayed in Figure A-1. As with most of the body protocols, it requires the use of a contrast agent and thus, the contrast or phase delay is noted in the acquisition table. A phase delay is sometimes necessary to wait for the contrast agent to travel through the vascular system and reach the area of interest of the study at the time of the scan acquisition. A cardiac protocol is illustrated in Figure A-2. The cardiac protocols use a diagram that is centered on the heart and have very detailed instructions in the “Other” section regarding when to begin injection of the contrast agent, as well as the indicated use of manufacturer-specific software-based reconstructions which differ by manufacturer, making it necessary to include reconstruction and reformation instructions for both manufacturer-independent and manufacturer-specific protocols. An ENT protocol is shown in Figure A-3. The Reconstruction section displays an example of the illustrations and FOVs drawn on the protocol to improve visualization of the areas of clinical interest. Another diagram is used to depict the regions for the coronal reformation image set. Because the area of interest is solely the temporal bones, the coronal reformatted images do not need to go through the entire head; this specification of the reformatted image set is a clear example of implementing limits on the number of reformatted images for storage considerations in the PACS archive. A neuroradiology protocol is depicted in Figure A-4. The need for very thin image slices is typical in neuroradiology studies and indicated in the B1 reconstruction thickness of 0.5–0.75mm. A range of values for this parameter is given, rather than a single value because of potential

differences among slice thickness capabilities of CT scanners. Also of interest are the two separate image sets, one pre-contrast and the other post-contrast, generated for comparison. All three image planes are utilized, depicted in the lines in the illustrations as well as specified in the tables. Finally, an MSK protocol is shown in Figure A-5. In the case of MSK, there are many instances when the same protocol is applied to the body area of interest. The committee chose to keep the protocols as generic as possible in this case. Therefore, no illustration is used in the Acquisition section for many of these protocols, and the start and end points of the image acquisition are also not specified. Both the Reconstruction and Reformation tables also indicate the FOV according to the anatomy of interest. By not specifying anatomy, the protocol is flexible in order to avoid generating a large number of joint-specific protocols with the same acquisition and reconstruction parameters.

Chest / Abdomen / Pelvis

ACQUISITION



Patient Position	Supine	
Contrast	Oral: dilute, 4 cups IV: up to 100 ml	
Injection Rate	2 ml/sec	
Respiration	Breath hold	
Volume	Appropriate to achieve images as specified in following reconstruction tables.	
Acquisition Specs		
A general venous	Begin	Thoracic inlet
50-60 sec delay	End	Pubic symphysis

RECONSTRUCTION

A1	Algorithm	Soft tissue	A2	Algorithm	Lung
	Thickness	5 mm		Thickness	3 mm
	Spacing	5 mm		Spacing	3 mm
	FOV	Patient largest + 4 cm		FOV	Patient largest + 4 cm

REFORMATION

OTHER

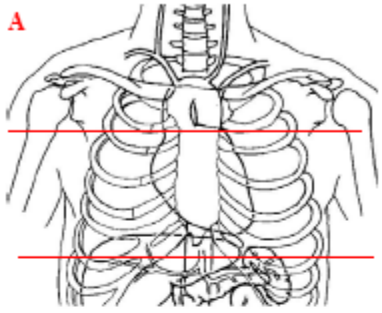
INDICATIONS

- Workup of metastatic disease
- Search for 1° malignancy
- Lymphoma
- Fever of unknown etiology

Figure A-1. Example of a body protocol. A phase delay of 50-60 seconds is utilized so that the administered contrast has time to travel through the blood stream to areas of the pelvis.

Cardiac CTA – Routine / Small - Average

ACQUISITION



Patient Position	Supine
Contrast	IV: 80 ml saline 80 ml Visipaque 320
Injection Rate	5 ml/sec
Respiration	Breath hold
Volume Acquisition Specs	Appropriate to achieve images as specified in following reconstruction tables. Pick small - average on setup for correct filters
A non-contrast	Begin 2 cm above carina End 2 cm below bottom of heart
B contrast*	Begin 2 cm above carina End 2 cm below bottom of heart

(Target heart rate – 55 – 65 bpm – no arrhythmias)

RECONSTRUCTION

TOSHIBA PROTOCOLS

A1 Algorithm	
Thickness	3 mm
Spacing	3 mm
FOV	220 mm
Prospectively Gated	75%

A2 Algorithm	
Thickness	3 mm
Spacing	3 mm
FOV	320 mm
Prospectively Gated	75%

B1 Algorithm	
Thickness	0.5 mm
Spacing	0.3 mm
FOV	220 mm
Gated	Best Phase

B2 Algorithm	
Thickness	0.5 mm
Spacing	0.3 mm
FOV	220 mm
Gated	ImageXact - RCA

B3 Algorithm	
Thickness	0.5 mm
Spacing	0.3 mm
FOV	220 mm
Gated	ImageXact - LAD

B4 Algorithm	
Thickness	2 mm
Spacing	2 mm
FOV	220 mm
Gated	ImageXact - Cx

B5 Algorithm	
Thickness	2 mm
Spacing	2 mm
FOV	220 mm
Gated	0-90% 10% intervals

B6 Algorithm	
Thickness	5 mm
Spacing	5 mm
FOV	320 mm
Gated	55%

Revised 1/9/2008

Page 1 of 2

Figure A-2. Example of a cardiac protocol. These images are generated in different ways on different CT scanners and thus two sets of reconstruction tables are used in this protocol.

VENDOR INDEPENDENT **

B1	Algorithm
Thickness	0.5 mm
Spacing	0.3 mm
FOV	220 mm
Gated	75%

B2	Algorithm
Thickness	0.5 mm
Spacing	0.3 mm
FOV	220 mm
Gated	40%

B3	Algorithm
Thickness	0.5 mm
Spacing	0.3 mm
FOV	220 mm
Gated	70%

B4	Algorithm
Thickness	0.5 mm
Spacing	0.3 mm
FOV	220 mm
Gated	80%

B5	Algorithm
Thickness	5 mm
Spacing	5 mm
FOV	320 mm
Gated	55%

B6	Algorithm
Thickness	2 mm
Spacing	2 mm
FOV	220 mm
Gated	0-90% 10% intervals

REFORMATION

OTHER

* S&V SureStart: Monitor descending aorta level of aortic valve

180 HU HR > 65 bpm

200 HU HR 55-65 bpm

** Reccnstruction should be done using vendor's phase choice software where available.

INDICATIONS

Chest pain in low to intermediate risk patient

Chest pain in low to intermediate risk patient with borderline or mildly abnormal ETT

Patient with possible coronary anomaly

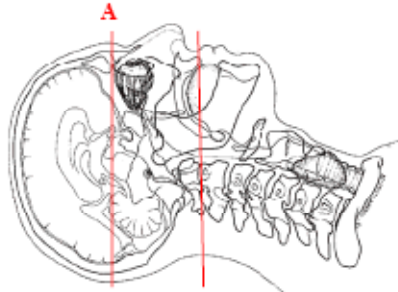
Patient with need for definition of bypass graft anatomy

Patient with need for definition of anatomy prior to EP ablation

Figure A-2. Continued

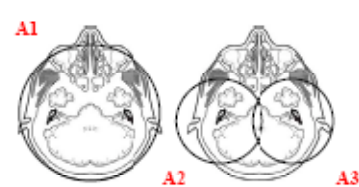
Temporal Bone Detail without Contrast

ACQUISITION



Patient Position	Supine IOML perpendicular to table top
Contrast	N/A
Injection Rate	N/A
Respiration	Quiet, NO swallowing
Volume	Appropriate to achieve images as specified in following reconstruction tables.
Acquisition Specs	Head FOV.
A Begin	Above sella
End	Through hard palate

RECONSTRUCTION

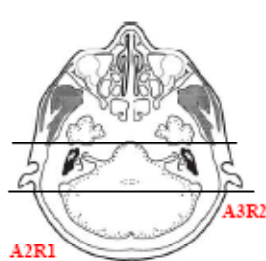


A1 Algorithm	Soft
Thickness	1.0 mm
Spacing	0.8 mm
F.O.V.	Approx 180

A2 Algorithm	Bone
Thickness	0.5- 0.75 mm
Spacing	0.3 -0.5 mm
F.O.V.	Approx. 30-90

A3 Algorithm	Bone
Thickness	0.5- 0.75 mm
Spacing	0.3 -0.5 mm
F.O.V.	Approx. 80-90

REFORMATION



A2R1 Algorithm	Bone
Thickness	1.0 mm
Spacing	1.0 mm
F.O.V.	80-90 each temporal bone
Plane	Coronal
Begin	TMJ
End	Through IAC

A3R2 Algorithm	Bone
Thickness	1.0 mm
Spacing	1.0 mm
F.O.V.	80-90 each temporal bone
Plane	Coronal
Begin	TMJ
End	Through IAC

OTHER

Indications

- Chronic otomastoiditis
- Cholesteatoma
- Congenital abnormalities external, middle and inner ear
- Cochlear implants
- CSF otorrhea
- Other uncomplicated inflammatory disease
- Sensorineural hearing loss-inner ear anatomy only (not VIIIth nerve)
- Trauma
- Pulse synchronous tinnitus WITH a visible middle ear mass**

Revised 7/23/2007

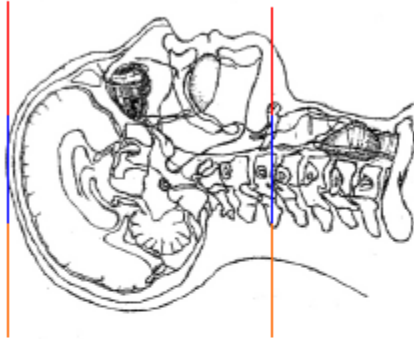
Page 1 of 1

Figure A-3. An example of an ENT protocol. Two small circles in the locations of the right and left temporal bone denote specific areas for the reconstructed coronal images. Horizontal lines show the plane and specific area of reformatted coronal images.

CTA Head

ACQUISITION

A, B, C



	Patient Position	Supine. IOML perpendicular to table top
	Contrast	100 ml adult
	Injection Rate	4 ml/sec, visual trigger at hyoid
	Respiration	Breath Hold
	Volume	Appropriate to achieve images as specified in following reconstruction tables.
	Acquisition Specs:	Head FOV.
A	Begin	C3
Noncontrast head	End	Skull Vertex
B	Begin	C3
CTA head	End	Skull Vertex
C	Begin	C3
Delayed postcontrast head	End	Skull Vertex

RECONSTRUCTION



A1	Algorithm	Brain
	Thickness	5.0 mm
	Spacing	5.0 mm
	F.O.V.	Approx 220

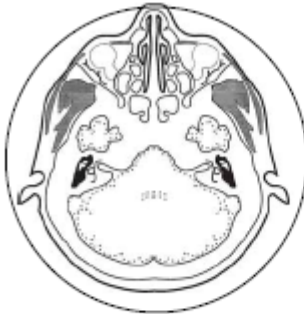
B1	Algorithm	Soft Tissue
	Thickness	0.5-0.75 mm
	Spacing	0.3-0.5 mm
	F.O.V.	Approx 220

C1	Algorithm	Brain
	Thickness	5.0 mm
	Spacing	5.0 mm
	F.O.V.	Approx 220

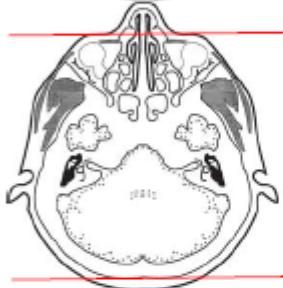
Figure A-4. Example of a neuroradiology protocol, depicting the Acquisition, Reconstruction, Reformation and Indications sections.

CTA Head

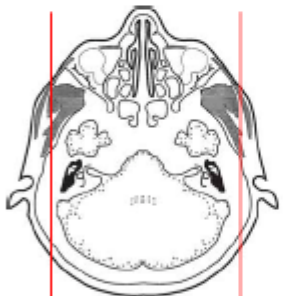
REFORMATION



B1R1	Algorithm	Soft Tissue
	Thickness	10 mm
	Spacing	5 mm
	F.O.V.	Approx 220
	Plane	Axial MIP



B1R2	Algorithm	Soft Tissue
	Thickness	10 mm
	Spacing	5 mm
	F.O.V.	To be specified by tech
	Plane	Coronal MIP



B1R3	Algorithm	Soft Tissue
	Thickness	10 mm
	Spacing	5 mm
	F.O.V.	To be specified by tech
	Plane	Sagittal MIP

INDICATIONS

Subarachnoid Hemorrhage

Vascular Abnormality: Aneurysm, AVM, Stenosis, etc.

Vascular bypass surgery

Revised 12/6/2007

Page 2 of 2

Figure A-4. Continued

Trauma – Joint Involved

ACQUISITION

Patient Position	Supine
Contrast	None
Injection Rate	N/A
Respiration	N/A
A* Begin	Above fracture / joint
End	Below fracture / joint

RECONSTRUCTION

A1 Algorithm	Bone	A2 Algorithm	Soft tissue
Thickness	0.75 mm	Thickness	2 mm
Spacing	0.5 mm	Spacing	2 mm
FOV	Appropriate to body part	FOV	Appropriate to body part
Plane	Axial	Plane	Axial

REFORMATION

AIR1* Algorithm	Bone	AIR2* Algorithm	Bone
Thickness	2 mm	Thickness	2 mm
Spacing	1 mm	Spacing	1 mm
FOV	Appropriate to body part	FOV	Appropriate to body part
Plane	True coronal to body part	Plane	True sagittal to body part

SPECIAL INSTRUCTIONS

*Usually the fracture is on one side of joint, extending into the joint.

If this is the case, include ALL of the fracture and joint about 2 cm past the other side of the joint.

If there is a fracture on BOTH sides of the joint, then include all of each fracture.

Figure A-5. Example of an MSK protocol.

APPENDIX B DOSIMETRIC PHANTOMS

Phantom Construction

While the construction methodology and details of the specific phantoms used in this research project are yet to be published, the methodology was the same as that published by Jones in 2003.³⁹ First, image segmentation was used to define the contours of the organs within the data sets; second, tissue-equivalent materials were developed and third, automated methods were used in the physical construction of the phantoms.

Image Segmentation

For the purpose of accurate and reproducible segmentation, and to expedite the process, an automatic segmentation method was utilized by the group at UF.³⁶ The goal of this process was to define the contours of each organ displayed within a CT slice. Various CT number thresholding methods were utilized for this purpose. Once a contour has been defined, all voxels within that contour are assigned a tag value. Each organ has a unique tag value, thereby differentiating between as many organs as are segmented.

Tissue-Equivalent Materials

Three tissue-equivalent compositions were developed for the purpose of constructing these tomographic phantoms: bone (or skeletal) tissue, soft tissue and lung tissue. The three tissue-equivalent materials were matched to three basic physics characteristics: density, mass attenuation coefficient, and mass energy absorption coefficient. An epoxy resin-based system was used to manufacture the main matrix of the tissue equivalent materials using phenolic microspheres as needed to adjust the mass density. The reference values used for these tissues of interest were those published by Cristi and Eckerman, in association with the Oak Ridge National Laboratory (ORNL).⁶⁸

In his paper, Jones argued that there was no need for developing a larger, more specific set of tissue equivalent materials because of the inherent error associated with the dosimetry system he used for organ dose measurements. Thus, in addition to the fact that phantom construction is outside the scope of this project, the dosimetry system used for this research project is different, but sources of error exist in it that are greater than the small differences in tissue composition of all of the segmented organs making use of these phantoms adequate for this research project.

Phantom Specifications

Adult Male Phantom

Two of the UF tomographic phantoms were used in this research project: an adult male and a pediatric male. The adult male was built using data from work by Lee *et al.*⁶⁹ The computational model known as KTMAN-2 was based on whole-body CT images of a 35-year old Korean male whose height and weight closely matched those of the average Korean man. The CT image set was acquired with a pixel resolution of 2x2x5 mm³. The CT scan was performed with contrast to provide images with high soft-tissue resolution, and the images were reconstructed at 1-mm thick slices.

Work was further done at UF by Ambrose⁷⁰ to transform the data from KTMAN-2 into a corresponding American counterpart; organ masses were scaled to those of the American reference male (approximately 176 cm tall and a weight of 72.9 kg). Known as “gatorman,” the data from this tomographic phantom were the basis for the physical phantom used in this research project. The phantom is composed of the same three tissue-equivalent materials as discussed and developed by Jones, and is pictured in Figure 6-1.

Pediatric Phantom

The pediatric phantom was constructed based on a 9-month old computational phantom built as part of the UF series.³⁷ Data used for the phantom were obtained from CT scans of a 9-

month old male patient: one of the chest, abdomen, pelvis and a second of the head. The image segmentation process previously described was followed to assign one of three tissue-equivalent materials to each segmented organ. While the construction process of this 9-month phantom is yet to be published,⁶⁵ the methodology is similar to that described by Jones and Simon.⁷¹ This phantom is depicted in Figure 6-2.

While stylized models have been used with success in the past, the UF series of tomographic, physical phantoms is far superior to its predecessors for the purpose of organ dose measurements. The use of CT data sets for image segmentation gives these phantoms the most realistic and detailed organ structure, as well as accurate organ position within the phantom. Tissue-equivalent materials representing different human tissue further substantiate the usefulness of the UF phantoms for organ dose estimates.

LIST OF REFERENCES

- ¹F. A. Mettler, P. W. Wiest, Jr., J. A. Locken, and C. A. Kelsey, "CT scanning: patterns of use and dose," *J. Radiol. Prot.* **20**, 353-359 (2000).
- ²D. Brenner, C. Elliston, E. Hall, and W. Berdon, "Estimated risks of radiation-induced fatal cancer from pediatric CT," *Am. J. Roentgenol.* **176**, 289-296 (2001).
- ³National Council on Radiation Protection and Measurements, "Ionizing Radiation Exposure of the Population of the United States," Report 160 (2009).
- ⁴Conference of Radiation Control Program Director, Inc., "Nationwide evaluation of x-ray trends (NEXT) 2000-2001 survey of patient radiation exposure from computed tomography examinations in the United States," Report E-07-2 (2007).
- ⁵D. Brenner, "Estimating cancer risks from pediatric CT: going from the qualitative to the quantitative," *Pediatr. Radiol.* **32**, 228-330 (2002).
- ⁶J. T. Bushberg, J. A. Seibert, E. M. Leidholdt, Jr., and J. M. Boone, *The Essential Physics of Medical Imaging*, 2nd ed. (Lippencott Williams & Wilkins, Philadelphia, 2002).
- ⁷C. P. Langlotz, "RadLex: A new method for indexing online educational materials," *Radiographics.* **26**, 1595-1597 (2002).
- ⁸American College of Radiology, *Index for Radiological Diagnoses*, 4th ed. (American College of Radiology, Reston, 1992).
- ⁹T. M. Buzug, *Computed Tomography: From Photon Statistics to Modern Cone-Beam CT*, 1st ed. (Springer, Verlag, 2009).
- ¹⁰Protocols [Internet]. Gainesville: University of Florida, College of Medicine (US); [updated 2009 Jun 24; cited 2009 Jun 24]. Available from: <http://xray.ufl.edu/patient-care/protocols>.
- ¹¹C. H. McCollough *et al.*, AAPM Task Group 23: CT Dosimetry, American Association of Physicists in Medicine. Task Group Report 96, 2008..
- ¹²Aquilion ONE: The Quantum Advantage [Internet]. Tustin: Toshiba America Medical Systems (US); [cited 2009 Jun 23]. Available from: www.medical.toshiba.com.
- ¹³E. Siebert, G. Bohner, M. Dewey, F. Masuhr, K. T. Hoffmann, J. Mews, F. Engelken, H. C. Bauknecht, S. Diekmann, and R. Klingebiel, "320-slice CT neuroimaging: initial clinical experience and image quality evaluation," *Br. J. Radiol.* **82**, 561-570 (2009).

- ¹⁴Neuro and Acute Stroke Imaging with Dynamic Volume CT [Internet]. Tustin: Toshiba America Medical Systems (US); [cited 2009 Jun 23]. Available from: http://www.healthcaretechguide.com/index.php?option=com_resource&controller=whitepaper&task=inquire&id=207&Itemid=2.
- ¹⁵P. Rogalla, B. Stover, I. Scheer, R. Juran, G. Gaedicke, and B. Hamm, "Low-dose spiral CT: applicability to paediatric chest imaging," *Pediatr. Radiol.*, **29**, 565-569 (1999).
- ¹⁶M. K. Kalra, M. M. Maher, T. L. Toth, B. Schmidt, B. L. Westerman, H. T. Morgan, and S. Saini, "Techniques and applications of automatic tube current modulation for CT," *Radiology*, **233**, 649-657 (2004).
- ¹⁷P. Vock, "CT dose reduction in children," *Eur. Radiol.* **15**, 2330-2340 (2005).
- ¹⁸D. D. Cody, D. M. Moxley, K. T. Krugh, J. C. O'Daniel, L. K. Wagner, and F. Eftekhari, "Strategies for formulating appropriate MDCT techniques when imaging the chest, abdomen, and pelvis in pediatric patients," *Am. J. Roentgenol.* **182**, 849-859 (2004).
- ¹⁹National Council on Radiation Protection and Measurements, "Limits of Exposure to Ionizing Radiation," Report 116, (1993).
- ²⁰International Commission on Radiological Protection, "The 2007 Recommendations of the International Commission on Radiological Protection," Report 103 (2007).
- ²¹International Commission on Radiological Protection, "Conversion coefficients for use in radiological protection against external radiation. Adopted by the ICRP and ICRU in September 1995," *Annals of the ICRP*, **26**, 1-205 (1996).
- ²²C. H. McCollough and B. A. Schueler, "Calculation of effective dose," *Med. Phys.* **27**, 828-837 (2008).
- ²³G. Drexler, W. Panzer, N. Petoussi, and M. Zankl, "Effective dose - how effective for patients?," *Radiat. Environ. Biophys.* **32**, 209-219 (1993).
- ²⁴T. B. Shope, R. M. Gagne, and G. C. Johnson, "A method for describing the doses delivered by transmission x-ray computed tomography," *Med. Phys.* **8**, 488-495 (1981).
- ²⁵Food and Drug Administration, "FDA public health notification: reducing radiation risk from computed tomography for pediatric and small adult patients," *Pediatr. Radiol.* **32**, 314-316 (2002).
- ²⁶W. Leitz, B. Axelsson, and G. Szendro, "Computed tomography dose assessment: a practical approach," *Radiat. Prot. Dosim.* **57**, 377-380 (1995).
- ²⁷A. Suzuki and M. N. Suzuki, "Use of a pencil-shaped ionization chamber for measurement of exposure resulting from a computed tomography scan," *Med. Phys.* **5**, 536-539 (1978).

- ²⁸R. L. Dixon, "A new look at CT dose measurement: beyond CTDI," *Med. Phys.* **30**, 1272-1280 (2003).
- ²⁹J. M. Boone, "The trouble with CTD100," *Med. Phys.* **34**, 1364-1371 (2007).
- ³⁰S. Mori, M. Endo, K. Nishizawa, T. Tsunoo, T. Aoyama, H. Fujiwara, and K. Murase, "Enlarged longitudinal dose profiles in cone-beam CT and the need for modified dosimetry," *Med. Phys.* **32**, 1061-1069 (2005).
- ³¹R. L. Dixon and A. C. Ballard, "Experimental validation of a versatile system of CT dosimetry using a conventional ion chamber: beyond CTDI100," *Med. Phys.* **34**, 3399-3413 (2007).
- ³²G.F.Knoll, *Radiation Detection and Measurement*, 3rd ed. (John Wiley & Son, Hoboken, 2000).
- ³³Radcal Corporation, "Model 9010 Radiation Monitor Controller Manual," (2009).
- ³⁴National Institute of Standards and Technology, "Ionizing radiation measurements: dosimetry of x ray, gamma rays, and electrons," (2009). Available from: <http://ts.nist.gov/MeasurementServices/Calibrations/x-gamma-ray.cfm>.
- ³⁵RTI Electronics, Inc., "Selection guide," (2009). Available at: <http://www.rti.se/cuda/index.htm>.
- ³⁶J. C. Nipper, J. L. Williams, and W. E. Bolch, "Creation of two tomographic voxel models of paediatric patients in the first year of life," *Phys. Med. Biol.* **47**, 3143-3164 (2002).
- ³⁷C. Lee, J. L. Williams, C. Lee, and W. E. Bolch, "The UF series of tomographic computational phantoms of pediatric patients," *Med. Phys.* **32**, 3537-3548 (2005).
- ³⁸C. Lee, C. Lee, R.J. Staton, D.E. Hintenlang, M.M. Arreola, J.L. Williams, and W.E. Bolch, "Organ and effective doses in pediatric patients undergoing helical multislice computed tomography examination," **34**, 1858-1873 (2007).
- ³⁹A. K. Jones, T. A. Simon, W. E. Bolch, M. M. Holman, and D. E. Hintenlang, "Tomographic physical phantom of the newborn child with read-time dosimetry I. Methods and techniques for construction," *Med. Phys.* **33**, 3274-3282 (2006).
- ⁴⁰L.N. Rill, L. Brateman, and M. Arreola, "Evaluating radiographic parameters for mobile chest computed radiography: phantoms, image quality and effective dose," *Med. Phys.* **30**, 2727-2735 (2003).
- ⁴¹S.R. Prasad, C. Wittram, J.A. Shepard, T. McCloud, and J. Rhea, "Standard-dose and 50%-reduced-dose chest CT: comparing the effect on image quality," *Am.J.Roentgenol.* **179**, 461-465 (2002).
- ⁴²C.H. McCollough and F.E. Zink, "Performance evaluation of a multi-slice CT system," *Med. Phys.* **26**, 2223-2230 (1999).

- ⁴³Catphan 500 & 600 brochure [Internet]. Salem: The Phantom Laboratory (US); [cited Jun 24 2009]. Available from: <http://www.phantomlab.com/catphan.html>.
- ⁴⁴M. S. Akselrod, L. Botter-Jensen, and S. W. S. McKeever, "Optically stimulated luminescence and its use in medical dosimetry," *Radiat. Meas.* **41**, S78-S99 (2007).
- ⁴⁵P. A. Jursinic, "Characterization of optically stimulated luminescent dosimeters, OSLDs, for clinical dosimetric measurements," *Med. Phys.* **34**, 4594-4604 (2007).
- ⁴⁶E. G. Yukihiro, E. M. Yoshimura, T. D. Lindstrom, S. Ahmad, K. K. Taylor, and G. Mardirossian, "High-precision dosimetry for radiotherapy using the optically stimulated luminescence technique and thin Al₂O₃:C dosimeters," *Phys. Med. Biol.* **50**, 5619-5628 (2005).
- ⁴⁷S. W. S. McKeever, M. S. Akselrod, L. E. Colyott, N. A. Larsen, J. C. Polf, and V. Whitley, "Characterisation of Al₂O₃ for use in thermally and optically stimulated luminescence dosimetry," *Radiat. Prot. Dosim.* **84**, 163-168 (1999).
- ⁴⁸A. Viamonte, L.A. da Rosa, L.A. Buckley, A. Cherpak, and J.E. Cygler, "Radiotherapy dosimetry using a commercial OSL system," *Med. Phys.* **35**, 1261-1266 (2008).
- ⁴⁹V. Schembri, and B.J. Heijmen, "Optically stimulated luminescence (OSL) of carbon-doped aluminum oxide (Al₂O₃:C) for film dosimetry in radiotherapy," *Med. Phys.* **34**, 2113-2118 (2007).
- ⁵⁰B. G. Markey, L. E. Colyott, and S. W. S. McKeever, "Time-resolved optically stimulated luminescence from alpha-Al₂O₃:C," *Radiat. Meas.* **24**, 457-463 (1994).
- ⁵¹American National Standards Institute, Inc., "American National Standard for Dosimetry - Personnel Dosimetry Performance - Criteria for Testing," Report N13.11-2009, (2009).
- ⁵²Landauer, Inc., "microStar User Manual," (2008).
- ⁵³International Electrotechnical Commission, "Medical diagnostic X-ray equipment - radiation conditions for use in the determination of characteristics," IEC Report 1267 (1994).
- ⁵⁴International Electrotechnical Commission, "Medical diagnostic X-ray equipment - radiation conditions for use in the determination of characteristics," IEC Report 61267 (2005).
- ⁵⁵R. I. Aviv, E. Rodger, and C. M. Hall, "Craniosynostosis," *Clin. Radiol.* **57**, 93-102 (2002).
- ⁵⁶N. Hirai, J. Horiguchi, C. Fujioka, M. Kiguchi, H. Yamamoto, N. Matsuura, T. Kitagawa, H. Teragawa, N. Kohno, and K. Ito, "Prospective versus retrospective ECG-gated 64-detector coronary CT angiography: assessment of image quality, stenosis, and radiation dose," *Radiology.* **248**, 424-430 (2008).

- ⁵⁷F. J. Rybicki, H. J. Otero, M. L. Steigner, F. Vorobiof, L. Nallamshetty, D. Mitsouras, H. Ersoy, R. T. Mather, P. F. Judy, T. Cai, K. Coyner, K. Schultz, A. G. Whitmore, and M. F. Di Carli, "Initial evaluation of coronary images from 320-detector row computed tomography," *Int. J. Cardiovasc. Imaging.* **24**, 535-546 (2008).
- ⁵⁸K. Kitagawa, A. C. Lardo, J. A. Lima, and R. T. George, "Prospective ECG-gated 320 row detector computed tomography: implications for CT angiography and perfusion imaging," *Int. J. Cardiovasc. Imaging.* Published online 2-18-2009, available from: <http://www.springerlink.com/content/n05324735g457720/>.
- ⁵⁹M. L. Steigner, H. J. Otero, T. Cai, D. Mitsouras, L. Nallamshetty, A. G. Whitmore, H. Ersoy, N. A. Levit, M. F. Di Carli, and F. J. Rybicki, "Narrowing the phase window width in prospectively ECG-gated single heart beat 320-detector row coronary CT angiography," *Int. J. Cardiovasc. Imaging.* **25**, 85-90 (2009).
- ⁶⁰L. M. Hurwitz, R. E. Reiman, T. T. Yoshizumi, P. C. Goodman, G. Toncheva, G. Nguyen, and C. Lowry, "Radiation dose from contemporary cardiothoracic multidetector CT protocols with an anthropomorphic female phantom: implications for cancer induction," *Radiology.* **245**, 742-750 (2007).
- ⁶¹M. Clemons, L. Loijens, and P. Goss, "Breast cancer risk following irradiation for Hodgkin's disease," *Cancer Treat. Rev.* **26**, 291-302 (2000).
- ⁶²J. Geleijns, A.M. Salvado, P.W. de Bruin, R. Mather, Y. Muramatsu, and M.F. Nitt-Gray, "Computed tomography dose assessment for a 160 mm wide, 320 detector row, cone beam CT scanner," *Phys. Med. Biol.* **54**, 3141-3159 (2009).
- ⁶³M.K. Kalra, M.M. Maher, T.L. Toth, L.M. Hamberg, M.A. Blake, J.A. Shepard, and S. Saini, "Strategies for CT radiation dose optimization," *Radiology.* **230**, 619-628 (2004).
- ⁶⁴S. Mori, K. Nishizawa, M. Ohno, and M. Endo, "Conversion factor to CT dosimetry to assess patient dose using a 256-slice CT scanner," *Brit. J. Radiol.* **79**, 888-892 (2006).
- ⁶⁵J.F. Winslow, D.E. Hyer, R.F. Fisher, C.J. Tien, and D.E. Hintenlang, "Construction of anthropomorphic phantoms for use in dosimetry studies," Accepted *J. Appl. Clin. Med. Phys.* (2009).
- ⁶⁶Centers for Disease Control and Prevention, "Cutaneous Radiation Injury: Fact Sheet for Physicians," (2005). Available from: <http://emergency.cdc.gov/radiation/pdf/crphysicianfactsheet.pdf>.
- ⁶⁷M. Ghita, PhD dissertation, University of Florida, 2009.
- ⁶⁸M. Cristy and K. F. Eckerman, *Specific Absorbed Fractions of Energy at Various Ages from Internal Photon Sources*, ORNL/TM-8381/Volumes I-VII. (Oak Ridge National Laboratory, Oak Ridge, 1987)³⁷C. Lee, C. Lee, S. Park, and J. Lee, "Development of the two Korean adult tomographic computational phantoms for organ dosimetry," *Med. Phys.* **33**, 380-390 (2006).

⁶⁹C. Lee, C. Lee, S. Park, and J. Lee, "Development of the two Korean adult tomographic computational phantoms for organ dosimetry," *Med. Phys.* **33**, 380-390 (2006).

⁷⁰R. Ambrose, MS thesis, University of Florida, 2006.

⁷¹A. K. Jones, T. A. Simon, W. E. Bolch, M. M. Holman, and D. E. Hintenlang, "Tomographic physical phantom of the newborn child with read-time dosimetry I. Methods and techniques for construction," *Med. Phys.* **33**, 3274-3282 (2006).

BIOGRAPHICAL SKETCH

Lindsey K Lavoie was born in Boston, Massachusetts on June 28th, 1982 to Charles and Dona Lavoie. She graduated from Bishop Stang High School in 2000. In 2004, she graduated with honors from the College of the Holy Cross, earning a Bachelor of Arts degree in physics. After being accepted into the medical physics program at the University of Florida, she was awarded her master's degree in 2007. In the summer of 2009, she graduated from the University of Florida with a Ph.D. in medical physics.